

Alma Mater Studiorum – Università di Bologna

**DOTTORATO DI RICERCA IN
GEOFISICA**

Ciclo XXV

Settore Concorsuale di afferenza: 04/A4

Settore Scientifico disciplinare: GEO/10

TITOLO TESI

**TOWARD A MAGNITUDE SCALE FOR LOW
FREQUENCY SEISMICITY
The LP energy for Campi Flegrei caldera**

Presentata da: IRENE BORGNA

Coordinatore Dottorato

Relatore

Prof. Michele Dragoni

Dr.ssa Francesca Bianco

Esame finale anno 2014

Contents

1. Abstract.....	5
2. Introduction	6
3. Volcanic seismicity – source dynamic and seismic signature	9
3.1 Long Period seismicity.....	13
4. Campi Flegrei Caldera	17
4.1 The bradyseism and seismic activity at Campi Flegrei	21
4.2 The seismic network at Campi Flegrei	28
5. The October 2006 seismic events at Campi Flegrei.....	30
6. Data analysis – first step	36
6.1 Preliminary analysis of the waveforms	36
6.2 Duration of the events	39
6.2.1 Duration – visually selection.....	39
6.2.2 Duration routines.....	43
6.3 Energy estimates – first step	46
6.3.1 Energy via theoretical formula	46
6.3.2 Energy via envelope.....	49
6.3.3 Conclusion of the first step of study.....	54
6.4 Waveforms analysis.....	55
6.4.1 The spectrograms	55
6.4.2 Cross-correlation of the waveforms	59
6.4.3 Noise analysis	63
7. The energy and magnitude estimation method	66
7.1 Signal theory.....	66
7.2 The duration	67
7.3 Spectral analysis – the energy evaluation	69
7.4 The Magnitude estimation method	71
7.4.1 The error estimation.....	78
8. Data analysis - application of the method	79
8.1 Campi Flegrei.....	79

8.1.1	The dominant frequency	79
8.1.2	The magnitude estimation.....	84
8.1.3	Searching for a scaling law.....	88
8.2	Mount Colima.....	91
8.3	Mount Etna.....	96
9.	Conclusions and future developments	98
10.	List of figures	100
11.	List of tables	105
12.	Bibliography	106

1. Abstract

The energy released during a seismic crisis in volcanic areas is strictly related to the physical processes in the volcanic structure and could be a very important parameter to study in activities dealing with eruption forecasting. In particular Long Period seismicity, that seems to be related to the oscillation of a fluid filled crack (Chouet , 1996, Chouet, 2003, McNutt, 2005), can precedes or accompanies an eruption; these seismic signals may be used to assess the eruptive state of a volcano or its eruptive potential.

The present doctoral thesis is focused on the study of the Long Period seismicity recorded in the Campi Flegrei volcano (Campania, Italy) during the October 2006 crisis.

Campi Flegrei Caldera is an active caldera (situated in a densely populated area in the North of Naples); the combination of an active magmatic system and a dense populated area make the Campi Flegrei a critical volcano.

The source dynamic of LP seismicity is thought to be very different from the other kind of seismicity (Tectonic or Volcano Tectonic): it's characterized by a time sustained source and a low content in frequency. This features implies that the duration–magnitude, that is commonly used for Volcano Tectonic events and sometimes for LPs as well, is unadapted for LP (and VLP) magnitude evaluation. The main goal of the research work performed in the framework of the doctoral studies was to develop a method for the determination of the magnitude, for the LP seismicity; we based this method on the comparison of the energy of VT event and LP event, linking the energy to the moment magnitude for the VT. So the magnitude of the LP event would be the moment magnitude of a VT event with the same energy of the LP.

We applied this method to the LP data-set recorded at Campi Flegrei caldera in 2006, to an LP data-set of Colima volcano recorded during an experiment performed in 2005 – 2006 and for an event recorded at Etna volcano.

Experimenting this method to lots of waveforms recorded at different volcanoes we tested its easy applicability and consequently its usefulness in the routinely and in the quasi-real time work of a volcanological observatory.

2. Introduction

Volcanoes are geologic manifestations of highly dynamic physical and chemical processes in the interior of the Earth.

Volcanic eruptions and their impact on human society are one of the most severe natural hazards.

Often, before an eruption, a series of phenomena indicative of an abnormal state of the volcano occurs; these phenomena are defined as precursors. They include the increasing frequency and/or intensity of the earthquakes located below the volcano apparatus, the presence of volcanic tremor, the uplift of the soil, the opening of fractures, the increasing fumarolic activity and the variation in its temperatures and composition, the compositional variations of the fluids involved...

Their presence, duration and time interval before the eruption depends on factors that currently remain largely unknown. So the study of their temporal evolution may be very helpful in a monitoring context. Precursory observation often coincided with the starting of an eruption in open-conduit volcanoes, but the situation is more complicated in the case of quiescent volcanoes like Campi Flegrei caldera.

Volcano seismology aims to understand the nature and dynamics of magmatic systems, and to determine the extent and evolution of source regions of magmatic energy which are important for the understanding of the volcanic behavior. The energy released during a seismic crisis is strictly related to the physical processes in the volcanic structure and could be very important in eruption forecasting.

The study of the Low Frequency seismicity is relative new and therefore the knowledge about both the physical mechanisms responsible for such signals, and their propagative features it is constantly updated.

In particular, Long Period seismicity seems to be correlated with the resonance of a fluid filled crack (magmatic or hydrothermal fluid) (Chouet, 1996; Chouet, 2003, McNutt, 2005), it can precede or accompany an eruption hence these seismic signals may so be used to assess the eruptive state of a volcano or its eruptive potential. For example, swarms of small and shallow LP events can be the only precursor of an important phreatic activity (Barberi, *et al.*, 1992).

The seismic monitoring of the active volcanoes, such as Campi Flegrei, is necessary to put in evidence possible precursors of an imminent eruption. Unfortunately, there is no clear relation between the energy of the precursory seismicity signals and the strength of the subsequent eruption.

The present doctoral thesis is focused on the study of the Long Period seismicity recorded in the volcano of Campi Flegrei (Campania, Italy) in the October 2006.

Campi Flegrei Caldera is an active caldera (situated in a densely populated area in the North of Naples), which last eruption occurred on 1538 affecting the Monte Nuovo eruptive center (Di Vito, et al., 1999). The combination of an active magmatic system and a dense populated area make the Campi Flegrei a critical volcano, and the comprehension of the volcanic state is important to protect the population.

The source dynamic of the Long Period seismicity is thought to be very different from the other kind of seismicity: LP and VLP (Very Long Period) events are characterized by the time persistency of the source, the peak of the spectrum at low frequency (less than 5 Hz for LPs and much less for VLPs) and the absence of high-frequency components in the spectrum of their seismic radiation. One of the practical consequences of the lack of high-frequency coda is that the duration–magnitude, that is commonly used for Volcano Tectonic events and sometimes for LPs as well, cannot be used for LP (and VLP) magnitude evaluation since it could lead to confusing results.

The magnitude concept comes from the relationship between the waveform amplitude of a seismic event and its energy (taking into account the path attenuation). The definition of magnitude was then firstly proposed by Richter, measuring the amplitude of an event recorded at a well-known instrument. So the seismogram can be transformed into an equivalent Wood Anderson record using the empirical curve that describes the attenuation of the maximum amplitude with the source-station distance, taking a zero magnitude reference event.

Differently from a VT event, an LP characterized by a long (source) duration and a low maximum amplitude can have the same energy as another LP event with a greater maximum amplitude and a shorter duration, so the maximum amplitude alone is not sufficient to determine the magnitude of a Long Period event.

In fact, the spectral content of the VT event, with a source-duration shorter than that of an LP event, is much broader than that of the LP event, it makes the coda of a VT reach in high frequency energy making it longer than that of the LP event.

Consequently we needed a different parameter to evaluate the energy and then the magnitude of LP events.

After its definition (Kanamori, 1977), the moment-magnitude scale came into common use for the physical definition of a tectonic earthquake strength, since, first of all, it does not saturate for large earthquakes and it is based on the physical properties of the source. It is based on the calculation of the seismic spectrum assuming a double-couple source model and a far-field

radiation and measuring the level of the flat portion of the source spectrum (log-log plot).

Even if the moment-tensor inversion would produce more accurate results (e.g. Aster, *et al.*, 2008 and Auger, *et al.*, 2006) its application in quasi-real time could be more complicated.

We consequently decided to base the developed algorithm for the evaluation of the LP magnitude, on the comparison with the energy of VT event and LP event, linking the energy to the moment magnitude for a VT.

To reach this scope we studied the LP seismicity recorded in the 2006 October at Campi Flegrei Caldera, we developed the new algorithm for the LP magnitude estimation and we applied that method to this seismicity and also to the LP seismicity recently recorded at Colima volcano (Mexico) and Etna volcano (Sicily, south of Italy).

3. Volcanic seismicity – source dynamic and seismic signature

To have a clear idea of the link between the fluids transport (and therefore the volcanic activity) and the seismicity, it can be useful to classify the volcanic seismicity according to the waveform features and consequently to the physics of the source processes. A magma intrusion or oscillation perturbs the volcano edifice and leads to different kinds of signals. The large variety of seismic signals observed in volcanoes is thus the representation of the structural heterogeneity of the volcanic edifices, and can be classified into two families linked to two different sources: one originates in the rock (*Volcano-Tectonic* events) and the other originates in the fluid, of magmatic or hydrothermal component (*Long-Period, Very Long Period, Tremor and Hybrids*).

The first kind of events is associated with the shear failure in the volcanic edifice where the magmatic processes provide the source of the strain energy that leads to rock failure. These earthquakes are called *Volcano-Tectonic* (VT), to discern them from the 'pure' tectonics events although they're practically indistinguishable. So it is possible to discern the P and S waves arrivals and the characteristic frequency can reach value much greater than 5 Hz (Figure 1). The only difference from the 'pure' tectonic seismicity is the frequent occurrence of swarms of VT events, which do not follow the usual main-after-shock distribution (Wassermann, 2011). They involve purely elastic processes in the brittle rock and are often located around the conduit and magma reservoir. The VT seismicity is often the first sign of a renewed activity. The rising magma acts as an additional stress source, that superimposed to a regional stress field, leads to tensile faulting when magma is breaking the rock, or to earthquakes on preexisting faults as a reaction to additional stress.

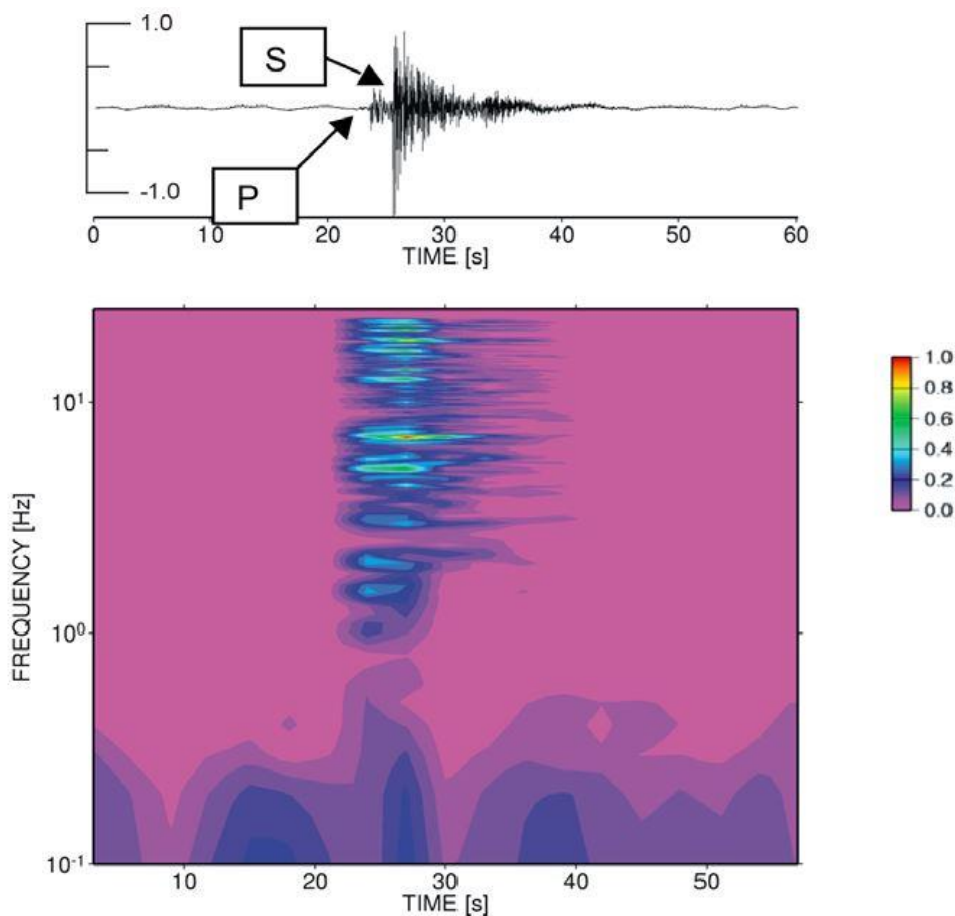


Figure 1 VT event recorded at Mt. Merapi (Indonesia). Arrivals of P and S waves clearly distinguishable. The colour coding represents normalized amplitude spectral (Wassermann, 2011).

The other kind of volcano seismicity, involving processes originating by the dynamic of the fluid, inside structures such as crack, pipes or fluid filled conduits, includes *Long Period* (LP) events, *Very Long Period* (VLP) and *Tremor*. The fluid component can have magmatic or geothermal origin and the gas content can vary greatly from volcano to volcano, accordingly with the depth of the source and the fugacity of the gas itself.

LP events differ from the tectonic earthquakes in their signature and spectral characteristic. There is no clear arrival for P and S waves and its characteristic frequency varies in fact from 0.5 Hz to 5 Hz (lower than the VT's) (Chouet , 1996) (Figure 2, Figure 3).

The VLP characteristic frequencies are lower than 0.5 Hz, while tremor have the same frequency band of LP but it differs from the latters about the duration: tremor is characterized by a signal of sustained amplitude lasting from minute to months or longer (Figure 4). This suggests that LP and tremor may have the same source process differing only in duration.

In the study of the dynamics of the whole volcanic structure, LP, VT and tremor are intimately tied together.

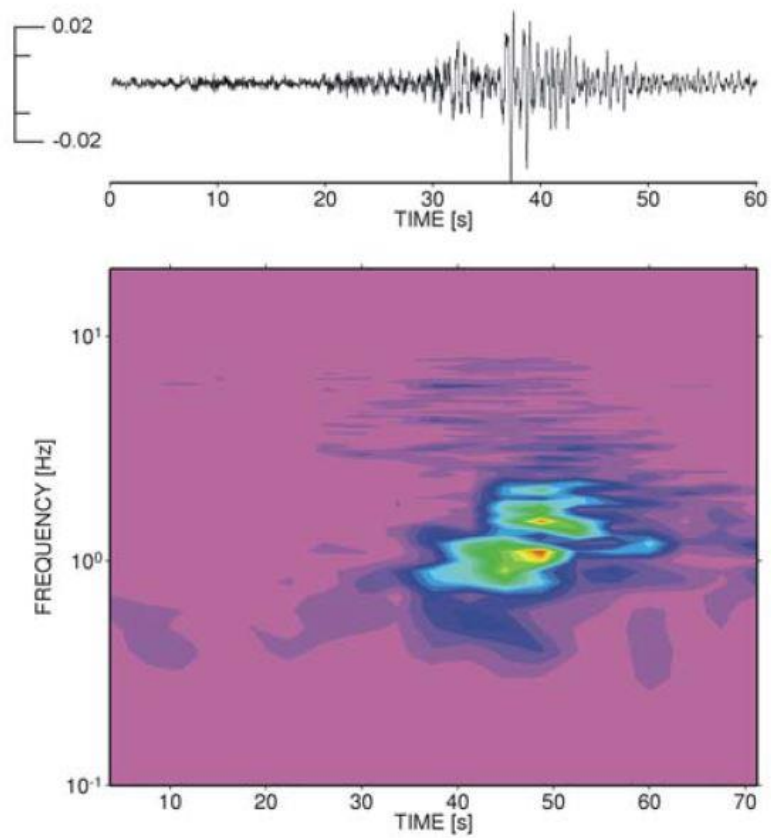


Figure 2 LP event recorded at Mt. Merapi. The dominant frequency is about 1 Hz (Wassermann, 2011).

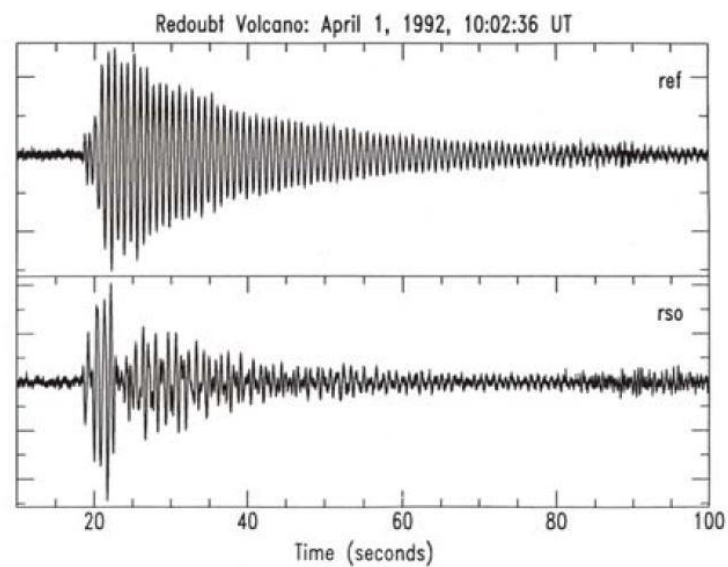


Figure 3 Example of LP event recorded at two different stations at Redoubt volcano (Alaska) (Wassermann, 2011). The spindle shape waveform is also known as 'tornillo'.

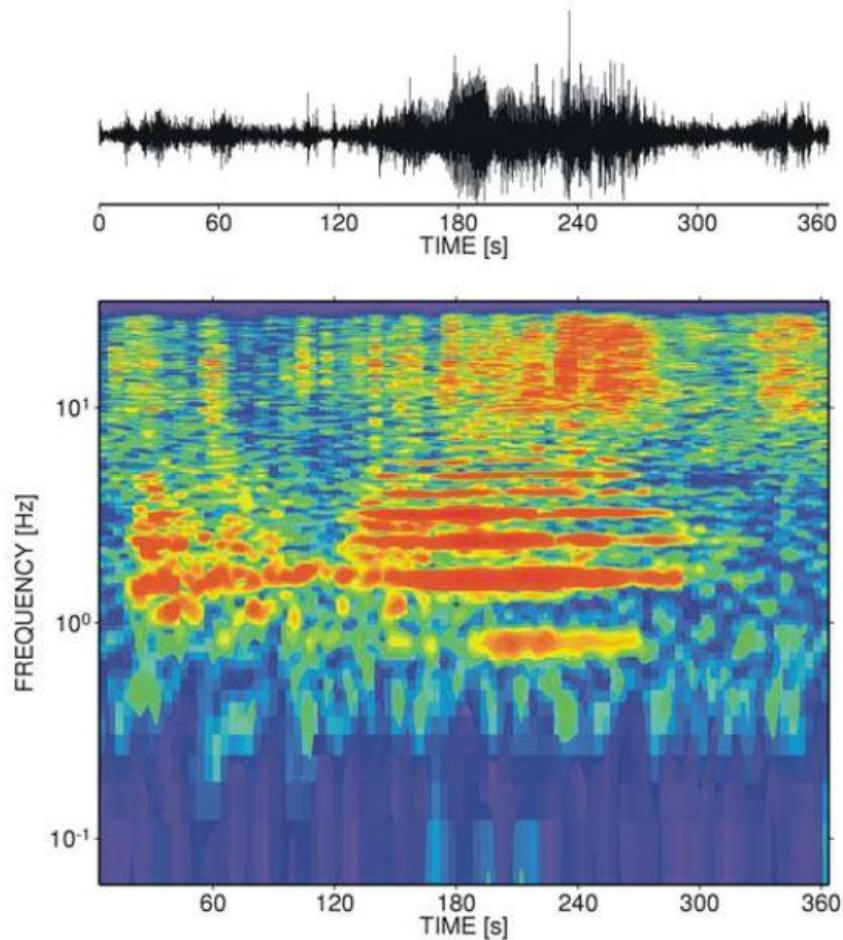


Figure 4 Tremor signal recorded at Mt. Semeru (Indonesia) (Wassermann, 2011).

Moreover, there is another kind of volcanic earthquakes, named *Hybrids*, that represents the transition between the two families described above, with signal and spectral characteristics of both intermediate between the LP and VT events. The hybrid events have an onset more pronounced than that of the LP, but an harmonic coda similar to the former . They are thought to involve shear faulting on a plane intersecting a fluid-filled crack, so they have both volumetric and shear component, and they can additionally reflect possible path effects (Wassermann, 2011).

This events are also related to a very shallow activity that may be associated with a growing dome (Miller, *et al.*, 1998).

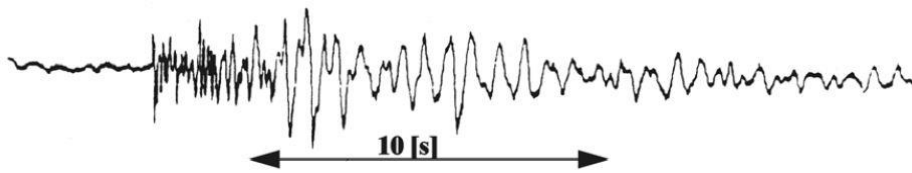


Figure 5 Hybrid event Redoubt volcano (Alaska) (Wassermann, 2011).

3.1 Long Period seismicity

In volumetric sources, gas, liquid and solid are dynamically coupled. The elastic radiation is the result of processes originating in the physics of the multi-phase fluid flow through cracks and conduits and the Long Period events are manifestations of such processes. The fluid (liquid or gas) may be of magmatic or geothermal origin and the gas content can vary depending on the volcano properties.

LP seismicity often occurs in the form of swarms and the similarity in the signature of individual events in some swarms strongly suggests the repetitive excitation of a stationary source in a non-destructive process.

Long Period events show no S-wave arrival but a very emergent signal onset (see, for instance, Figure 2) and, in the still rare cases in which the location of source are determined, they are often situated in the shallow part of the volcano (< 2 Km) (McNutt, 2005).

The source of the low frequency events is believed to be due to the mechanism of resonance produced by the oscillation of a fluid (magma or hydrothermal fluid) within cracks due to a perturbation of short duration (Chouet, 2003).

The LP events may be suitable to describe the volcanic and hydrothermal processes, since the properties of the resonator system may be inferred from the complex frequencies of the decaying harmonic oscillations in the tail of the seismogram.

The damped oscillations in the LP coda are described by two parameters, f and Q ; f is the frequency of the dominant mode of oscillation, and the parameter Q represents the quality factor of the oscillatory system (other than the quality factor of the earth medium). The observed Q may be expressed as:

$$Q^{-1} = Q_r^{-1} + Q_i^{-1}$$

Eq. 1

where Q_r^{-1} represents the radiation losses at the fluid-rock interface (is a function of the impedance contrast at the fluid-rock interface and of the geometry of the resonating cavity) and Q_i^{-1} represents the intrinsic attenuation of the fluid vibration depending only on the fluid properties (Saccorotti, *et al.*, 2007).

Typical frequencies observed for LP events are in the range 0.5–5 Hz (Chouet, 1996), and typical observed Q range from values near 1 to values larger than 100. In the following figure (Figure 6) waveforms recorded at different volcanoes and characterized by different Q values are represented.

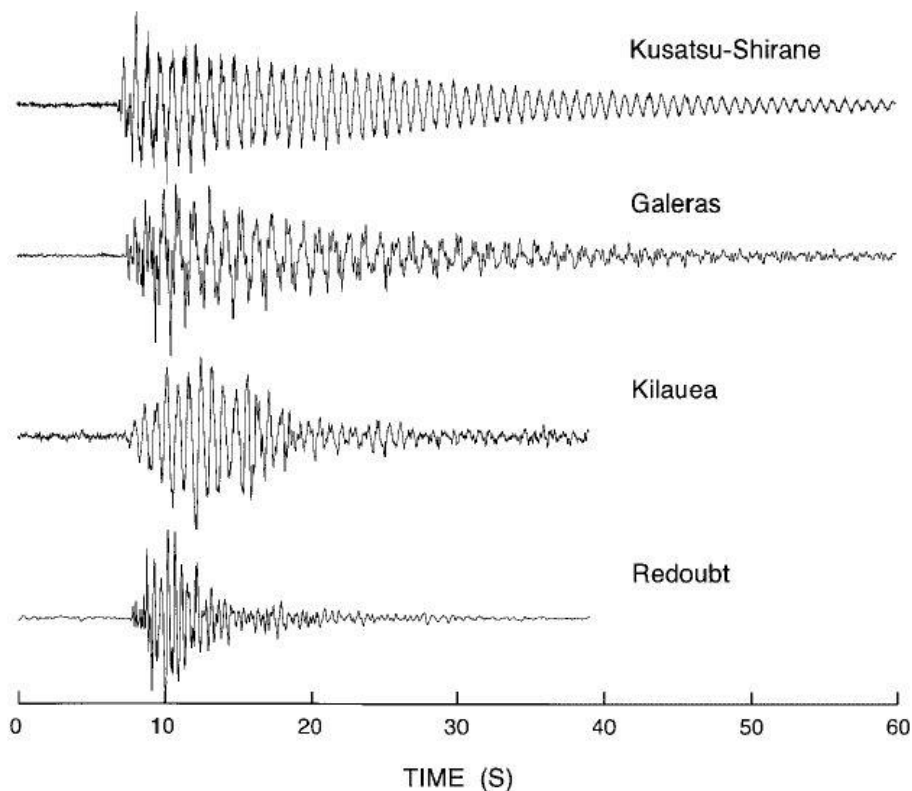


Figure 6 Waveforms of LP events recorded at different volcanoes: Kusatsu-Shirane, Galeras, Kilauea and Redoubt. The signatures are characterized by different Q values: the Q values of Kilauea and Redoubt events are between 20 and 50, the Q values of Kusatsu-Shirane and Galeras are higher than 100 (Chouet, 2003).

Once spectral peaks are identified in the wavefield of a LP event, to hypothesize and to test a model for the resonator source represents the next step.

Many geometries are possible resonators (pipes, spheres, cracks...) but the one that better explains the seismic data accordingly with mass transport conditions is the *crack model* (Chouet, 1996).

The fluid-filled crack model was originally proposed by Aki (Aki, *et al.*, 1977) and has been extensively studied by Chouet (Chouet, 2003 and references

therein) using a more formally detailed description of the coupling between fluid and solid.

This model consists in a rectangular crack with length L , width W and thickness d , filled with a fluid of density ρ_f , bulk modulus b and acoustic velocity a . The crack is in a solid half space with density ρ_s , rigidity μ and compressional velocity α .

The resonance is impressed by a pressure transient applied symmetrically in a small area in the center of the crack (see Figure 7).

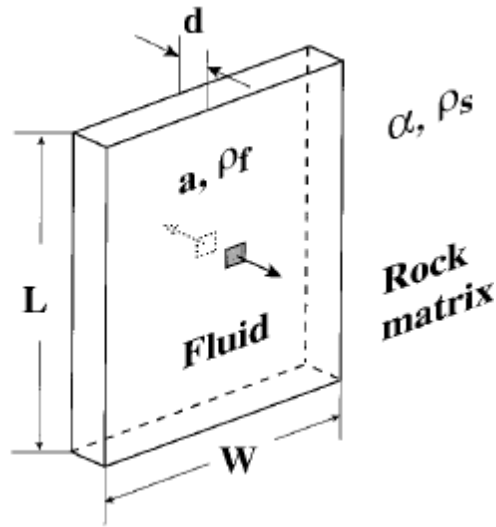


Figure 7 Geometry of the crack model (Chouet, 2003).

The crack resonance is controlled by two parameters: the crack stiffness C and the impedance contrast Z (Eq. 2):

$$C = \frac{b L}{\mu d} \quad Z = \frac{\rho_s \alpha}{\rho_f a}$$

Eq. 2

The stiffness controls the dispersion characteristics of the wave and the resonant frequencies generated by the source. The frequency is also controlled by the impedance contrast Z , that controls the duration of the signal too. The presence of gas bubbles can reduce the acoustic velocity and thus make possible the resonance at long period, and it can also increase the signal duration (increasing the Z). The long period signal can also be generated for an increasing of the C value (increase the phase velocity of the crack wave) if the crack is characterized by a large aspect ratio L/d or large contrast b/μ .

Once assumed a model for the crack-source, the properties of the resonator system can be determined from the complex frequency related to Q and f (Nakano & Kumagai, 2005) of decaying harmonic oscillations in the tail of the seismogram. The complex frequency is defined as $f - ig$ where $i = \sqrt{-1}$, f is the frequency and g the growth rate related to the quality factor of the resonator Q because $Q^{-1} = -2g/f$ which represents the fractional loss of elastic energy in each oscillation cycle at frequency f (Kumagai & Chouet, 1999).

A spectral method, named *Sompi*, was developed to quantify the spectral properties of the harmonic signals (Kumazawa, *et al.*, 1990).

So the properties of the fluid involved in the resonator may be deduced from the spectrum of the LP seismicity, but, to better constrain the possible results, a knowledge of geological and geochemical characteristics of the area are necessary (Chouet, 2003).

4. Campi Flegrei Caldera

The area of Campi Flegrei ('burning fields' from the greek) is located 15 km west north-west of the city of Naples, is almost circular area of size 12x15 Km, inhabited by 0.5 million people.

The Campi Flegrei is a caldera with, inside, numerous volcanic structures, formed during the various eruption, subsequent to those that caused the formation of the caldera.

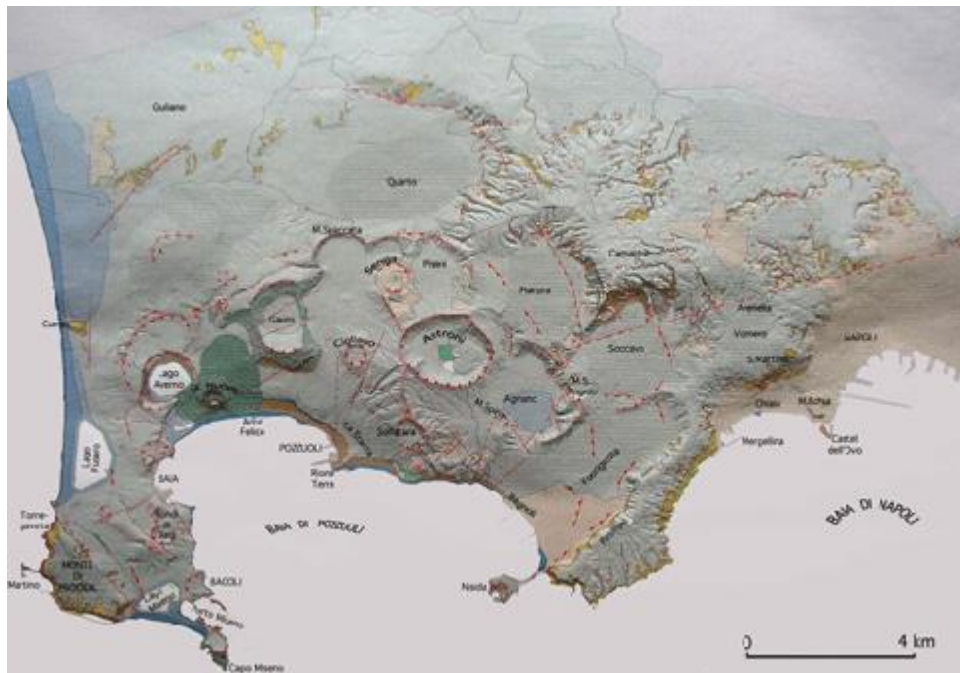


Figure 8 Campi Flegrei area, with the main volcano structures (Vulcani d'Italia - Uniroma3).

In Campania, the volcanic activity began around 150,000 years ago, in the Ischia island, and later in the Procida island, but in the Campi Flegrei area, the first manifestations, characterized by numerous and also violent eruptions, are probably occurred later, about 50-45000 years ago in the area of Cuma, although perforations made for the realization of geothermal wells, have shown the presence of other products arising from a previous activity. The eruption activity was concentrated in three phases separated by quiescence periods of 1000 and 3500 years (Di Vito, *et al.*, 1999).

The most important eruptions is undoubtedly the gigantic eruption of *Campanian Ignimbrite* (CI) (37-40,000 years ago) whose eruptive products, mainly ash and pumice, spanning an area that is covering the 'Piana Campana' up to the Apennines, with thicknesses that reach to 100 m (Scandone &

Giacomelli, 1998). They are almost absent in the central part of the Piana, either due to erosion, either because they are covered by the products of the next activity of Vesuvius and Campi Flegrei themselves and by alluvial soils.

The theories on the genesis of CI are numerous. According to some reconstructions (Rosi , *et al.*, 1983) (Rosi & Sbrana, 1987), this eruption occurred along a circular fracture which coincides with the edge of the current Campi Flegrei; the rapid emission of about 80-100 km³ of magma caused the collapse of the roof of the magma chamber and the formation of the caldera depression.

According to Lirer, *et al.*, (1987), however, the eruptive fracture included a larger area reaching the Bay of Naples, while Scandone *et al.* (1991) it had a NE-SW orientation and ran laterally to the Campi Flegrei. According to these authors, the origin of the Phlegrean caldera is to reconnect to a later stage than that of Ignimbrite Campana, the so-called Neapolitan Yellow Tuff eruption, whose products are widely distributed on the edge and inside the caldera (12000 years ago).

After this eruption the central part of the Campi Flegrei collapsed, forming the caldera (Lirer, *et al.*, 1987). Although smaller than the volume of Ignimbrite Campana (20 to 50 km³ of products, covering over 350 km²), after the NYT eruption, the morphological appearance of the area changed a lot, giving the Gulf of Naples, more or less its present appearance.

According to Scandone (Scandone R., *et al.*, 1991) after the eruption of the NYT, the lowest part of the Campi Flegrei has been submerged by the sea. The activity outside the caldera ends with this eruption, and the successive eruptions are confined within or along the edge of the caldera itself. The post-caldera activity is evidenced at the edge of the caldera itself by the cone of *Gauro Tuff*, with an age of about 10000 years. Around 8000 years ago, a large plinian eruption (*Pomici Principali*), occurs in the eastern area of Campi Flegrei. It is thought that this explosive eruption was followed by the eruption that built the island of Nisida and perhaps by another eruption on the crater rim where lately was formed the Solfatara.

Around 6000 years ago, after a period of stagnation in activity, evidenced by a paleosol, the central part of the Campi Flegrei begins to rise. In Pozzuoli, the movement of the soil is testified by a layer of marine sediments raised by about 40 m above the sea level.

Between 4500 and 3500 years ago, an intense eruptive activity returns in the Campi Flegrei (Astroni, 3700 years ago, and Monte Spina, 4000 years ago); the latest eruptions related to this phase of activity is the eruption of Senga and the Averno (Scandone & Giacomelli, 1998).

Subsequently, the soil of the Campi Flegrei, in its central part, begins to fall slowly in coincidence with a period of stagnation in the eruptive activity.

In Roman times, continued subsidence forced to incessant repair and rehabilitation of the road *Erculea*, Roman buildings along the coast are gradually reached to the sea, and, around the ninth century AD, the city of Pozzuoli is partially submerged. This phenomenon, which will be explained in more detail in the next section, is called *bradyseism*, and is thought to be probably related to the gradual readjustment of the soil after the release of large volumes of magma (which occurred in previous eruptions).

The last eruption in the Campi Flegrei happened in the 1538, and the volcanologists have tried to reconstruct the eruptive dynamics from the studies of the historical chronicles the detailed study of the deposits.

Around the 1502, the inhabitants of Pozzuoli noted that new stretches of beach are forming and in 1536 begins a new swarm of earthquakes, which become continuous and violent in the last week of September 1538, when the sea retired before the Tripergole village, near the Averno lake.

At one o'clock in the morning of September 29th, near the sea, a bulge comes from the cold water, probably due to the increased pressure caused by magma on the underground aquifer. Quickly this water is transformed into a cloud of steam and mud that rises in the sky, forming a characteristic mushroom-shaped column and destroying a small group of houses, after that begin to be ejected even pumice and scoria.

After this stage, follows a more properly magmatic phase, perhaps with the issue of scoria and pyroclastic flows. The last stage of the October 6th, is characterized by strombolian activity.

In a few days a mound of about 130 m is formed, and is called, with little imagination, *Monte Nuovo* (Vulcani d'Italia - Uniroma3).

The volcanic history of Campi Flegrei cannot be considered completed just because there have been 'only' about five hundred years after that eruption, in which there was a large urban explosion that completely ignores the possible risks too.

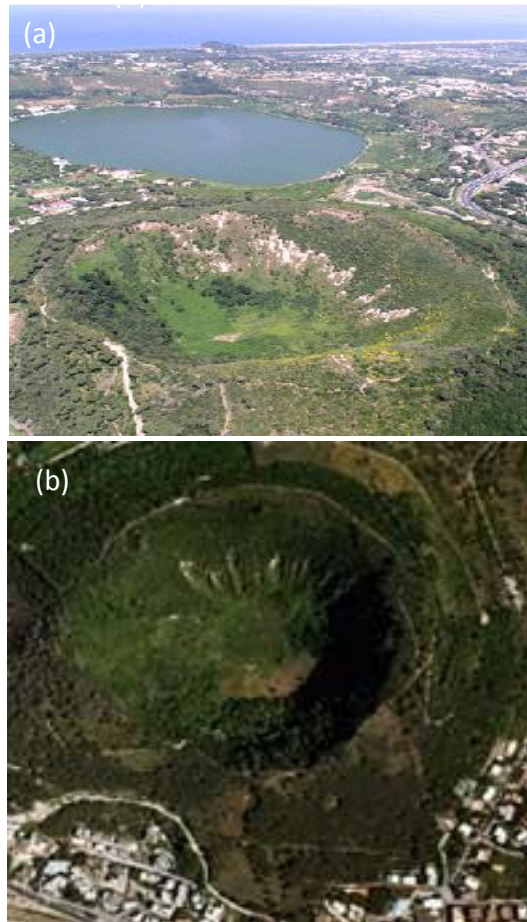


Figure 9 Crater of *Monte Nuovo*, (a) from (Vulcani d'Italia - Uniroma3), (b) (OV-INGV)

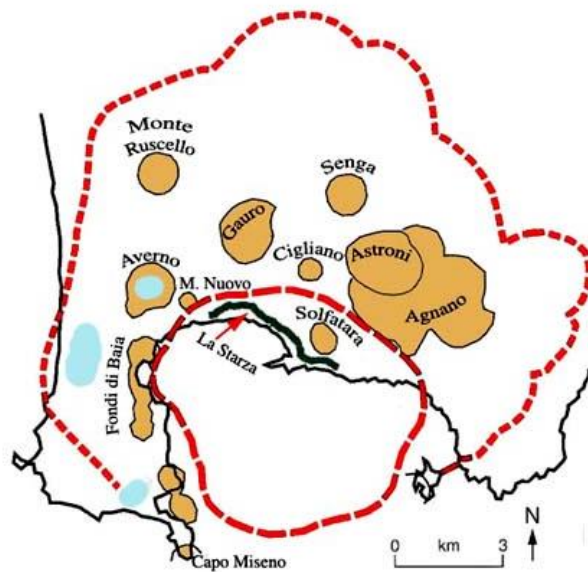


Figure 10 Disposition of volcanic systems in the Phlegrean caldera. The dashed lines approximate the areas of lowering, as a result of the *Ignimbrite Campana* eruption (the external one) and the *Tufo Giallo Napoletano* eruption (the internal). (Vulcani d'Italia - Uniroma3)

4.1 The bradyseism and seismic activity at Campi Flegrei

One of the peculiarities of the Campi Flegrei area is the phenomenon of bradyseism (from the greek 'slow movement of soil'), which consists of a raising of the ground, often very clear, followed by a phase of slow subsidence.

The phases of uplift are usually accompanied by seismic activity, while the phase of subsidence is aseismic (e.g. Saccorotti, *et al.*, 2001, and references therein).

The place that, more than any other, shows this phenomenon is the *Macellum* (roman market better known as the *Temple of Serapis*, Figure 11) located near the port of Pozzuoli. The ruins of this building (which dates from the late first century AD) have been very useful for the reconstruction of bradyseism phases and in particular of changes in soil level compared to the marine's, observing the holes produced, on the columns, from *Lithodomes* (mollusks living in the coastal environment in the limit of the free surface) Figure 11 (Morhange, *et al.*, 2006).

Submersion of Pozzuoli (up to 7 m) wasn't a unique event, but included three maximum threshold oscillations between the fifth and the fifteenth centuries A.D. The first two (400-530 A.D. and 700-900 A.D.) weren't followed by a volcanic eruption, but the last one was culminated with the 1538 Monte Nuovo eruption (Morhange, *et al.*, 2006).

Vertical ground deformation is common in active calderas but they are not always followed by an eruption. Generally, ground deformation is due to an inflation of magma at depth, so it reflects an evolution of magmatic system possibly ending with an eruption.

In the Campi Flegrei case, the hydrothermal fluids circulating between the surface and the magmatic chamber plays an important role.



Figure 11 Temple of Serapis in Pozzuoli (Vulcani d'Italia - Uniroma3).



Figure 12 Submerged Roman port in the gulf between Baia and Bacoli (Vulcani d'Italia - Uniroma3)

In the last four decades, Campi Flegrei caldera has been among the world's most active caldera characterized by intense unrest episodes involving huge ground deformation and seismicity, but has not culminated in an eruption. The most recent high intensity bradyseismic crisis, is in the period 1982-1984 (Battaglia M. , *et al.*, 2006, Petrazzuoli, *et al.*, 1999, Bianchi, *et al.*, 1987). In this period there was a noticeable uplift of 1.8 m in the area of the town of Pozzuoli, accompanied by more than 16,000 earthquakes with maximum magnitude $M = 4$ (these events were recorded by the first mobile digital seismic network, managed by the University of Wisconsin). Since January 1985, began a phase of slow subsidence, interrupted by short phases of uplift in 1989, 1994, 2000 .

Among these episodes, the one of 2000 (July-August) is accompanied by two seismic swarms, the first of which is characterized by long-period events (LP), never recorded in the Campi Flegrei until that time.

Since August 2000, begins a new phase of subsidence until November 2004, which starts a new light uplift (4 cm) ending in October 2006.

In the period between January 1st and April 14th 2006, only seven microearthquakes were recorded in the Campi Flegrei area. However, throughout the second half of 2006, there has been a strong activity, with the highest number of events since 1985. In fact, 1043 seismic events of small magnitude have been recorded, most of which located in the area of the Solfatara: 166 of these were classified as volcano-tectonic and 877 as Long Period (LP). Their localizations are shown in Figure 13:

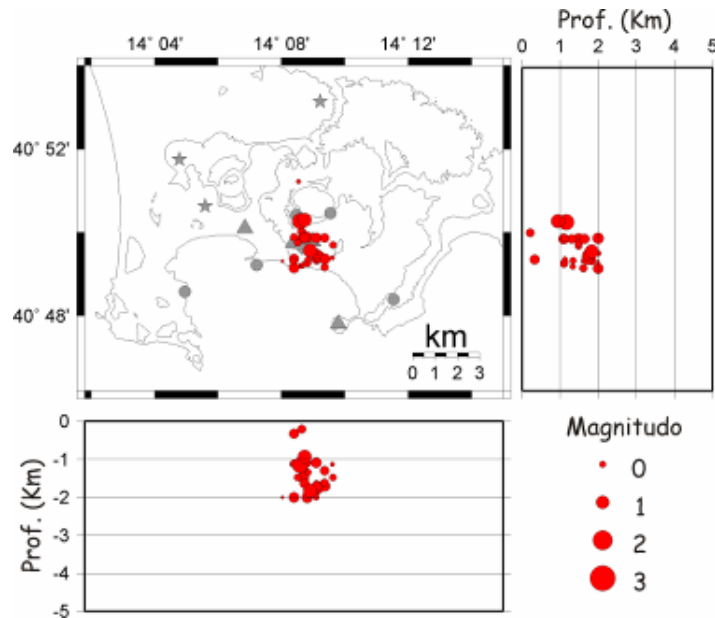


Figure 13 Localizations of VT events, recorded between 19th and 28th October 2006, in the Campi Flegrei Caldera. (OV-INGV)

A summary of the history of ground deformation at Campi Flegrei is represented in the following figure (Figure 14).

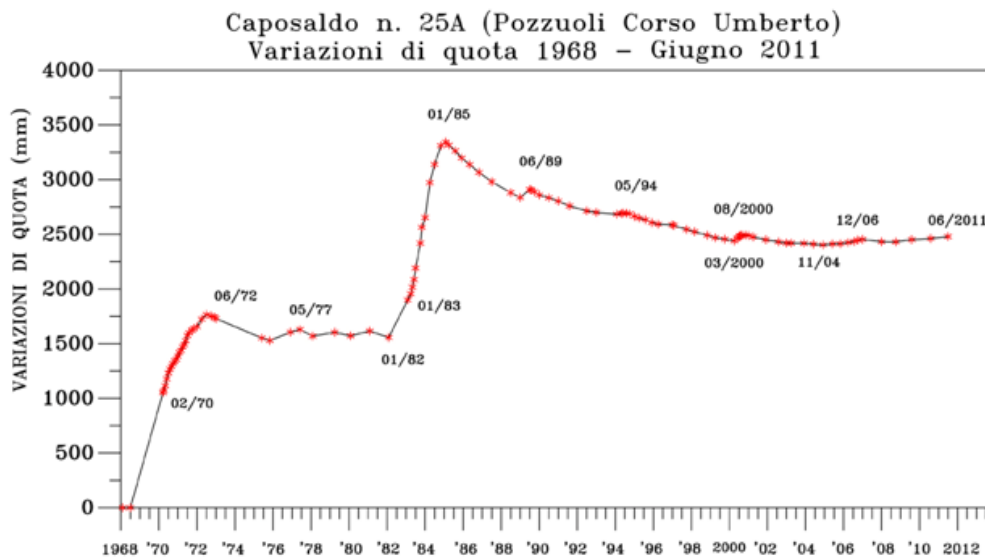


Figure 14 Variations of *caposaldo n.25*, in the Corso Umberto in Pozzuoli city, measured by geometric leveling (OV-INGV).

About the most recent activity in the Phlegrean area, geodetic measurements show a gradual uplift of the ground since 2008 (Figure 15). At the end of 2007, after a period of subsidence following the uplift of 2004-2006 (+ 4 cm), a new phase of uplift occurred, that has continued up through 2010 (average speed of +1 cm/year). Between April and June 2011, the vertical ground deformation rate increased up to 1 cm/month, after then it returned to the previous value. This evolution is well illustrated by the time series of the change in height for the GPS permanent station of RITE, located in Pozzuoli, in the maximum vertical deformation area (Figure 15).

There is an evidence also in the North and East component of GPS measures of ground deformation, in accordance with the inflation phenomenology of the Pozzuoli area during the 2008-2011 period (Figure 16).



Figure 15 Time series from 2006 of the vertical deformation in Pozzuoli, measured by the GPS permanent station (OV-INGV).

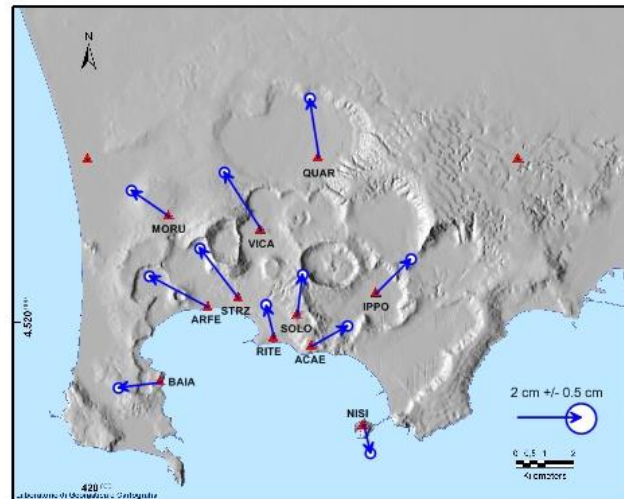


Figure 16 Planimetric displacements in the Phlegrean area in 2008-2011 period (OV-INGV).

About the seismicity, the Campi Flegrei area is characterized by a moderate activity that occurs mostly in swarms and during the deformation crisis the number and the magnitude of the seismic events increase.

Since 2000, 10 seismic crisis with swarms of earthquakes and some individual event occurred. In the beginning of 2011, 62 Volcano-Tectonic events were recorded with magnitude always less than 1 (Figure 17).

These earthquakes are mainly located in the Solfatara, the most active area in Campi Flegrei caldera.

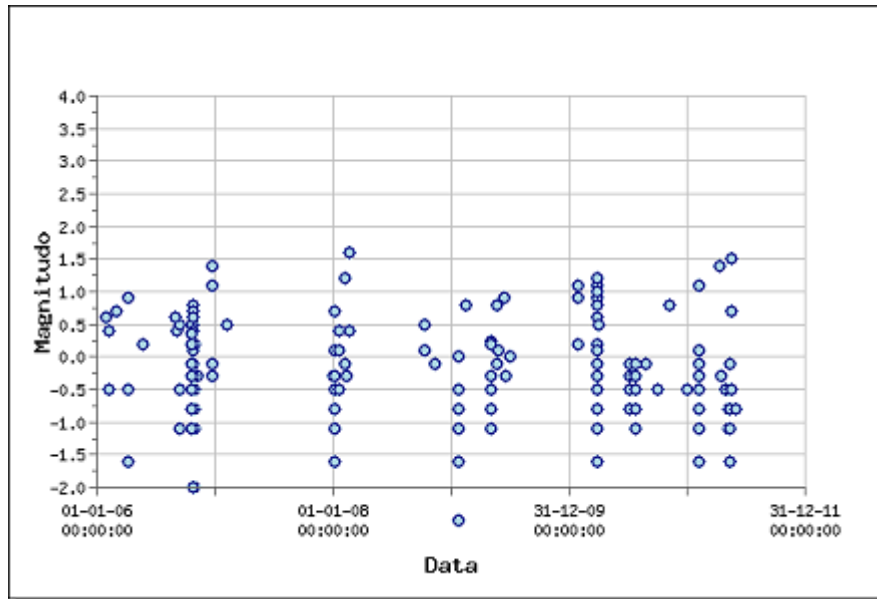


Figure 17 Magnitude of seismic events from 2006 to 2011 (OV-INGV).

In the recent period the dynamic activity at Campi Flegrei caldera increased. Since the end of 2005 up to 2012 the vertical cumulative deformation recorded at the GPS-RITE (Rione Terra) station is of 21 cm (10 centimetres during 2012). The rate of ground deformation in 2012 suffered a rapid increase up to 5 cm/year (Figure 18). On September 2012, 219 earthquakes were recorded in the Campi Flegrei area and the rate of ground deformation reached a value of 1-1.6 cm/month. After this period the seismic activity and deformation went back to the values before this crisis, but at the end of 2012 there was a rapid increasing to 2-3 cm/month and a few number of seismic event. Also the geochemical activity underwent an increasing, mainly in the area of Pisciarelli vent, possibly due to the increasing of rainwater. In the first month of 2013 the ground deformation rate decreased to 1 cm/month (Figure 19) and the seismic activity went back to the background state with just a few small and shallow events recorded in the last months (OV-INGV, Bollettino mensile vulcani campani, 2012) (OV-INGV, Bollettino mensile vulcani campani, 2013).



Figure 18 Vertical ground deformation at the station RITE (Pozzuoli) since 2000 to 31st January 2013 (OV-INGV, Bollettino mensile vulcani campani, 2012).



Figure 19 Temporal series of vertical ground deformation at RITE station (Pozzuoli), since 1st January 2012 to 4th February 2013 (OV-INGV, Bollettino mensile vulcani campani, 2012).

4.2 The seismic network at Campi Flegrei

In order to monitor volcanoes, the principal use of a seismic network is the detection of signals associated to the volcano activity and correlated to the variations of its dynamic state.

Through the detection, analysis and interpretation of the seismic phenomena, the monitoring of volcanic processes aims to report the evolution of volcanic activity leading to a possible eruption in the short or medium term.

The Osservatorio Vesuviano (INGV) manages networks for seismic monitoring of the high risk volcanoes of Vesuvius, Campi Flegrei and Ischia which are high risk volcanoes because of their eruptive style, mainly explosive, and their proximity of large urban areas, and it also provides information on the seismicity at a regional scale measured by the Centralized National Seismic Network (INGV - National Center for Earthquake).

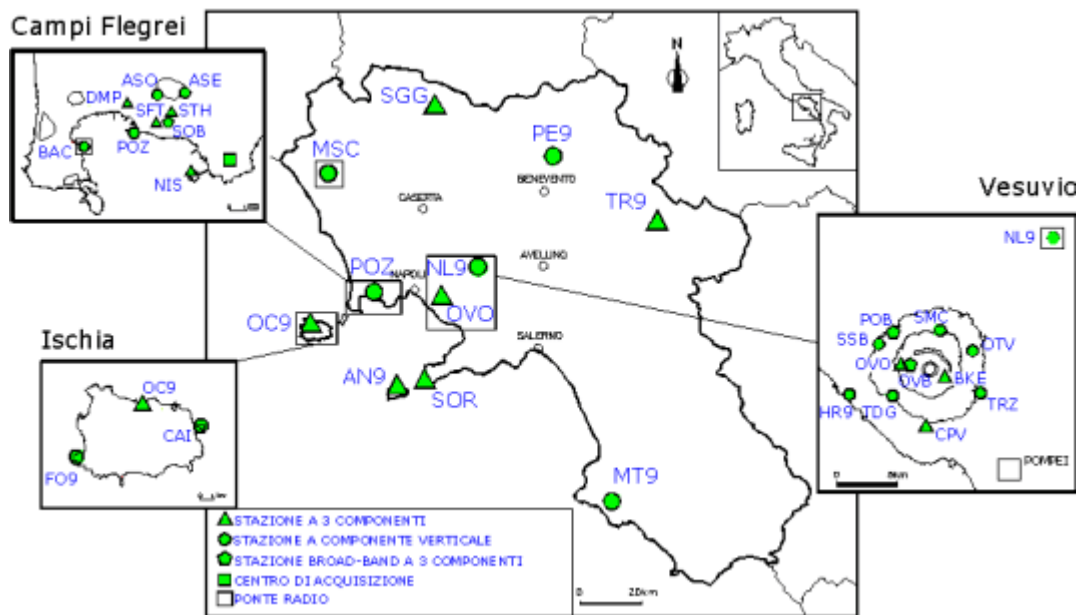


Figure 20 Seismic network of Osservatorio-Vesuviano, (OV-INGV)

The first reports of seismicity for a neapolitan volcano, Vesuvius area, date back to the second half of 1800 (the electromagnetic Palmieri seismometer – 1856).

In the second half of 60's four stations were operating at the Vesuvius volcano, equipped with electromagnetic seismometers Hosaka and smoked papers records.

The first stations equipped with modern instrumentation (electromagnetic seismometers, frequency modulation, radio and telephone) date back to the early 70's.

Over the years, the Osservatorio Vesuviano Seismic Network was expanded both in number of stations, instrumentation and data acquisition systems. This enhancement has significantly lowered the detection threshold of the network, by doubling the number of localizable events and increasing the number of recorded signals with a high signal-to-noise ratio.

The complete seismic network that recorded the 2006 events at Campi Flegrei is in Figure 21 and consisted of:

- 10 analogic stations, three components and short period;
- 1 digital station, three components and short period;
- 8 stations, three components and broad band;
- 1 seismic antenna equipped with 5 sensors, three components and short period, plus 1 accelerometer.

The complete seismic network operating at Campi Flegrei area is illustrated in the following figure (Figure 21).

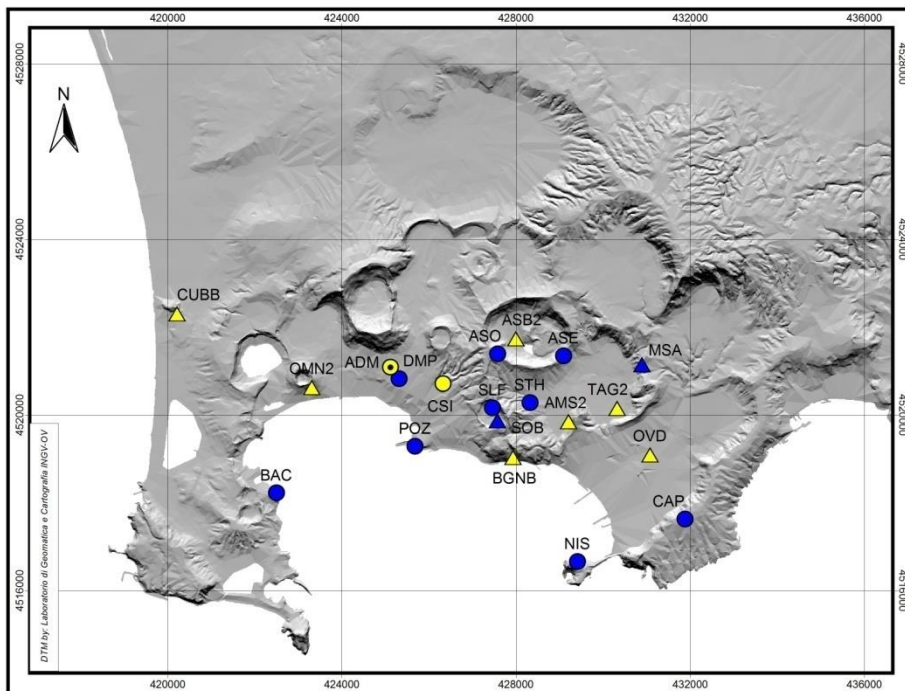


Figure 21 Map of Osservatorio Vesuviano seismic network operating at Campi Flegrei area (OV-INGV). Blue symbols refers to the permanent network and yellow symbols to the temporary one. Stations equipped with short period sensor are marked with circles and the triangle are used for the broadband sensor stations. The circle with the black point inside refers to the array (Saccorotti, *et al.*, 2007).

5. The October 2006 seismic events at Campi

Flegrei

After the seismic swarm of October 2005, in October 2006 started a new seismic crisis, consisting of approximately 160 microearthquakes ($M \leq 0.8$) (Volcano-Tectonic events), recorded in the period from October 19th to 30th, 2006.

This activity was also followed by several hundreds of weak events with a monochromatic low frequency spectra, peaked at frequencies between 0.7 and 1 Hz. These events have a lack of clear S-wave arrival, a spindle-shaped waveform and were classified as Long-Period events. Their activity climaxed on October 27th, 2006, about one day after the most intense VT activity (Figure 22) (Saccorotti, *et al.*, 2007).

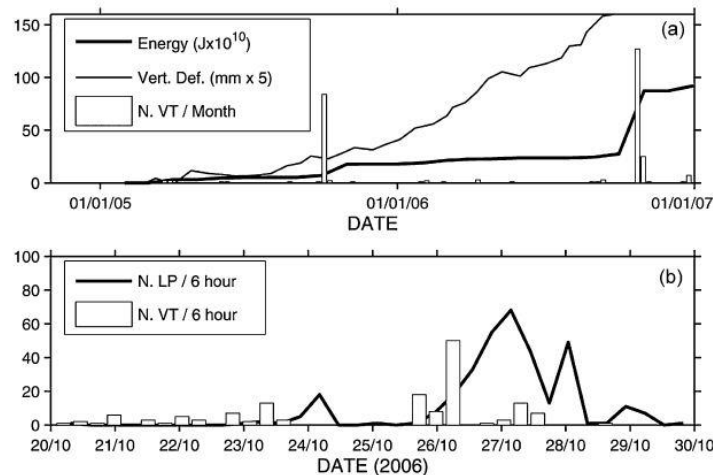


Figure 22 (a) Number of VT earthquakes, energy release and ground vertical deformation in Pozzuoli, from GPS measurements. (b) Number of VT and LP earthquakes during 6 hours in the 20th-30th October 2006 crisis (Saccorotti, *et al.*, 2007).

The last VT swarm occurred on December 21st, 2006, with highest magnitude of the entire period ($M=1.4$).

The sources of most of the VT seismicity of October 2005 and October 2006 are clustered at depth spanning from 1 Km to 4 Km beneath the Solfatara crater. The origin of the December 2006 swarm is localized at depth from 1 Km to 2 Km under the Astroni crater.

Focal mechanisms, show a class of normal solutions with nodal planes rotating from N-S to NNE-SSW and finally to NNW-SSE (Saccorotti, *et al.*, 2007).

About the Long Period events, several factors, as the absence of the same frequencies peaks in either the earthquake and the noise spectra, the presence of the same peak among all the stations of the network, suggest that they reflect a source effect.

The waveforms of the Long Period events can be grouped in three clusters (Figure 23) with similar locations along the S-E rim of the Solfatara at a depth of 500 m (Saccorotti, *et al.*, 2007), (Figure 24).

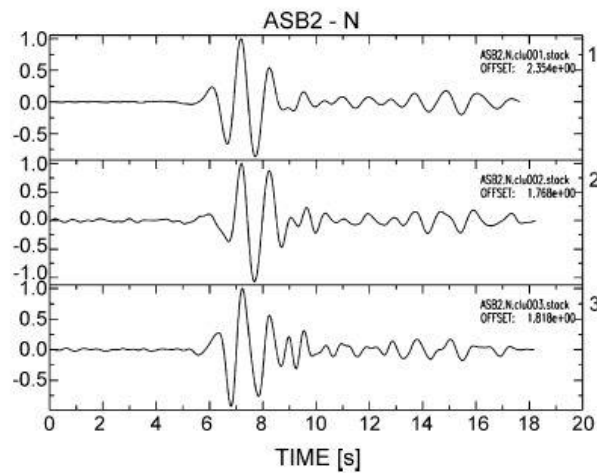


Figure 23 Stacked velocity seismograms for the three clusters, from the NS component of station ASB2, individually normalised to their maximum amplitude (peak-to-peak) (Saccorotti, *et al.*, 2007).

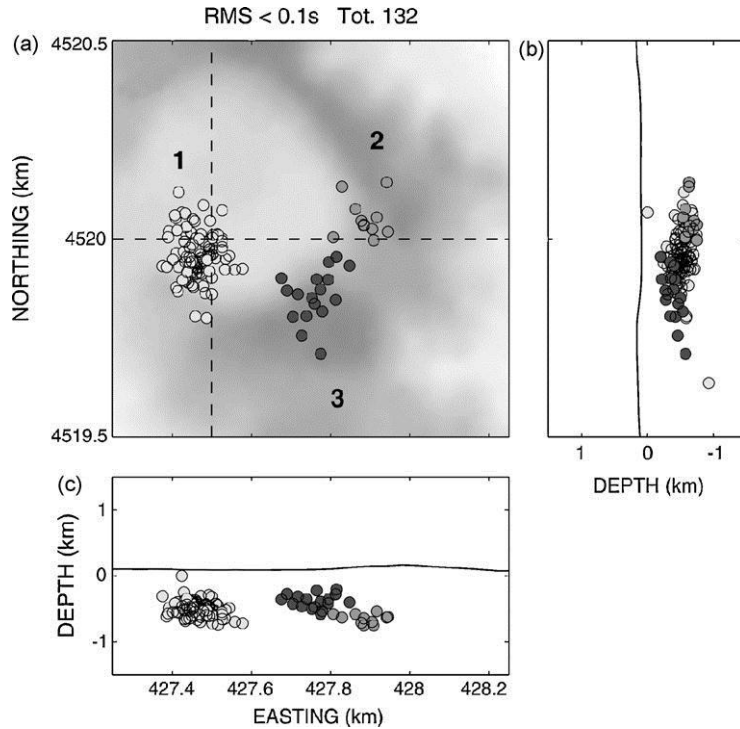


Figure 24 Locations of the three clusters of LP events, superimposed to a map of the Solfatara Volcano (Saccorotti, *et al.*, 2007). The three colors are relative to the three clusters of events (Saccorotti, *et al.*, 2007).

The monochromatic character of the LP oscillations and the similarity of the stacked waveforms suggest that this signal are generated by a non-destructive process of resonance, probably the harmonic oscillation of a fluid filled crack repeatedly triggered by very impulsive pressure boosts (Saccorotti, *et al.*, 2007).

To better understand the source of this low frequency seismicity and the characteristics of the fluids involved in the resonance processes, following the Chouet theory (Chouet, 2003) and using the power spectra of those LP, the quality factor of the resonator (different from the quality factor of the Earth medium) and the dominant frequency were estimated (Saccorotti, *et al.*, 2007, Figure 25).

From the relationship (Eq. 3):

$$Q = \frac{f}{\Delta f}$$

Eq. 3

where f is the frequency of the dominant spectral peak and Δf is the width of that peak at half of the peak's magnitude, the quality factor Q of the resonator cavity could be obtained.

Using the radial components of the waveforms recorded at the ASB2 station (the one with the highest SNR), a quality factor peaked around the value 4 is obtained (Saccorotti, *et al.*, 2007).

The values of Q could span over a wide range (10-500, from literature), reflecting the contrast of different physical properties between the multiphase fluid and the matrix of the surrounding rock (Kumagai, *et al.*, 2002). In our case we can interpret the values of Q , in terms of a contrast of very low impedance at the fluid-rock interface preventing the trapping of elastic energy in the crack.

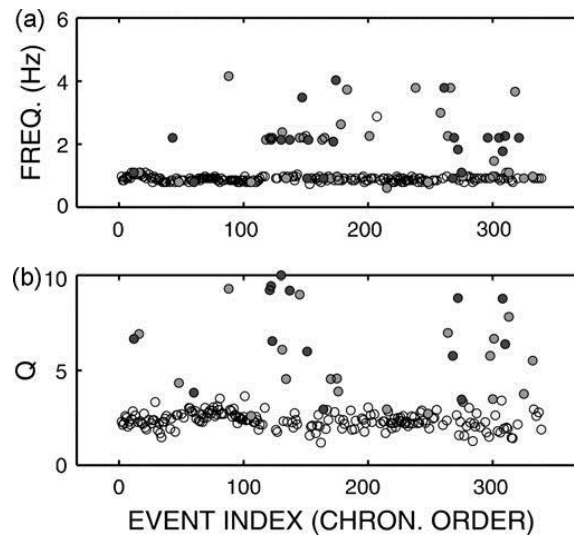


Figure 25 Dominant frequency (a) and quality factor (b) for the radial component of the LP events at station ASB2. Different tones correspond to event of different cluster (Saccorotti, *et al.*, 2007)

Applying the measured quality factor to the crack-like geometry proposed by Chouet (Chouet, 2003) and considering the shallow depth of the LP source (500 m), the most likely candidate for the source process generating those LP events is a vibrating fracture filled with water vapour mixed with a low gas content (maybe the hydrothermal system of Solfatara volcano, extending over the 0-1500 m depth range) (Cusano, *et al.*, 2008).

The crack length is between 40 m and 420 m, a size range which is consistent with the spatial spreading of the LP hypocentres (Cusano, *et al.*, 2008).

Hence the October 2006 crisis can be explained in terms of fluid exchange between a deeper and a shallower reservoir beneath the centre of Pozzuoli (Battaglia M., *et al.*, 2006). Possibly an overpressure in a cavity at 3-4 Km of depth containing fluids of magmatic origin, may have been caused a batch of magma rich in gas, from a deep source (Troise, *et al.*, 2007).

This pressurization, in addition to the deformation, caused brittle failure in the above rigid layer, producing the VT events, occurring during the uplift phase.

The pressurization increased the permeability of the soil allowing the migration of the fluids and inducing the LP resonance events in the shallow hydrothermal system of the Solfatara (Saccorotti, *et al.*, 2007). This caused an increasing of the temperature and velocity of the gases at the fumaroles (Cusano, *et al.*, 2008) (Figure 26).

This scenario clarifies the role of the hydrothermal systems beneath the volcanoes: it induces ground deformations and LP activity and it amplifies the response to the arrival of fresh magmatic fluids from the depth.

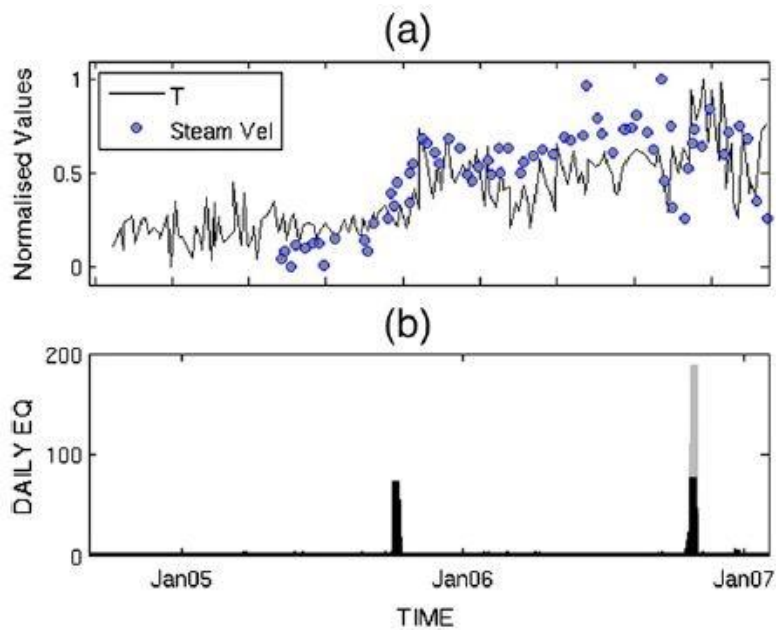


Figure 26 (a) Daily average temperature (infrared measures) at Bocca Grande fumarole of Solfatara (solid line) compared with the steam velocity at the same place (grey dots). The values are normalized. (b) Daily numbers of VT (black line) and LP (grey line) activity (Cusano, *et al.*, 2008).

The scenario suggested for the October 2006 crisis is illustrated Figure 27 (Saccorotti, *et al.*, 2007).

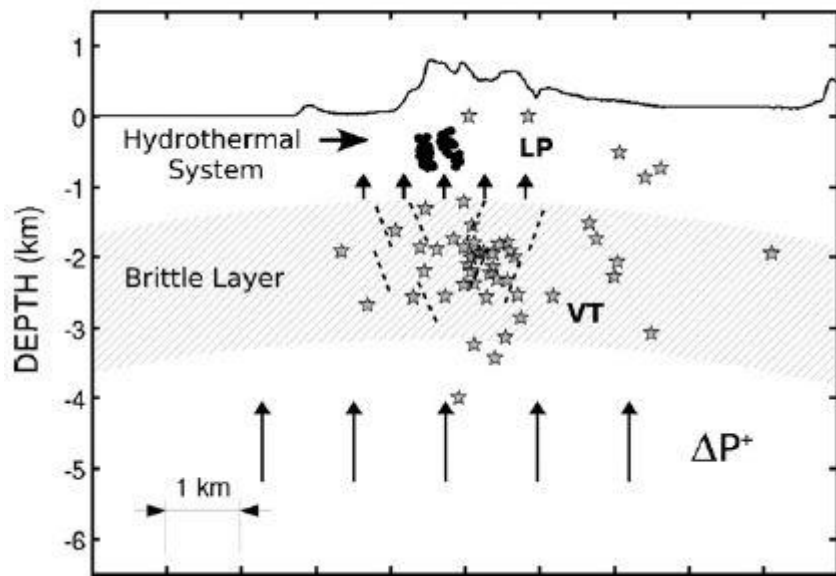


Figure 27 Possible scenario for the 2006 crisis at Campi Flegrei (Saccorotti, *et al.*, 2007).

6. Data analysis – first step

In this chapter, the different steps of the analysis of the LP seismic data will be illustrated.

After the first step in which the waveforms and their characteristics will be studied, the different procedures adopted for the determination of the duration and the energy of that seismic events will be described.

In particular in the first step, the energy will be estimated through the envelope of the waveforms searching for a relation with their durations. During this phases lots of routines were developed to better understand the seismicity in order to quantitatively define the right parameters in the final analysis.

6.1 Preliminary analysis of the waveforms

In order to have the best data set possible, we chose the seismic stations whose waveforms presented the highest value of the SNR: ASB2, TAGG, AMS2, BGNB (Figure 28). The selected seismic stations are all equipped with digital 3C broadband velocimeters and they are localized near the epicentres of the events recorded on the October 2006 and analysed in this work (see Figure 28).

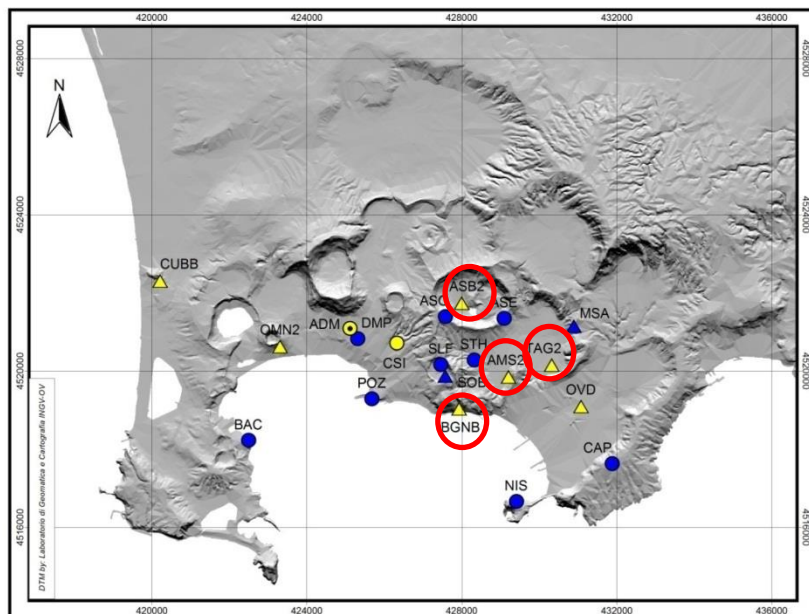


Figure 28 Seismic network in the Campi Flegrei area. Highlighted in red are the stations whose waveforms are used in this work (OV-INGV).

The waveforms have been bandpassed using a 'Butterworth' filter, with 3 poles and 3 zeros, between 0.2 Hz and 1.2 Hz for the ASB2, AMS2 and TAGG stations, and between 0.5 Hz and 1.5 Hz for BGNB.

An example of 3C waveform for each station is reported in the Figure 29, Figure 30, Figure 31 and Figure 32, for the event recorded on October 26th 2006 at 00:05 at the four different stations. Hereafter we refer to this event as the "sample event".

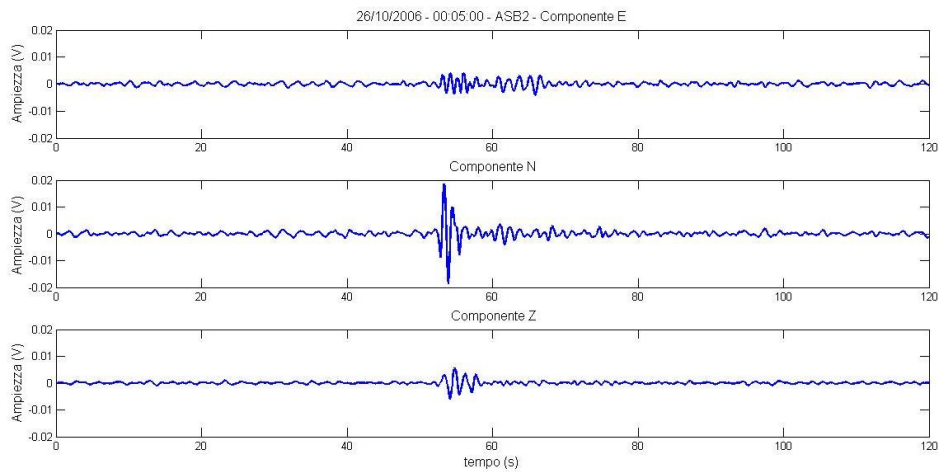


Figure 29 Three components of the event recorded on October 26th 2006 at 00:05 at the ASB2 seismic station.

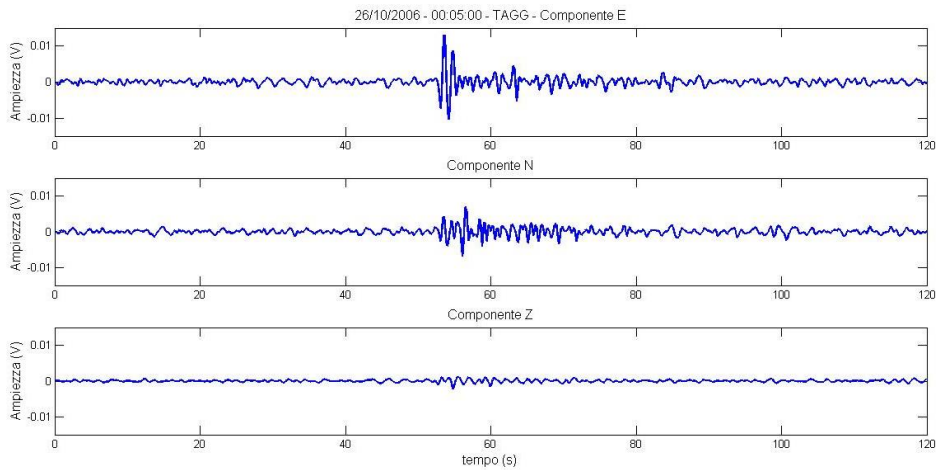


Figure 30 Three components of the event recorded on October 26th 2006 at 00:05 at the TAGG seismic station.

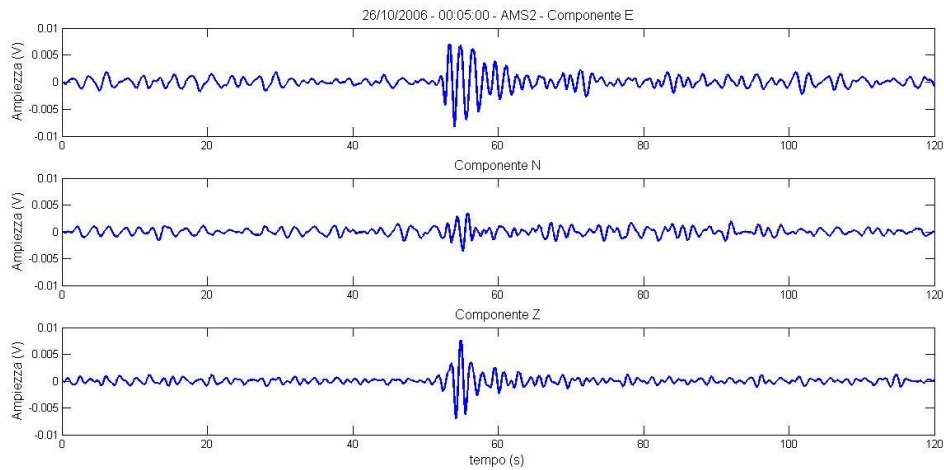


Figure 31 Three components of the event recorded on October 26th 2006 at 00:05 at the AMS2 seismic station.

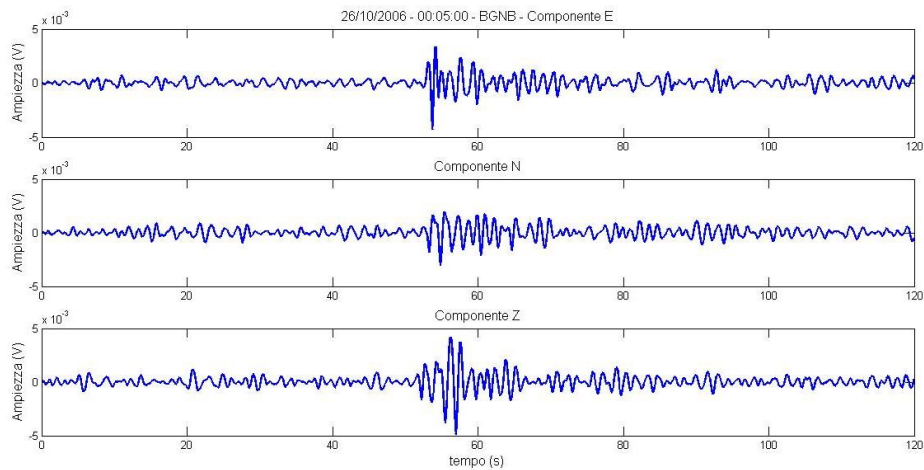


Figure 32 Three components of the event recorded on October 26th 2006 at 00:05 at the BGNB seismic station.

Choosing waveforms with the highest signal to noise ratio (hereafter SNR), drastically reduced the number of treated events.

The analyzed LP seismicity (actually for the LP seismicity in general) is characterized by an unclear onset and end of the waveform. This evidence, combined with the low SNR, forced to develop a supporting function for manual detection of the onset of the seismic impulse, in addition to the formulation of algorithms useful to the identification of the duration (Section 6.2).

Observing the waveforms, could be noticed, in some components of each seismic station, a repetitive waveform occurrence, with amplitude often gradually lower than the first one (Figure 29, Figure 30, Figure 31, Figure 32). The presence of this kind of 'sub-events', even if it goes beyond this work, will be a little better studied in a dedicated Section (Section 6.4.2).

6.2 Duration of the events

Duration-magnitude scale are widely used in the volcanic observatories practice, generally to furnish quantitative evaluation of the energy associated to volcano-tectonic events. At first step, we were interested in trying to find a duration-magnitude calibrated scale for routine rapid estimations of the energy content for the LP seismicity too.

The differences of the LP's waveforms respect to the tectonic seismicity involve also the difficulties in measuring their onset and their exact time duration. To achieve this goal different procedure have been developed. The duration of the LP was visually selected from the waveforms or from some supporting functions (root-mean-square (RMS) or amplitude-envelope), or automatically checked through two different routines based on the envelope or the RMS of the waveforms.

The three methods proposed will be discussed in the following paragraphs.

6.2.1 Duration – visually selection

It's not easy to estimate the duration of a low frequency seismic event, due to its emergent onset and to the coda decaying masked into the noise.

Accordingly, we used two different supporting-function for the visual inspection of the waveforms, that helped us in this step of the study.

The first function has been derived by the method adopted in the dissertation of Petrosino, *et al.*, 2007; it is based on the features of a function obtained through the Root Mean Square (RMS) of the signal.

We proceeded in the following way:

- each seismogram has been divided into many intervals of length 0.25 seconds. This duration window is chosen in order to reduce the noise-fluctuations that could masks the real trend of the final function.
- for every time window the RMS was calculated (Eq. 4). So we obtained a value of RMS every 0.25 s of signal.

$$RMS = \sqrt{\frac{\sum_{i=1}^N y_i^2}{N}}$$

Eq. 4

where y_i is the waveform amplitude and N the number of the intervals.

- the value obtained for every time window was then multiplied by each value of the times of all the recording, obtaining a function which, for sake of simplicity, we will call RMST (Eq. 5).

$$RMST = \left(\sqrt{\frac{\sum_{i=1}^N y_i^2}{N}} \right) \cdot t_n$$

Eq. 5

where n is the indices of each point in the signal array.

The obtained curve is very helpful in selecting the duration of these events (Petrosino, *et al.*, 2007); in fact, plotting Eq. 5 as a function of time, it shows a rapid increasing that corresponds to the impulse arrival and, after having reached a maximum, it decreases more or less rapidly until it reaches a minimum value, beyond which it starts to rise again. The time corresponding to this minimum, marks the end of the useful signal (Figure 33).

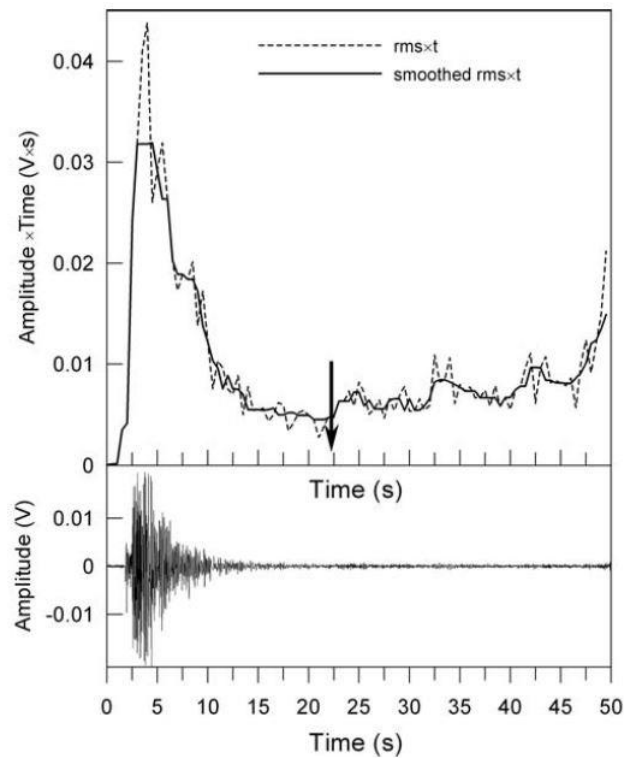


Figure 33 The function RMST (dotted line) calculated for the VT waveform in the lower panel (Petrosino, *et al.*, 2007).

In fact, before the seismic arrival, the RMS is sensible to the background noise of the seismogram, so its amplitude is very low and even if multiplied by the time it won't undergo major changes. On the contrary, after the arrival of the

signal, the value of the RMS, and consequently of the RMST, sharply increases.

Only after the end of the signal, the RMS resume very low values, which, however, multiplied by a growing time, and greater than those in the first part of noise (before the seismic impulse), are responsible for an increasing of the RMST function.

To better visualize the function RMST and minimize the fluctuations due to the noise, this function is applied to the waveform envelope. The envelope is calculated through the Hilbert Transform. Since the Hilbert Transform of a function has the characteristic of being out of phase with respect to the starting function (Figure 34), the envelope has been obtained by means of the following formula:

$$I(t) = \sqrt{x(t)^2 + \bar{x}(t)^2}$$

Eq. 6

where $x(t)$ represents the signal and $\bar{x}(t)$ is its Hilbert Transform.

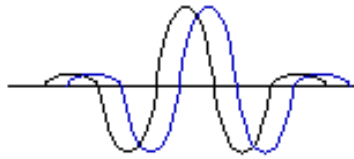


Figure 34 Superposition of a signal (black line) and its Hilbert Transform (blue line).

Applying the function RMST to the envelope we were able to select the signal in each recording and to obtain, than, its duration; however sometimes the duration estimate was difficult due to problems in the identification of the end of the signal.

In Figure 35 an example of the seismogram and the related RMST function is illustrated.

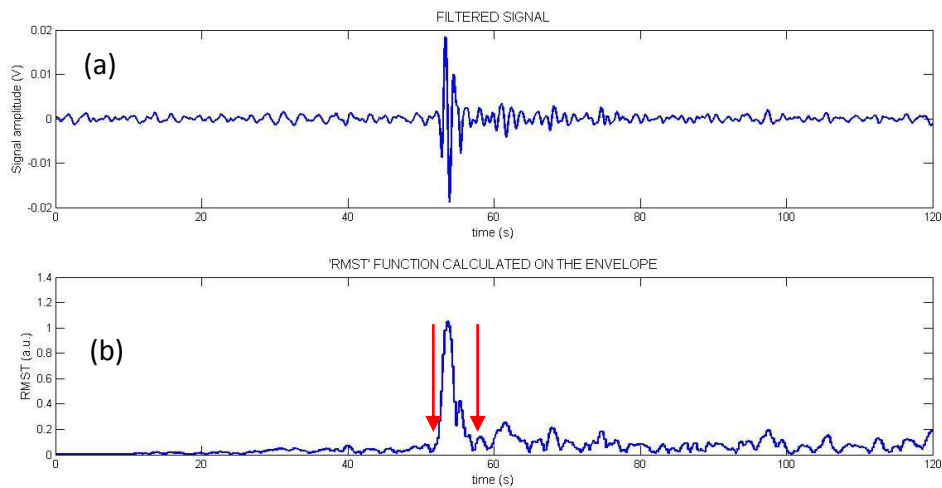


Figure 35 (a) Waveform (filtered between 0.2 Hz and 1.2 Hz) of an event of 26th October 2006 at the ASB2 seismic station; (b) its function RMST. The red arrows correspond to the arrival time and the end of the seismic impulse.

The second developed supporting-function is based on a kind of envelope of the waveforms. We decided to use an *amplitude-envelope* that refers to the changes of the waveform amplitude over the time. To develop it, we calculated the envelope linking the maximum of the modulus of the amplitude at several times. The complete array of the waveform was divided into intervals of a fixed duration. The time-step was chosen to “enough” reduce the noise fluctuations and to obtain a function that well approximated the waveform trend, at the same time.

For each interval the maximum of the modulus of the waveform amplitude was calculated and saved together with the corresponding time value. So we obtained an array of times correlated to the original ones (in this way, the comparison of the envelope with the original waveform was possible) and the corresponding values of amplitude envelope (See panel (b) in Figure 36).

To better select the duration we denoised the envelopes subtracting the average of 10 seconds of noise envelope (the amplitude of the envelope several seconds before the seismic impulse) (see panel (c) in Figure 35).

So we visually inspected the envelopes selecting the onset and the end of them and using these to determine the duration (panel (c) in Figure 36).

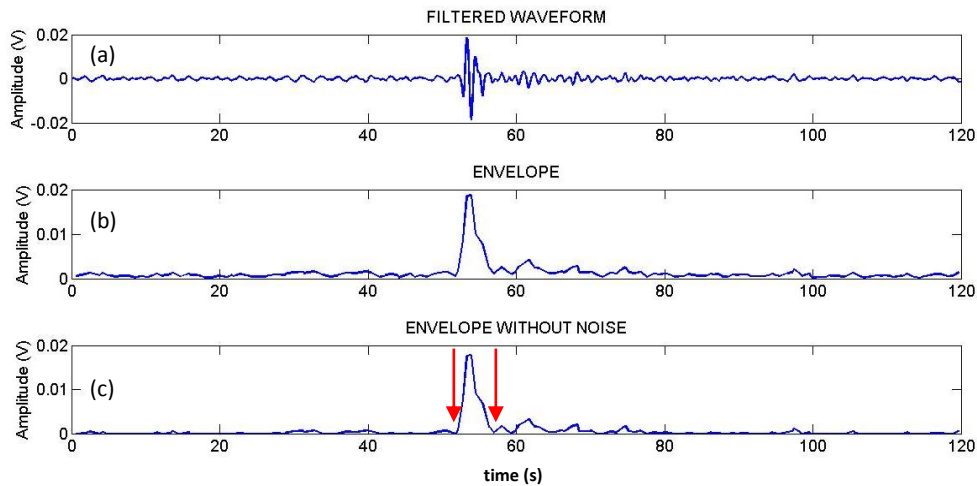


Figure 36 (a) Waveform (filtered between 0.2 Hz and 1.2 Hz) of an event of 26th October 2006 at the ASB2 seismic station, (b) its envelope, (c) the envelope denoised. The red arrows correspond to the arrival time and the end of the seismic impulse.

In the definition of the amplitude envelope, the time interval, at which the maximum of the amplitude are selected, is very important, because a very short step doesn't smooth enough the outline but, if it is too long it could hide the exact time to select.

Both the developed supporting-functions greatly helped us in the onset identification and duration selection, even though sometimes, to better mark the end of signals, the visual inspection of the original waveform was necessary.

6.2.2 Duration routines

In order to improve the previous procedures and make them usable in case of a large data set, we decided to develop some Matlab routines to determine the arrival time and the duration of the seismic impulse.

We decided to develop two routines based on different types of envelope: one obtained through the amplitude-envelope, and the other obtained through the RMS function.

First of all, these two routines were applied to the waveforms recorded at ASB2 since they showed the highest SNR of the entire data set.

6.2.2.1 Duration routine using the amplitude-envelope

This method is based on the calculus of the amplitude-envelope of the waveform (for the amplitude-envelope definition see Section 6.2.1).

The first step is to estimate the threshold to define the first arrival of the impulse. This is defined by computing the average amplitude value for 10 seconds of envelope at the beginning of the seismogram, where there is the contribution of only seismic noise. At this point, the routine scans the entire envelope and, the point for which the amplitude is larger than the threshold multiplied by a coefficient (greater than one) defined by the user, for more than a number of points defined by the user as well, is saved as the first arrival of the impulse. Then the routine continues to scan the envelope and, the time corresponding to an amplitude value lower than the threshold (multiplied by a coefficient different from the first one), for more than a number of points defined by the user, represents the end of the impulse.

To avoid mistakes selecting the wrong impulse, the routine saves the waveforms only if their envelope maximum is not less than another threshold defined as the maximum of the envelope multiplied by a coefficient between 0 and 1.

This procedure was applied to each component for each event in order to have a large data set and make the statistical results more reliable.

The results are represented in Figure 37 (red dots).

6.2.2.2 Duration routine using root-mean-square

This routine follows the same steps of the previous one but, instead of the envelope, it uses the Root Mean Square (RMS) to analyze the waveforms.

The RMS is calculated as described in the section 6.2.1.

Once calculated the RMS the routine works in the same manner as the previous method based on the envelope. So for the first step the threshold is estimated to define the first arrival of the impulse. This is defined by computing the mean of 10 seconds of the RMS at the beginning of the seismogram before the seismic impulse.

If the amplitude of the RMS, in the entire seismogram, is more than the threshold multiplied by a coefficient (more than one) defined by the user, for more than a number of points defined by the user as well, the corresponding time is saved as first arrival of the impulse. Then, if the RMS amplitude after the first arrival time, is less than the threshold (multiplied by a coefficient different from the first one) for more than a number of points defined by the user, the end of the impulse is defined.

Also in this case the waveforms are saved only if the RMS maximum is not less than another threshold defined as the maximum amplitude of the original waveform multiplied by a coefficient between 0 and 1.

A comparison between the results obtained through the two different routines is reported in Figure 37 where the results corresponding to each component of the ASB2 waveforms are represented.

The two envelope-routines are applied to each waveform and represented, on the same x-axes value, using two different colors (Figure 37): the blue dots for the amplitude-envelope routine and the red dots for the RMS routine.

The integer numbers of the x-axes in Figure 37 represent the different events, each number refers to one event and for each of this, in the y-axes, the two different values of duration obtained by the different routines are shown.

The results prove that different values of the duration can be obtained using different function, so, for this reason and for a good stability of the results, we decided to not use the routines showed in this section and we selected the duration visualizing the waveforms simultaneously with the amplitude-envelope or the RMST supporting functions (Section 6.2.1).

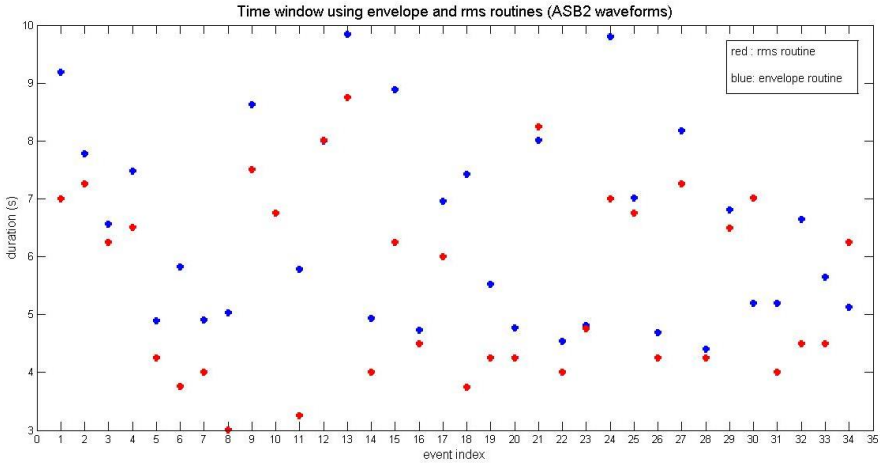


Figure 37 Comparison between the duration obtained through the two different duration-routines (using the amplitude-envelope (red dots) and the RMS (blue dots) of the waveform) applied to the ASB2 waveforms. Each integer number (event index) on the x-axes refers to a different event.

6.3 Energy estimates – first step

The main purpose of this study is to estimate the magnitude of the low frequency seismic events. In order to achieve this goal, the first step is the estimate of the energy related to the LP seismicity. In the follow we will discuss the different methods adopted to calculate the energy of the LP events of October 2006 at Campi Flegrei caldera.

We used two different methods for energy estimation:

1. The first one is based on the calculation of energy through a theoretically obtained formula, depending on the amplitude of the waveform, on its dominant frequency and on parameters related to the propagation of the wave in the medium (propagation speed, density...).
2. The second one is based on the calculation of the envelope of the waveform and of the relative area (once subtracted the background noise). This particular routine has been applied both to individual waveforms and to the average of the envelopes of the two horizontal components of each seismic event.

6.3.1 Energy via theoretical formula

This method has been used in the *master thesis* and modified through this work.

In order to obtain a big and statistical significant data set, all the components of each event have been used.

Considering a pointing source producing a wave train that propagates in every direction (Kasahara, 1981), we suppose that the seismic wave reaches the station at the epicenter (Figure 38) and we represent it using the displacement equation of the soil (Eq. 7):

$$x = a_0 \cos\left(\frac{2\pi t}{T_0}\right)$$

Eq. 7

where a_0 and T_0 indicates the wave amplitude and the period, respectively.

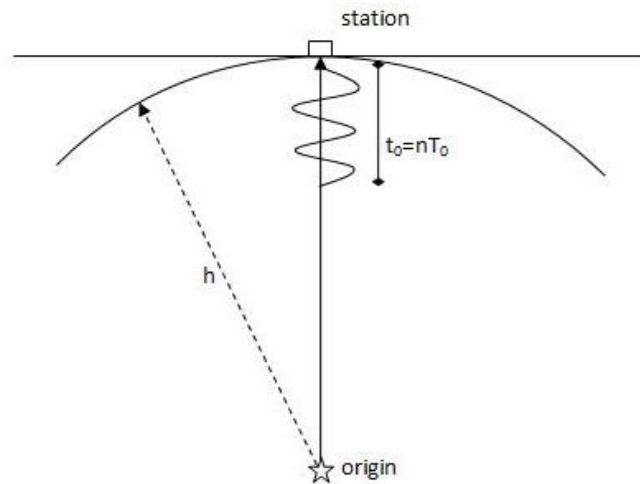


Figure 38 Seismic wave arrival at the surface (Kasahara, 1981).

Consequently, the velocity is given by the time derivative of the displacement:

$$v = -\frac{2\pi a_0}{T_0} \sin\left(\frac{2\pi t}{T_0}\right)$$

Eq. 8

The kinetic energy density per volume unity \mathcal{E} , is then:

$$\mathcal{E} = \left(\frac{\rho}{2T_0}\right) \int_0^{T_0} v^2 dt = \left(\frac{\rho}{2T_0}\right) \left(\frac{2\pi a_0}{T_0}\right)^2 \int_0^{T_0} \sin^2\left(\frac{2\pi t}{T_0}\right) dt = \left(\frac{\rho}{4}\right) \left(\frac{2\pi a_0}{T_0}\right)^2$$

Eq. 9

where ρ is the density of the half-space, t_0 is the duration of the wave-train with n waves of period T_0 , and velocity c of the sound in the halfspace.

So, the energy flux per surface unit is: $ct_0\mathcal{E}$, and, if integrated on a h ray surface (see Figure 38), we have the total kinetic energy at the origin:

$$E_k = 4\pi h^2 ct_0 \rho \left(\frac{a_0}{T_0}\right)^2$$

Eq. 10

Taking into account some considerations (Kasahara, 1981):

- the kinetic and potential energy are the same, so the total energy will be $E = 2E_k$;
- the amplitude doubled at the epicentre (free surface), so $a_0 = 2a$, where a is the wave amplitude at the hypocentre and a_0 represents the amplitude at the free surface;
- the previous calculations are for the S wave. The P wave energy is assumed to be half of the S one;

we obtain the following expression for the energy estimate:

$$E = 3\pi^2 h^2 c t_0 \rho \left(\frac{a_0}{T_0} \right)^2$$

Eq. 11

where h is the depth in meters, t_0 and T_0 are, respectively, the duration and the period in seconds, c is the velocity in m/s, a_0 is the amplitude measured in meters and ρ is the density of the half-space in Kg/m^3 . For the LP studied, the wave velocity is 2000 m/s, the density 2000 Kg/m^3 and the depth 500 m.

To apply the Eq. 11 we used the dominant frequency obtained from the maximum of the amplitude spectrum, and the amplitude a_0 obtained from the maximum amplitude of the modulus of the signal (seismogram corrected taking into account the transfer function of the instrument).

First of all we applied this method to the ASB2 waveforms since they showed a better value of SNR, so, in Figure 39 the energy values are plotted versus the duration of the signal, in order to find a correlation between the two variables.

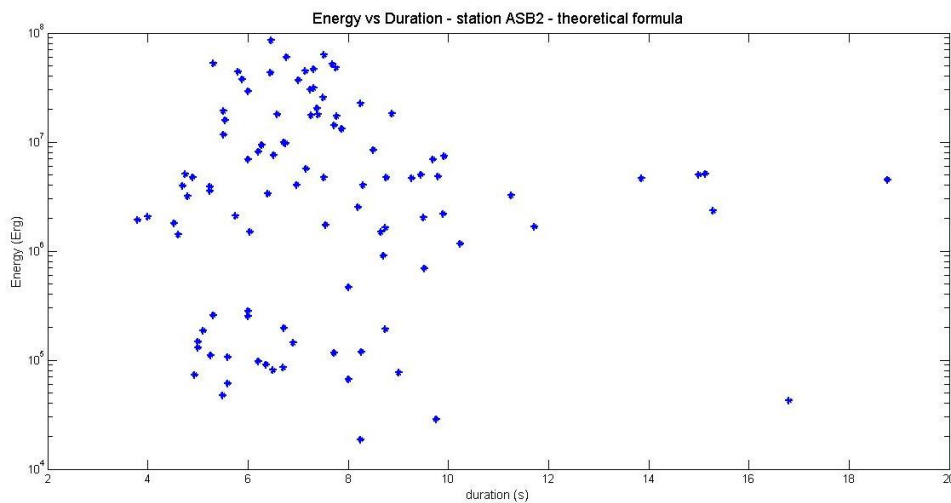


Figure 39 Energy vs duration for each component of every seismic event (semi-logarithmic scale) of the ASB2 seismic station, obtained using theoretical formula.

A non-correlation between energy and duration is evident in Figure 39. Just to confirm this results we calculated the correlation coefficient, that is -0.123. The modulus of this value is less than 0.3 so it reflects a non-correlation between the two variables.

6.3.2 Energy via envelope

The previous described approach about the energy evaluation (Section 6.3.1) is strongly dependent on the duration of the signal and on parameters typical of the area under study (propagation speed, density...). So, as second approach, we decided to evaluate a variable proportional to the energy of the signal using only some feature of the waveform itself, such as the envelope.

We assumed that velocity waveforms are representative of the kinetic seismic energy density at a specific location, and the potential energy density, for the equipartitioning of the energy, is equivalent to the kinetic one. This method is widely diffused in acoustic signal analysis, where the 'relative energy' associated to a signal is evaluated as the Measured Area under the Rectified Envelope (MARSE) (Lucas, McKeighan, & Ransom, 2001).

We calculated a variable proportional to the energy by integrating the seismic signal envelope over a time that corresponds to the entire duration of the transient. The envelope has been obtained connecting the maximum of the modulus of the waveform every fixed number of points (like in Section 6.2.2.1). The integral was calculated from the signal onset until the time that corresponds to the point where the amplitude returns less than the background noise.

In particular we applied this procedure in two different ways:

1. We calculated the envelope of every waveform, and then, for each of these we calculated the integral;
2. we calculated the average of the envelopes of the two horizontal components of each event (N-S and E-W) and for each of these we selected the duration and computed the integral.

6.3.2.1 *Envelope of the single waveforms*

For each waveform we calculated the integral for a selected time duration. We decided to select the duration visually inspecting both the waveform and the envelope.

First of all, we applied the envelope calculus on the filtered signal (Butterworth band pass filter between 0.2 Hz and 1.2 Hz for the waveforms recorded at the seismic stations ASB2, TAGG and AMS2; from 0.5 Hz and 1.5 Hz for the BGNB signals) to reduce the noise fluctuations. To avoid the contribution of the background noise we subtracted the average of 10 s of noise envelope (measured before the seismic impulse) to the entire envelope. In Figure 40 the waveform of the N-S component of the sample event recorded at the seismic station ASB2 is shown in the panel (a), in the panel (b)

the envelope is represented versus time and in the panel (c) the envelope after subtracting the 'noise' is plotted.

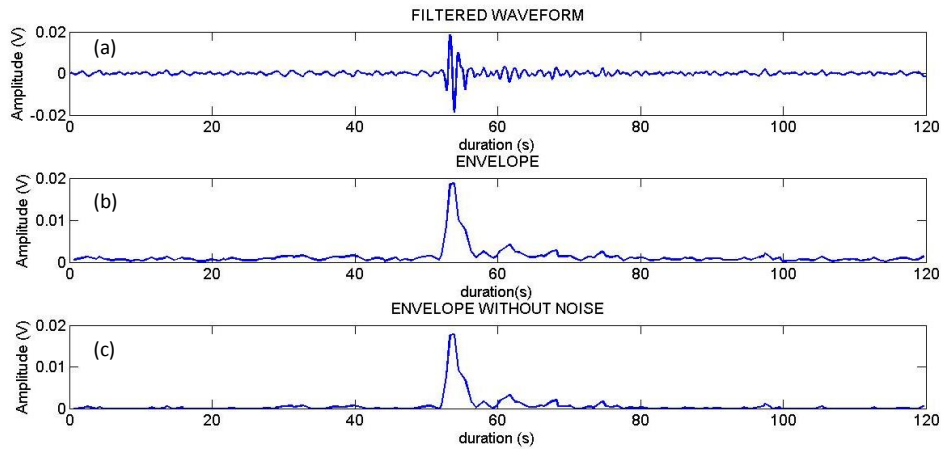


Figure 40 Waveform of an event filtered between 0.2 Hz and 1.2 Hz (a), envelope (b) and envelope corrected for the background noise contribution (c).

Once calculated the 'denoised envelope' we considered the duration obtained by a visual inspection of the waveform as well to calculate the integral. The obtained values are proportional to the energy of the events and are reported in the Figure 41 versus the time duration.

At this step of study, we decided to look at the results, showed in Figure 41 and following, obtained for the main impulses and these for the so called 'sub-impulses' separately (for a first explanation of the 'main' and 'sub' impulses see Figure 29, Figure 30, Figure 31 and Figure 32 in Section 6.1) (for a more accurately explanation of the main and sub impulses see Section 6.4.2), in order to eventually point out any different behaviour.

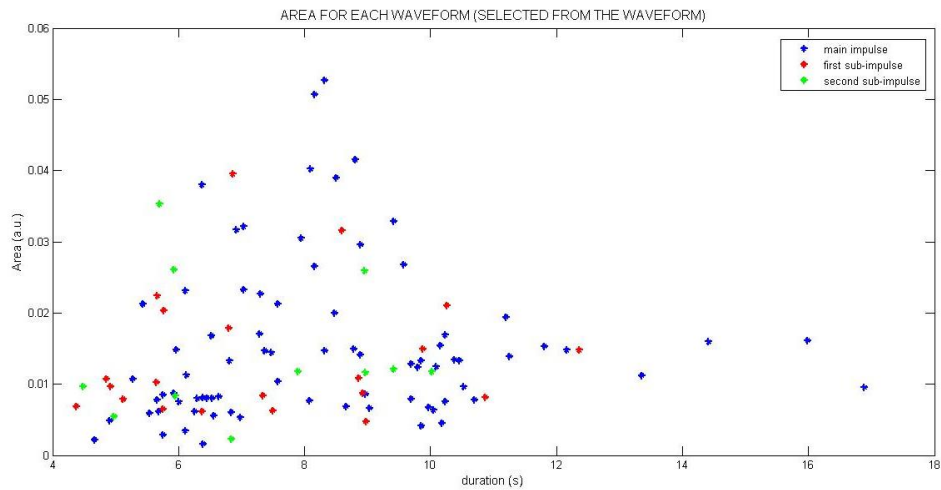


Figure 41 ‘Energy’ for each waveform versus duration of the event visually selected from the relative waveform. The blue symbols are relatives to the main impulse in the waveform, the red one to the first sub-impulse and the green to the second one.

We also calculated the ‘energy’ from the envelope as illustrated before, using a time window selected from the envelope itself, and the results are showed in Figure 42.

Also in this figure we separated the values relatives to the different impulses.

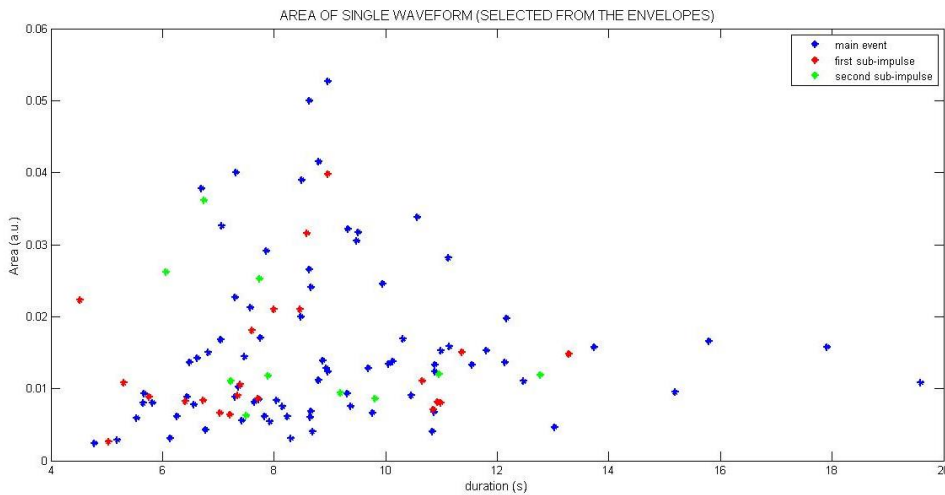


Figure 42 ‘Energy’ for each waveform versus duration of the event selected from the envelope. The blue symbols are relatives to the first impulse in the waveform, the red one to the second and the green to the third one.

We obtained similar results by selecting the time windows through a visual inspection of the waveforms or of the amplitude-envelope and, in both cases, a non-correlation between the two variables (‘energy’ and duration) is noticeable.

6.3.2.2 Envelope of the average of the horizontal components

Since the two horizontal components show a similar behaviour for the retrieved results, we decided to evaluate the average of the N-S and E-W components for each event and then apply to it the same procedure described in Section 6.3.2.1.

We used, again, two different approaches for the duration measurement: in the first we visually selected the onset of the impulse from the relative waveform and then we aligned the relative envelopes from that time to obtain their average. In the second, we aligned the envelopes using the onset selected from the two distinct envelopes. Then we calculated the ‘energy’ through the integral of the envelope in the selected time window, plotting the results in Figure 43 and Figure 44.

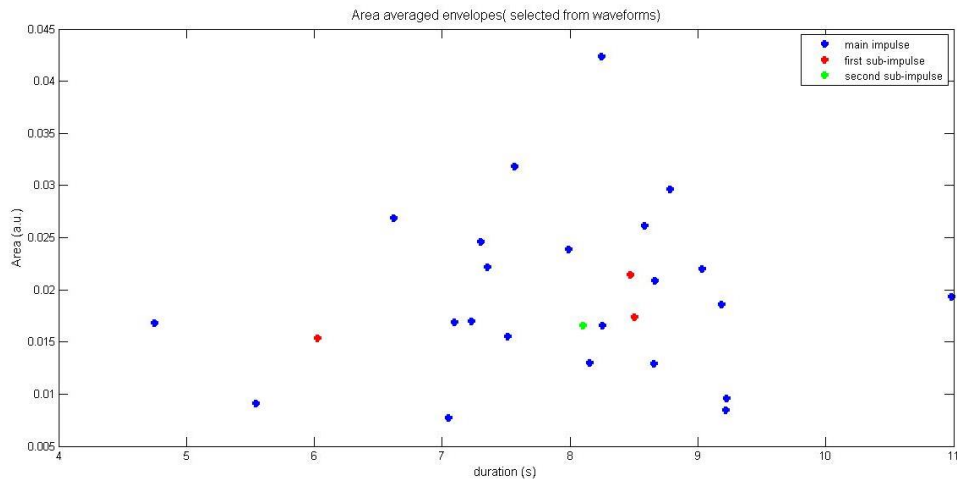


Figure 43 ‘Energy’ of the average of the horizontal components versus time duration selected from the waveforms for the ASB2 seismic station. The blue ones are relatives to the first impulse in the waveform, the red one to the second and the green to the third one.

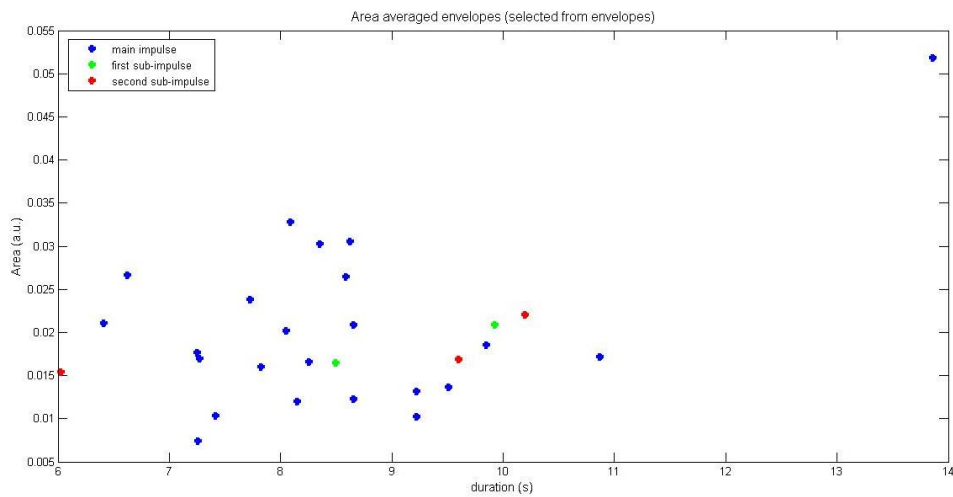


Figure 44 ‘Energy’ versus duration of the average of the horizontal components envelopes (calculated visually selecting the duration from envelopes) versus time duration selected from the envelopes for the ASB2 seismic station. The blue ones are relatives to the first impulse in the waveform, the red one to the second and the green to the third one.

Also in this case we represented the ‘energy’ of the results versus the duration of the “averaged component” to eventually point out any correlation.

The results are very similar for this two ways of selection of the envelope and an uncorrelation between the two variables in both cases is noticeable.

6.3.3 Conclusion of the first step of study

Using the different approaches described in this section we systematically obtained an uncorrelation between the energy and the duration of the LP events.

In fact, differently from a VT event, an LP characterized by a long (source) duration and a low maximum amplitude can have the same energy as another LP event with a greater maximum amplitude and a shorter duration, so the maximum amplitude alone is not sufficient to determine the magnitude of a Long Period event.

The above described methods point out some difficulties that suggested us to follow a different strategy to calculate the energy or a quantity proportional to it.

The duration selection is a difficult task mainly if we are analysing the average of the two horizontal components since the end of the impulse is often hidden by the noise. Moreover, in the time domain the duration value variation of few tenths of second results in different values of the variables associated with it, characterizing the final result for a poor stability.

For all the previous reasons and also to standardize the technique to other commonly used, we decided to move to the frequency domain and to analyze the waveforms according to the signal theory.

6.4 Waveforms analysis

Before describing the main procedure to evaluate the energy and then the magnitude of the LP events, we deeply studied the waveforms involved, in the time and in the frequency domain.

6.4.1 The spectrograms

In order to better characterize lots of the features of the low frequency seismicity analysed, we performed a spectral analysis using the spectrogram function.

A spectrogram is a way of representing the spectral content of a waveform, versus time.

The spectrograms were calculated using a sampling frequency of 125 Hz (typical of the instrumentation used), a 249 points window and an overlapping of 124 points. The spectrograms for the sample event recorded at four different seismic stations are reported in the following figures (Figure 45, Figure 46, Figure 47, Figure 48).

For each figure, the three components of the sample event recorded at a seismic station and their relative spectrograms are showed.

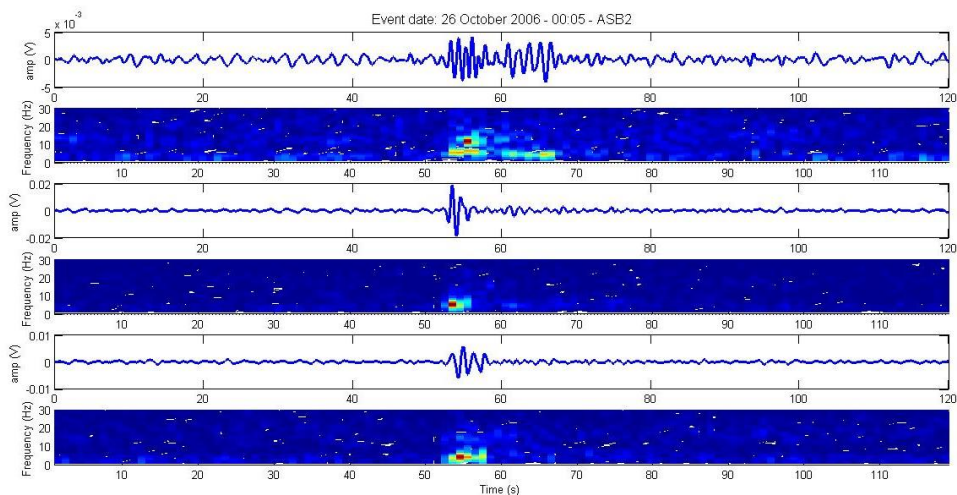


Figure 45 Waveform and relative spectrogram for the event of 26th of October 2006, at 00:05, recorded at the station ASB2 (sample event). The first waveform is the E-W component, the second the N-S component and the third the Z one.

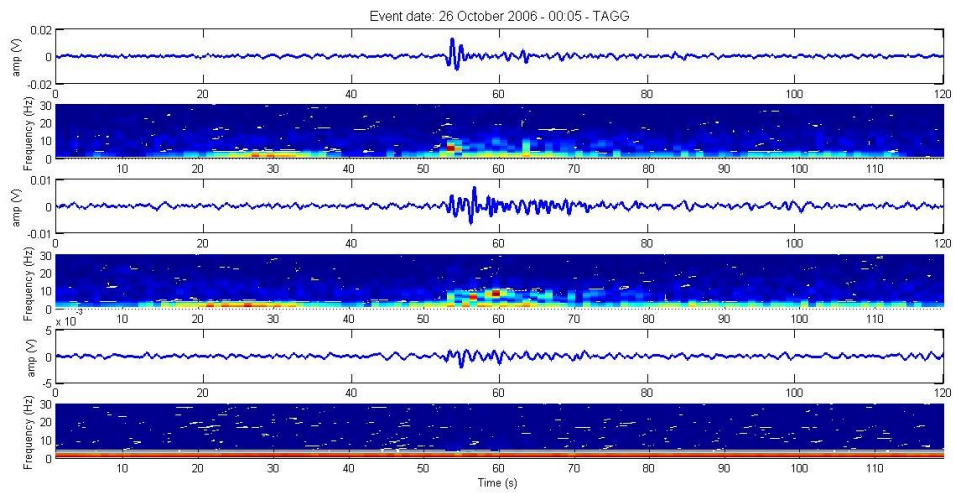


Figure 46 Waveform and relative spectrogram for the event of 26th of October 2006, at 00:05, recorded at the station TAGG. The first waveform is the E-W component, the second the N-S component and the third the Z one.

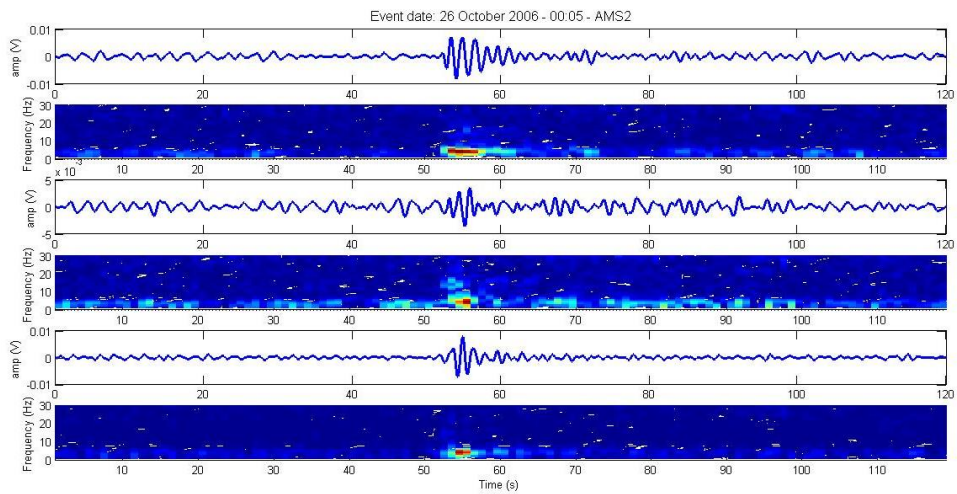


Figure 47 Waveform and relative spectrogram for the event of 26th of October 2006, at 00:05, recorded at the station AMS2. The first waveform is the E-W component, the second the N-S component and the third the Z one.

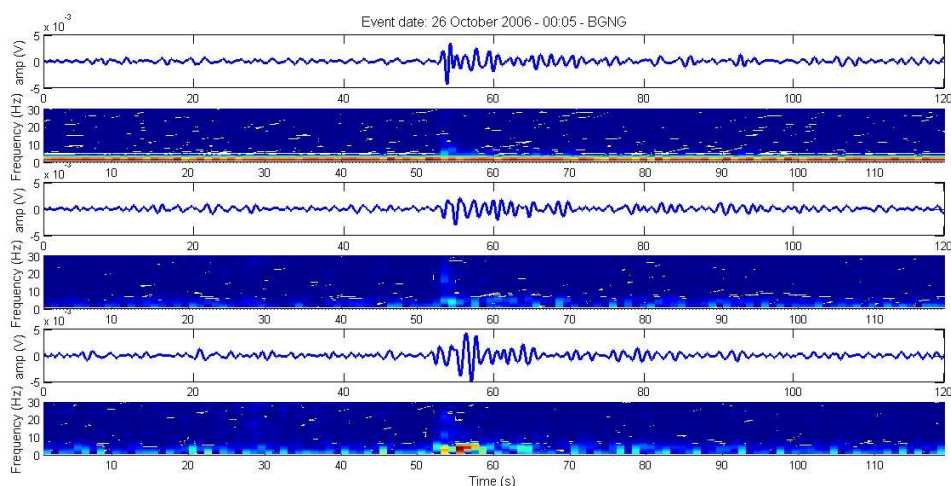


Figure 48 Waveform and relative spectrogram for the event of 26th of October 2006, at 00:05, recorded at the station BGNB. The first waveform is the E-W component, the second the N-S component and the third the Z one.

Spectrograms well enhanced the low frequency content and, in some cases (mainly for the Z component of the TAGG station and the E-W component of the BGNB station) showed also lower frequency content during the entire recording, possibly due to the background noise, as better detailed in Section 6.4.3.

In all the data set, as showed in Figure 45, Figure 46, Figure 47 and Figure 48, the peaks at low frequency are evident, more or less depending on the amplitude of the impulse and on the SNR.

Observing the spectrograms (for instance in Figure 45) we confirmed the presence of the so called sub-impulses described in Section 6.3.2.1. The presence of two temporally successive impulses can be seen also through the presence of different peaks in the spectrograms. These peaks are characterised by a low frequency content, typical of a LP event and may suggest that they represent two separate events although in immediately temporal succession. We observed this phenomenon in the entire dataset but only for a particular component of the waveforms of each seismic station. This feature will be better detailed studying the cross correlation of the waveforms, in the Section 0.

In some other spectrograms a contribution (in frequency) higher than that typical of the LP one is also evident for the entire (or almost the entire) recording; it reaches values up until about 20 Hz. We observed this, for instance, for the event of 26th of October at 9:12 at ASB2 and TAGG seismic stations (Figure 49 and Figure 50).

This may due to a noise contribute, but we will analyse it in detail in Sections 6.4.3 and Section 8.1.1.

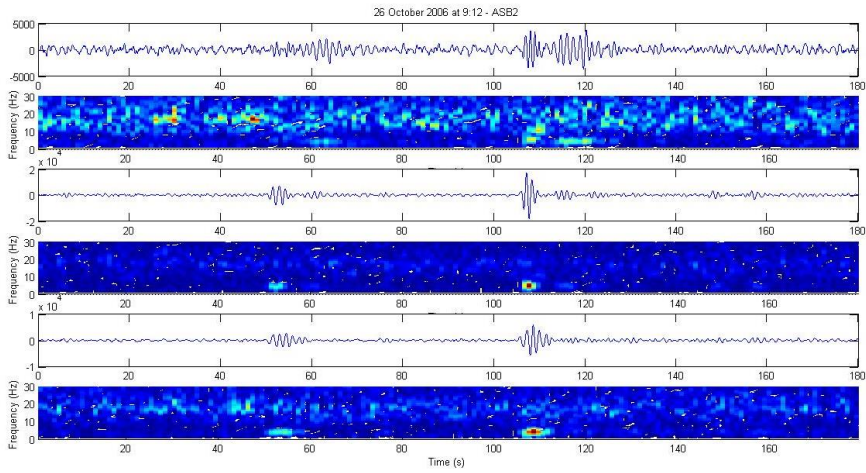


Figure 49 Waveform and relative spectrogram for the event of 26 of October at 9:12 at ASB2. The first waveform is the E-W component, the second the N-S component and the third the Z one.

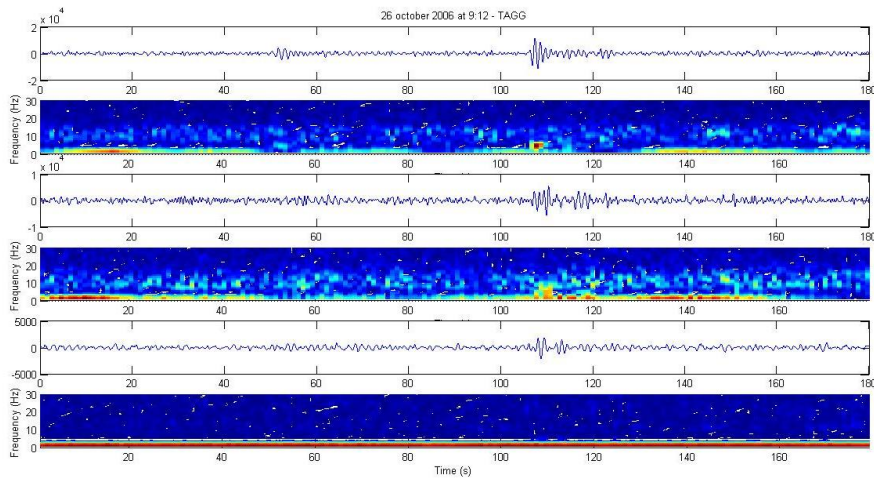


Figure 50 Waveform and relative spectrogram for the event of 26 of October at 9:12 at TAGG. The first waveform is the E-W component, the second the N-S component and the third the Z one.

6.4.2 Cross-correlation of the waveforms

A deeply study of the main-events and sub-events and their cross-correlation is not the purpose of this work, but, for sake of completeness as well as for a better comprehension of the waveforms features, we performed, also, this kind of study.

It is possible to compare a time series with itself at successive lags in order to detect dependencies through time, and it is also possible to compare two time series one to each other in order to determine the time position of pronounced correspondence. Two items of information may emerge from such a comparison: the strength of the relationship between the two series, and the lag or offset in time or distance between them at their position of maximum equivalence. The process of comparing two time series at successive lags is called **cross-correlation**. The *zero lag* often is set where the origins of the two series are aligned; negative or positive lags represent an arbitrary choice of the sense of movement of one sequence respect to the other. Since the two series are not identical, the cross-correlogram is not symmetric about its middle.

Waveform cross-correlation is an increasingly important tool for characterizing event similarity, improving earthquake locations, and studying source properties.

For continuous functions, $f(t)$ and $g(t)$, the cross-correlation is defined as:

$$C(t) \equiv \int_{-\infty}^{\infty} f^*(\tau) g(t + \tau) d\tau$$

Eq. 12

where $f(t)$ and $g(t)$ are time-dependent functions and f^* denotes the complex conjugate of f .

Similarly, for functions $f(m)$ and $g(m)$ of discrete variable m , the cross-correlation is defined as:

$$C(n) \equiv \sum_{m=-\infty}^{\infty} f^*(m) g(n + m)$$

Eq. 13

where n and m are integer numbers.

In an autocorrelation, which is the cross-correlation of a signal with itself, there will always be a peak at a lag of zero unless the signal is a trivial zero signal (Frasca, 2011).

We observed, in our data set, some sub-impulses after the main one (impulses temporally successive to the main one with amplitude almost-always gradually lower than the first). This phenomenon, visible only on one or two components of the seismograms, has been observed also for the LP seismicity recorded in other volcanoes in the world (see Matoza & Chouet, 2010, and references therein); an example is in Figure 51.

The observed feature may be addressed to several causes related to the source (source geometry or perturbation features) or to the path (attenuation or amplification effects) or also to site effects as well.

In order to investigate on the origin of these sub-impulses and their relation to the main events, we performed the cross-correlation between the typical LP impulses and sub-impulses, as detailed in the follow.

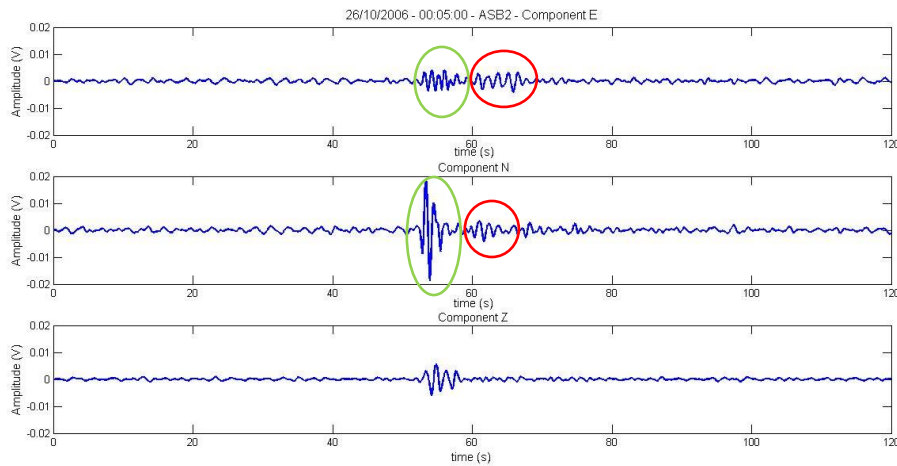


Figure 51 Three components waveform of the sample event. The 'sub-impulse' (red circle) after the main event (green circle) are visible in the N-S and E-W waveforms.

Waveforms recorded at all four stations (ASB2, TAGG, AMS2, BGNB) showing a 'main impulse' and a so-called 'sub-impulse' were analyzed.

We performed two different steps of cross-correlation, and, in both cases, we studied just a few fraction of seconds of the first arrival of the impulse, since they are related to the initial part of the source.

Firstly we evaluated the cross-correlation between the 'main event' and the 'sub-events' in a short time window (0.3 seconds), and then, if the retrieved normalized cross-correlation coefficient was larger than the fixed threshold of 0.8 (the cross correlation function were normalized to 1), then the 'main event' and the 'sub-event' were cross-correlated for a longer time window (1 second).

The ASB2 seismic station is the one with the higher number of sub-impulse probably because it is the one with the major SNR, so it was easier to observe small amplitude events.

For the seismograms recorded at the other seismic stations, sometimes, although the 'sub-events' presence was evident, it wasn't possible to determine them with a high degree of confidence, due to the noise level in which the sub-events are embedded. Therefore, to avoid inaccuracies, they were not taken into account in the analysis.

In the following figures (Figure 52 and Figure 53) an example of the result of the cross correlation analysis between the 'main impulse' and the 'sub-event' of the N-S component of Figure 51 is showed. There are the two steps of the analysis: in Figure 52 the cross-correlation with a time window of 0.3 s is showed and in Figure 53 the cross-correlation curve with a time window of 1 s in represented. In this case we performed both steps of cross-correlation (two type of time window) since in the first analysis the maximum of the curve exceeded than the 0.8 threshold.

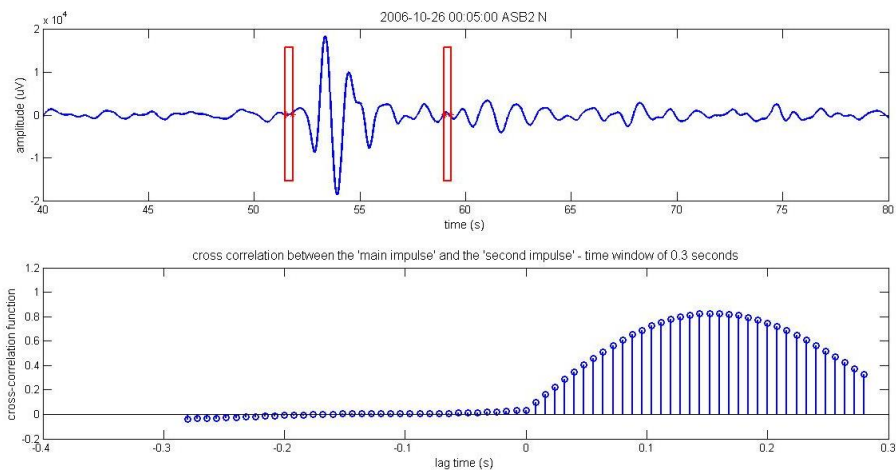


Figure 52 Waveform of the sample function and the cross-correlation curve between the 'main-impulse' and the 'second-impulse' with a time window of 0.3 s (in red rectangles the portion of waveforms cross-correlated).

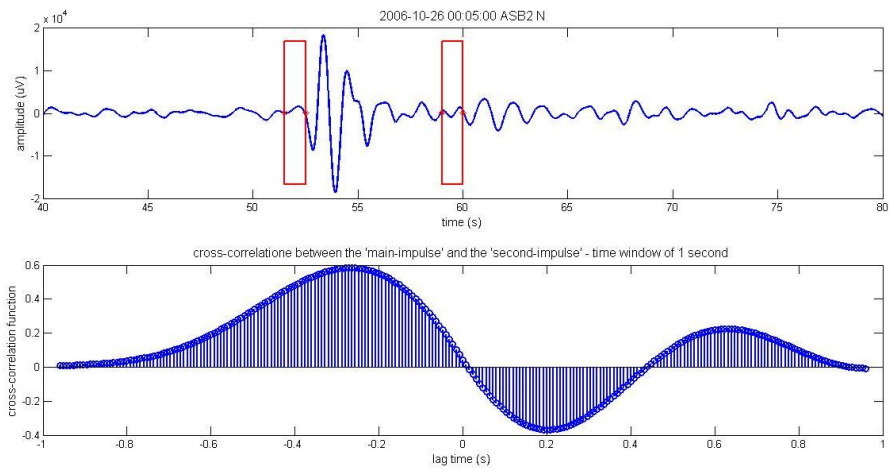


Figure 53 Waveform of the sample function and the cross-correlation curve between the ‘main-impulse’ and the ‘second-impulse’ with a time window of 1 s (in red rectangles the portion of waveforms cross-correlated).

Results for the entire data set are in Table 1 , where, for each seismic station, we reported the percentage of cross-correlation functions (calculated over the entire number of sub-impulses) that passed the two steps of analysis.

<i>Seismic station</i>	<i>% of CC with 0.3 s time window that pass the threshold</i>	<i>% of CC with 1 s time window that pass the threshold</i>
ASB2	62.3 %	38.1 %
TAGG	66.7 %	41.7 %
AMS2	80 %	70 %
BGNB	57.7 %	34.6 %

Table 1 Percentage (always calculated over the entire number of ‘sub-impulse’ for each seismic station) of the maximum of the cross-correlation functions that passed the threshold of 0.8. (The cross-correlation function is normalized)

A high percentage of sub-events passed the first step of cross-correlation, but it is not the same for the second time window cross-correlation.

Observing the results of both the cross-correlation and the spectral analysis and considering the very short spatial distances at which this events are recorded, we suggested that the presence of this kind of ‘sub-impulse’ just reflects some features of the shallow source that generated the seismicity.

For completeness, a better comprehension of this features need a more accurate study, but this beyond of our scope. So, to avoid any mistake, they will not be taken into account in the final step of data analysis.

6.4.3 Noise analysis

To better understand this kind of seismicity, we also studied the background noise.

In situation like those of the Campi Flegrei area, in which there is a very low SNR, the survey about the main features of the seismic noise is very important. In some spectrograms showed in the Section 6.4.1 we observed continuous peaks along the entire duration of the recording, at different frequencies. This is the main reason that motivated us in studying the seismic noise.

Observing, for example, the whole dataset recorded at ASB2 seismic station a difference between the three components should be noted. Each N-S component (of each event) is characterized, in fact, by a higher SNR than the other. In Figure 54 the waveforms of the sample event are shown, and is noticeable the different amplitude of the North-South component respect to the other ones. The cause of this difference may be due to some effect during the propagation of the wave through the halfspace (attenuation or amplification) even though this hypothesis may be unfavoured by the shallow depth at which these events originated (about 500 m) . Another hypothesis is that the observed feature may be due to a source property like the orientation of the cracks that originates this LP events .

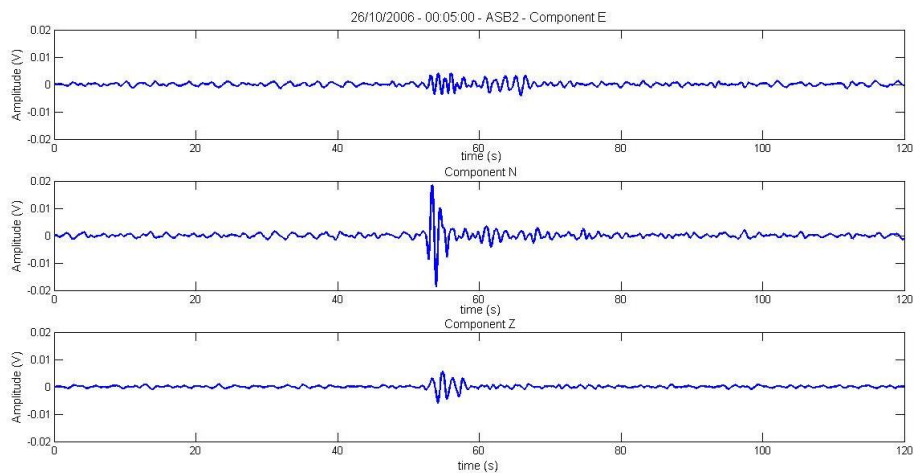


Figure 54 Waveform of the event of October 26th 2006 at 00:05 recorded at ASB2 seismic station.

In order to define the main features of the seismic noise in the investigated area, an analysis of the noise amplitude recorded at the station ASB2 is developed. So, for each recorded event, 10 seconds of seismic noise amplitude (absolute value) are averaged and then reported into a plot to compare the three component of each event (Figure 55).

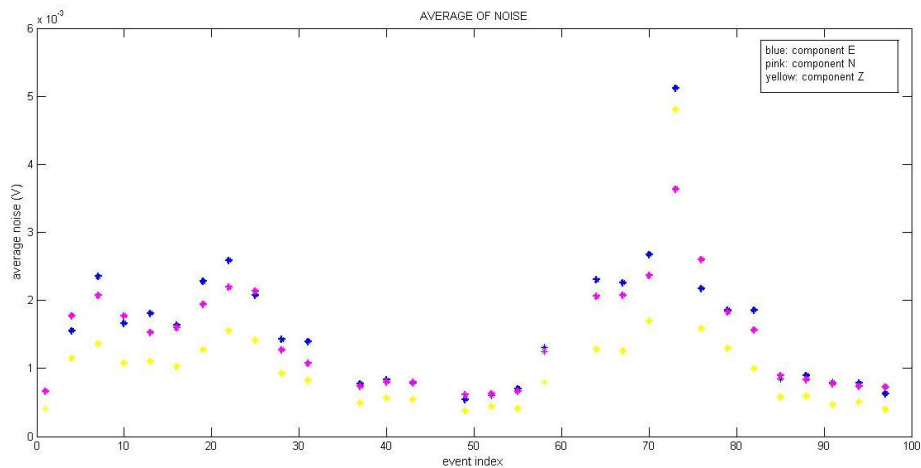


Figure 55 Average of 10 s of seismic noise (absolute value) for the three components before every events recorded at the ASB2 seismic station. each integer number (event index) in the x-axes represents an event. In blue is the component E-W, in pink the N-S and in yellow the Z component.

Observing Figure 55 it can be noted that the vertical component is always characterized by a low noise amplitude than the other components. These latter have a similar amplitude of the noise, and in particular 10 of those 30 have a noise with amplitude greater in the component N and 19 of those in the component E (just for one event the amplitude of the two component is the same).

This should allow us to exclude a phenomenon of amplification along the NS direction otherwise also the noise amplitude along that direction should be greater than in the others two.

The noise can be studied also in the frequency domain. The different contribute of the noise were showed during the analysis of the spectrograms (Section 6.4.1), where some different frequency contributes were noticed, at low and high frequency.

It is well known that the seismic noise can be due to different causes and consequently it occurs in different frequency bands (Del Pezzo, *et al.*, 2013 and *referencies therein*).

The mainly causes are:

- marine background: (0.1 – 2) Hz (Bianco *et al.*, 2010);
- weather conditions: low frequency, in particular (0.05 – 1) Hz (Marzorati, 2004) (Bianco, *et al.*, 2010);
- proximity the coast line: (0.1 – 1) Hz (Bianco, *et al.*, 2010);
- anthropic: (1 -5) Hz (Marzorati, 2004) (Bianco, *et al.*, 2010) ;
- water streams, volcanic activity, fluid circulation and the wind interaction with vegetation and topography: high frequency contribute (Bianco, *et al.*, 2010).

Considering the results of the spectral analysis too (Section 6.4.1) and considering that the area of the seismic sources (around the Solfatara crater) is near the sea, we are convinced that the contribution at very low frequency may be due to the marine background and to the proximity to the coastal line.

For this reason the BGNB seismic station, that is the nearest to the coast line, is the one with the lower SNR.

The contribution to the high frequency (also (10-20) Hz), found in the spectrograms analysis, may be ascribed, on the contrary, to the fluid circulation, particularly active in the considered area, in addition, obviously, to the anthropic contribution (the Campi Flegrei caldera is a densely populated area).

To verify the different contribution to the frequency content of these events, a section dedicated to the spectra calculation will be developed later (8.1.1).

7. The energy and magnitude estimation method

Parts of the following paragraphs have been taken from the article published in Geophysical Journal International in 2013. My coauthors are E. Del Pezzo and F. Bianco. I conducted part of the theoretical work and part of the writing.

In order to study the energy of the LP events we decided to use the standard signal theory. We moved in the frequency domain and calculated the energy through the velocity-density spectrum.

The first step was the definition of a simple method to determine the time duration of the LP events. Then we approached the problem of linking the retrieved energy values to Magnitude values by quantitatively, comparing a VT and an LP spectra, finally defining the relationship that allowed us to obtain the LP magnitude-scale.

In the following, the entire procedure is explained in detail.

7.1 Signal theory

For a finite energy signal, the normalized energy can be calculated integrating the square of the modulus of the signal in the time domain or in the frequency domain (*Parseval theorem*):

$$E = \int_{-\infty}^{\infty} |x(t)|^2 dt = \int_{-\infty}^{\infty} |X(f)|^2 df$$

Eq. 14

where $x(t)$ is the waveform in the time domain, t is the time variable, $X(f)$ is the signal in the frequency domain (Fourier Transform) and f is the frequency. In the frequency domain, the total energy of the signal $x(t)$, in the frequency band (f_1, f_2) is evaluated using the following equation (Eq. 15) (Liberali, 2010):

$$E = \int_{f_1}^{f_2} |X(f)|^2 df$$

Eq. 15

To evaluate the ‘energy’ we don’t need to have a displacement signal, since, whatever is the physical quantity that describes the ground motion, for a monochromatic wave, the energy will always be proportional to the square of the amplitude of the considered physical quantity (Zollo *et al.*, 2003). In fact, if we use the Eq. 7 considering that $2\pi/T_0 = \omega_0$ we can write:

$$x = a_0 \cos(\omega_0 t)$$

Eq. 16

where a_0 is the maximum amplitude of the wave and t the time variable. Consequently, the velocity, that is the time derivative of the displacement, will be:

$$v = \frac{\partial x}{\partial t} = -a_0 \omega_0 \cdot \sin(\omega_0 t)$$

Eq. 17

and:

$$v^2 = a_0^2 \cdot \omega_0^2 \cdot \sin^2(\omega_0 t)$$

Eq. 18

The energy is proportional to the square of the maximum of the velocity, and we can write:

$$E \propto v^2 \propto a_0^2 \omega_0^2$$

Eq. 19

So we can deduce that the energy is proportional also to the velocity of the ground displacement.

Considerations allows us to use the velocity waveforms of our data-set.

7.2 The duration

The first task is to determine the duration of the LP source, since it plays an important role in the determination of the ‘energy’. In the Section 6.2, we described different ways to evaluate the duration of the LP events, but in this case we decided to adopt a universal method that doesn’t need a visual evaluation. It is based on the “shape” of the waveform and the exponential decay of its tail, and it may be very useful in the routinely monitoring activities of a volcanological observatory.

We simplified the source model assuming a single square crack source with two dimensions $L=W$ and $d \ll L$ (see Figure 7) (Del Pezzo *et al.*, 2013, Ferrazzini & Aki, 1992). So, in the spectrum of the LP events, the peaks

distribution reflects that of the normal modes of vibration of that crack and the eigenfrequencies are given by:

$$f = \frac{c}{2} \sqrt{\left(\frac{n_x}{W}\right)^2 + \left(\frac{n_y}{L}\right)^2 + \left(\frac{n_z}{d}\right)^2}$$

Eq. 20

where n_x , n_y and n_z are integers greater than zero and c is the velocity of the sound in the fluid which permeates the crack (Morse & Bolt, 1944, Ferrazzini & Aki, 1992).

The dominant peak of the spectrum is associated to the normal mode of vibration, i.e. $n_x=1$, $n_y=0$ and $n_z=0$. If we substitute those values in Eq. 20, we obtain:

$$f_0 = \frac{c}{2L}$$

Eq. 21

where f_0 is the dominant frequency and L is the crack dimension.

Measuring the width at half of the maximum amplitude of the spectral peak (Δf) we can get the duration of the LP event, since, the width is correlated to the quality factor of the resonator Q (completely different from the quality factor of the earth medium, see Section 3.1) (Elmore & Heald, 1969, Nakano, *et al.*, 2007). In fact:

$$\Delta f = \frac{f_0}{Q}$$

Eq. 22

so

$$Q = \frac{f_0}{\Delta f} = 2\pi f_0 \tau$$

Eq. 23

where τ is the time at which the waveform has squared amplitude equals to $1/e$ of the maximum squared amplitude. So, hereafter, we assumed that a 'reasonable' estimation of the LP duration is 2τ .

In order to obtain the time duration, we decided to proceed in the following way:

we calculated the waveform envelope based on the Hilbert transform (in particular, evaluating the absolute value of the Hilbert transform). After that, we selected the LP arrival time using the onset of the vertical component previously evaluated (Section 6.2.1) and then, we calculated the maximum of each squared envelope (A_{max}). The time at which the squared envelope

amplitude is equal to A_{max}/e (starting from the onset) is taken as the τ value. So we can determine the duration as 2τ . We decided to use, for each event, the minimum duration of the three component values. An example of the three components of an LP event (the sample event) and the selection of the onset and the 2τ duration (red lines) is showed in the following figure (Figure 56):

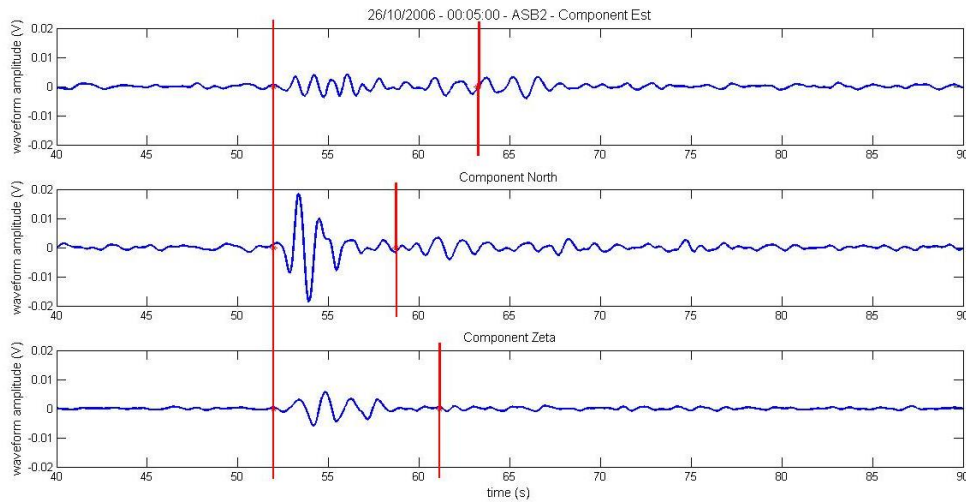


Figure 56 Sample event of the October 26th 2006 at ASB2 seismic station. The red lines show the onset of the seismic impulse and the end of the three different components using the ' 2τ ' method. The final time duration is the smallest of the three.

7.3 Spectral analysis – the energy evaluation

Once selected the time window, in order to obtain the signal in the frequency domain we applied the Fourier Transform to that one (using the FFT algorithm of Matlab programming language).

The Fourier Transform FFT in Matlab is not, however, corrected by any normalization coefficient. We decided to evaluate the right coefficient to be able to compare these value with the values evaluated for other events, and, in case, using different Fourier transform routines. So, first of all, we correctly estimated the normalization factor to be able to get the right spectrum. The retrieved normalization factor is:

$$K_{norm} = \frac{1}{f_s \cdot \sqrt{2\pi}}$$

Eq. 24

The final expression for the discrete FFT function is then:

$$X_k(f) = \mathcal{F}_d(x_j) = \frac{1}{f_s \cdot \sqrt{2\pi}} \sum_{j=0}^{N-1} x_j e^{-i \frac{2\pi}{N} k j}$$

Eq. 25

where: f_s is the sampling frequency of the instruments (125 Hz), x_j is the waveform and N the number of points. We also used a sampling window, the Hanning window, in the transform calculation.

We took into account some effects that concur in defining the correction coefficient of the spectra, that take into account the transduction constant of the instrument (G) and the path-dependent attenuation (Petrosino *et al.*, 2008).

We used the following formula Eq. 26:

$$C_{corr} = G \cdot \exp\left\{\frac{-\pi t f}{Q}\right\} = G \cdot \exp\left\{\frac{-\pi r f}{v_s Q}\right\} = G \cdot \exp\left\{\frac{-\pi r f^{1-g}}{v_s Q_0}\right\}$$

Eq. 26

where f is the frequency, r is the distance between the source and the seismic station (in meters), v_s is the S-wave velocity of the sound in the earth medium and Q is the total quality factor averaged in the earth volume under investigation, and is equal to $Q_0 f^g$ (Petrosino *et al.*, 2008).

Using the Eq. 15, we calculated the integral of the average of the modulus of the squared spectra for each component, as in Eq. 27 and Eq. 28:

$$E = \int_{f_1}^{f_2} X_a^2(f) df$$

Eq. 27

where

$$X_a^2(f) = C_{corr}^2 \cdot \frac{1}{3} \cdot (|X_{kN}^2| + |X_{kE}^2| + |X_{kZ}^2|)$$

Eq. 28

where X_{kN}^2 , X_{kE}^2 , X_{kZ}^2 are the squared velocity density spectra, relative to the three components, obtained using the Eq. 25.

To define f_1 and f_2 values, in Eq. 27, we considered that f_1 should be a lot lower than the peak frequency of the event and f_2 should be greater than f_c , where f_c is the cut-off frequency of the instruments. Since the contribution to

the total energy from the high-frequency ($>f_c$) components strongly decreases with frequency, the numerical value of f_2 is not crucial for the following calculations, hence we fixed this value at 25 Hz, i.e. the typical value below which most seismic instruments show a flat velocity response. Accordingly, we also used $f_1=0$ Hz.

7.4 The Magnitude estimation method

The developed procedure is based on the comparison between the energy of LP and VT signal, estimated as the integral of the squared velocity spectra, on the reasonable assumption that the stress drop of the area under investigation is constant. So, the LP magnitude is defined as the moment magnitude of the VT event that has the same energy of the LP event.

The relationship between the energy and the moment is (Kostrov, 1974):

$$E = \frac{\Delta\sigma}{2\mu} M_0$$

Eq. 29

where $\Delta\sigma$ is the stress-drop and μ is the shear modulus (we considered $\Delta\sigma=10^6$ Pa and $\mu= 5\cdot 10^{10}$ Pa, that are typical values for volcanic rocks (Del Pezzo, *et al.*, 1987)). We can also write, in S.I. units:

$$M_w = \frac{\log_{10}\left(\frac{E}{E_{ref}}\right) - 11.8}{1.5} = \frac{\log_{10}\left(\frac{M_0}{M_{ref}}\right) - 11.8}{1.5} = \frac{2}{3} \log_{10}M_0 - 6.53$$

Eq. 30

where $E_{ref} = 10^{-7}$ N*m accounts for the dyne*cm to N*m conversion and M_{ref} is the moment correspondent to E_{ref} .

The moment magnitude scale, as it is related to some physical properties of the seismic source, is calculated through the seismic spectra corrected for the propagation effects between the source and the receiver.

As first step we theoretically derived the integral that compares in Eq. 27 for a VT event and its relationship with the magnitude M_{VT} .

For simplicity we'll call $S_{VT}(r, M_{VT})$ the integral that appears in the Eq. 27 for a VT event and $S_{LP}(r, M_{LP})$ the one for an LP event.

In order to obtain the magnitude M_{LP} , i.e. the magnitude associated to LP, we first evaluated S_{LP} and then we searched for the S_{VT} equal to S_{LP} ; the related M_{VT} is taken as the estimate of M_{LP} .

For the considerations in Section 7.1, we could write:

$$S_{VT}(r, M_{VT}) = \int_{f_1}^{f_2} X^2(M_{VT}, f, r) \propto E_{VT}(r, M_{VT})$$

Eq. 31

and

$$S_{LP}(r, M_{LP}) = \int_{f_1}^{f_2} X_{LP}^2(M_{LP}, f, r) \propto E_{LP}(r, M_{LP})$$

Eq. 32

We assumed that most of the VT seismic energy is associated with the S-wave, so the velocity density spectrum for an S wave at distance r can be written as (Eq. 33) (Brune, 1970, Boatwright, 1980):

$$X(f, r) = \frac{2\pi f}{\sqrt{1 + \left(\frac{f}{f_c}\right)^{2\gamma}}} \frac{1}{4\pi\rho} \frac{1}{\beta^3} \frac{1}{r} Y M_0$$

Eq. 33

where ρ is the earth density, β is the shear wave velocity, $\gamma=2$, Y is the radiation pattern function modulus (averaged over azimuth) and f_c the corner-frequency given by:

$$f_c = \frac{\beta_r}{\pi} \frac{1}{\left(C \frac{M_0}{\Delta\sigma}\right)^{1/3}}$$

Eq. 34

where β_r is the rupture speed, $\Delta\sigma$ the stress-drop and C a constant associated with the source geometry which is analytically calculated for a few specific geometry. In this case we assumed a circular fault geometry (although the other geometries affect the X evaluation by less then 7%), so the C is equal to 7/16 (e.g. Lay & Wallace, 1995).

We assumed that this model hold well for a VT event (Del Pezzo, *et al.*, 1987). So, considering Eq. 33, Eq. 34 and Eq. 30, we could obtain S_{VT} from the following equation (Eq. 35):

$$S_{VT}(r, M_{VT}, \Delta\sigma) = \frac{1}{4\pi\rho} \frac{1}{\beta^3} \frac{M_0(M_w)}{r} Y \int_{f_{min}}^{f_{max}} \frac{2\pi f}{\sqrt{1 + \left(\frac{f}{\frac{\beta_r}{\pi} \frac{1}{\left(C \frac{M_0}{\Delta\sigma}\right)^{1/3}}} \right)^2}} df$$

Eq. 35

rewriting the Eq. 30 in the form:

$$M_0(M_w) = U a_1 \exp(a_2 M_w)$$

Eq. 36

where $a_1 = 1.1092$, $a_2 = 3.4539$ and $U = 10^9$.

Expliciting M_w , Eq. 35 may be written as (Eq. 37):

$$S_{VT}(M_w, r, \Delta\sigma) = A_1(M_w, r, \Delta\sigma) \cdot [F_1(M_w, r, \Delta\sigma) + F_2(M_w, r, \Delta\sigma) + F_3(M_w, r, \Delta\sigma) + F_4(M_w, r, \Delta\sigma) + F_5(M_w, r, \Delta\sigma) + F_6(M_w, r, \Delta\sigma)]$$

Eq. 37

with:

$$A_1(M_w, r, \Delta\sigma) = \frac{1}{16\sqrt{2}Cr^2\beta^6\pi^3\rho} U Y a_1^2 e^{a_2 M_w} \beta_r^3 \Delta\sigma$$

Eq. 38

$$F_1(M_w, r, \Delta\sigma) = 2 \text{ArcTan} \left(1 - \frac{\sqrt{2}\pi f_{min} \left(\frac{U a_1 C e^{a_2 M_w}}{\Delta\sigma} \right)^{1/3}}{\beta_r} \right)$$

Eq. 39

$$F_2(M_w, r, \Delta\sigma) = -2 \text{ArcTan} \left(1 + \frac{\sqrt{2}\pi f_{min} \left(\frac{U a_1 C e^{a_2 M_w}}{\Delta\sigma} \right)^{1/3}}{\beta_r} \right)$$

Eq. 40

$$F_3(M_w, r, \Delta\sigma) = -2\text{ArcTan} \left(1 - \frac{\sqrt{2}\pi f_{sup} \left(\frac{Ua_1 C e^{a_2 M_w}}{\Delta\sigma} \right)^{1/3}}{\beta_r} \right)$$

Eq. 41

$$F_4(M_w, r, \Delta\sigma) = 2\text{ArcTan} \left(1 + \frac{\sqrt{2}\pi f_{sup} \left(\frac{Ua_1 C e^{a_2 M_w}}{\Delta\sigma} \right)^{1/3}}{\beta_r} \right)$$

Eq. 42

$$F_5(M_w, r, \Delta\sigma) = -\text{Log} \left(\frac{\frac{\beta_r^2}{\pi^2} \left(\frac{Ua_1 C e^{a_2 M_w}}{\Delta\sigma} \right)^{2/3} - \sqrt{2} f_{min} \frac{\beta_r}{\pi} \left(\frac{Ua_1 C e^{a_2 M_w}}{\Delta\sigma} \right)^{1/3} + f_{min}^2}{\frac{\beta_r^2}{\pi^2} \left(\frac{Ua_1 C e^{a_2 M_w}}{\Delta\sigma} \right)^{2/3} + \sqrt{2} f_{min} \frac{\beta_r}{\pi} \left(\frac{Ua_1 C e^{a_2 M_w}}{\Delta\sigma} \right)^{1/3} + f_{min}^2} \right)$$

Eq. 43

$$F_6(M_w, r, \Delta\sigma) = \text{Log} \left(\frac{\frac{\beta_r^2}{\pi^2} \left(\frac{Ua_1 C e^{a_2 M_w}}{\Delta\sigma} \right)^{2/3} - \sqrt{2} f_{sup} \frac{\beta_r}{\pi} \left(\frac{Ua_1 C e^{a_2 M_w}}{\Delta\sigma} \right)^{1/3} + f_{sup}^2}{\frac{\beta_r^2}{\pi^2} \left(\frac{Ua_1 C e^{a_2 M_w}}{\Delta\sigma} \right)^{2/3} + \sqrt{2} f_{sup} \frac{\beta_r}{\pi} \left(\frac{Ua_1 C e^{a_2 M_w}}{\Delta\sigma} \right)^{1/3} + f_{sup}^2} \right)$$

Eq. 44

Solving analytically Eq. 37 is very complicated; since we were interested in developing an application that may be efficiently used in quasi real-time for the Observatories routine and/or emergencies activities, we approached the solution through numerical approximations, as discussed in the following. For a set of distances r we theoretically estimated S_{VT} (using the Eq. 37) and plotted versus M_{VT} , in Figure 57.

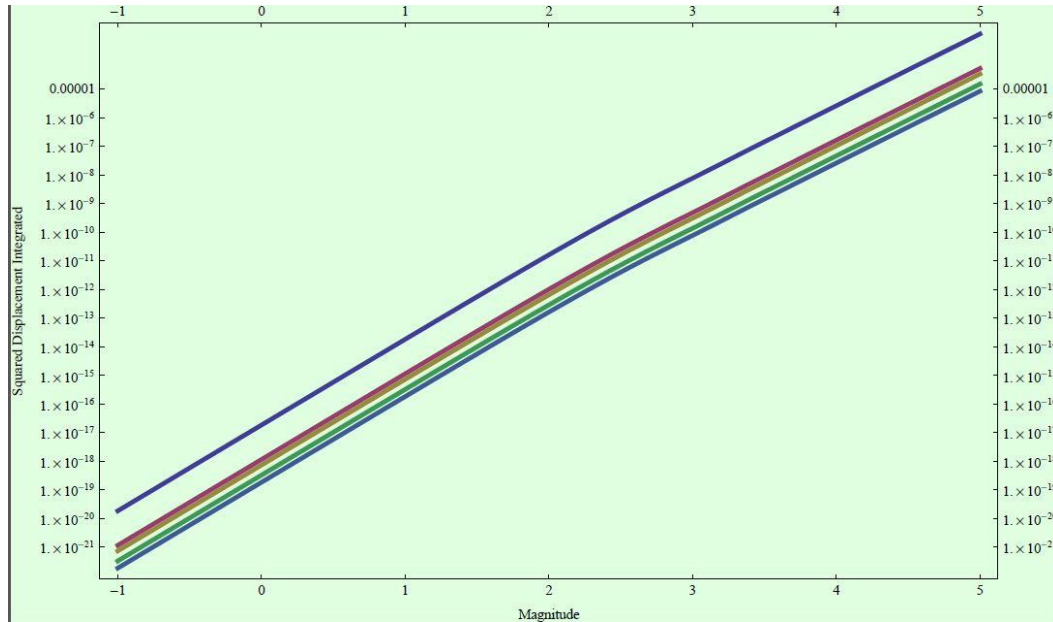


Figure 57 Squared velocity density spectrum integrated between 0 and $f_{sup} = 50$ Hz versus magnitude for different distances: 1000 m (blue), 4000 m (red), 5000 m (brown), 7500 m (green), 10000 m (blue) (Del Pezzo *et al.*, 2013).

So, to graphically obtain the M_{LP} value we can just follow the line in the plot corresponding to the evaluated S_{LP} for a corresponding distance, like a nomogram.

To analytically obtain the M_{LP} value, in automatic way (very important for the surveillance work of a Volcanological Observatory) we searched for a numerical formula that would link the considered variables (S_{VT} , M_{VT} and r).

Observing Figure 57 we could deduce that the curves that represent different source-receiver distances are parallel. In other words, the effects of changing the distance results in a shift of the S_{VT} - M_{VT} curve upward or downward in the plot.

A set of second-degree polynomials, with each polynomial with the zero-degree term that depends on distance, is thus a good candidate to represent the curves in Figure 57. For this reason we could write (Eq. 45):

$$\text{Log}_{10}(S_{VT}) = aM^2 + bM + c(r)$$

Eq. 45

where $c(r)$ is a function of distance with characteristics to be determined. To perform this last task we proceeded in the following steps:

- we selected a wide set of distance values, sampled in an interval between 1000 m and 20 000 m, characteristic of the distance range in which LP are generally observed. For the i th value of this set, r_i , we found the best fit (least squares) estimate for the parameter vector

$m_i = \{a_i, b_i, c_i\}$ of Eq. 45 that is, the i th element of the polynomial set.

- we observed from the results of this fit that only the c_i elements of the vectors m_i were different at the different values of i , as is also implicitly shown by the parallelism between the curves in Figure 57. Due to this evidence, we could drop out the index i in a and b , to obtain $m_i = \{a, b, c_i\}$. The obtained values for a and b are:

$$a = 3.05 \quad \text{and} \quad b = -0.2$$

- we plotted c_i versus distance r_i as shown in Figure 58. The best-fit curve which interpolates the couples $\{c_i, r_i\}$ is a quarter-order polynomial (Figure 58, blue line) of the form

$$c(r) = p_0 + p_1 r + p_2 r^2 + p_3 r^3 + p_4 r^4$$

Eq. 46

The values obtained for the p_i parameters are in the following Table 2:

p_0	p_1	p_2	p_3	p_4
-10.63	-0.00065	6.86×10^8	-3.57×10^{-12}	6.89×10^{-17}

Table 2 Values of the p parameters of the interpolation of the coefficient $c(r)$ with a 4th degree polynomial.

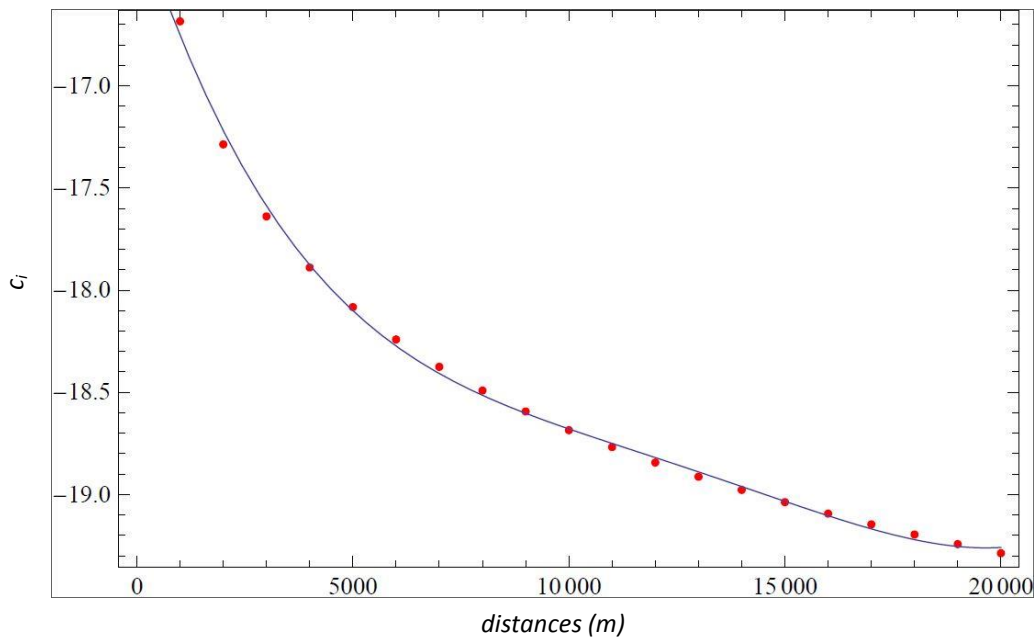


Figure 58 Plot of the parameter c_i versus distances in meters (red dots). The blue line represent the interpolation with the 4th order polynomial.

So, we substituted the value of $C(r)$ (Eq. 46) in the Eq. 45 and we obtained:

$$\text{Log}_{10}(S_{VT}) = aM^2 + bM + p_0 + p_1r + p_2r^2 + p_3r^3 + p_4r^4$$

Eq. 47

so we could write:

$$aM^2 + bM + p_0 + p_1r + p_2r^2 + p_3r^3 + p_4r^4 - \text{Log}_{10}(S_{VT}) = 0$$

Eq. 48

and for simplicity we wrote the Eq. 48 in the form of (Eq. 49):

$$aM^2 + bM + C(r) = 0$$

Eq. 49

where $C(r) = p_0 + p_1r + p_2r^2 + p_3r^3 + p_4r^4 - \text{Log}_{10}(S_{VT})$

Eq. 50

Finally, we plotted (Figure 59) the values of $\log_{10}(S_{VT})$, analytically determined using the Eq. 35 (lines), versus magnitude, superimposed to the interpolated curve obtained from Eq. 47 (dots, rhombs and stars).

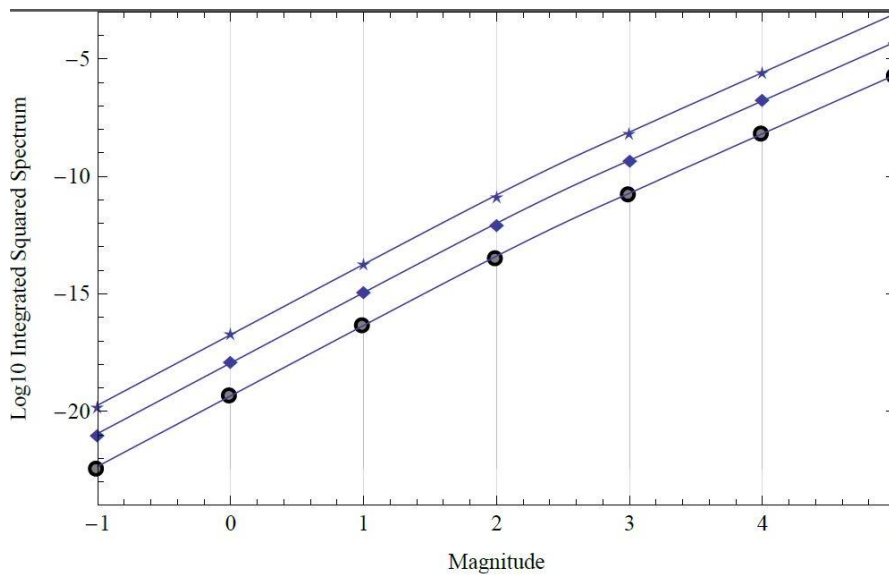


Figure 59 Values of $\text{Log}_{10}(S_{VT})$ versus magnitude theoretically calculated (lines) and interpolated using Eq. 47 (dots for a distance of 20 000 m, rhombs for 4000 m and stars for 1000 m).

To obtain the Magnitude (M_{LP}) for an LP event we could solve the Eq. 49 and take into account only the solution that led an increasing of magnitude with distance. Finally, the formula used for the estimate of the magnitude M_{LP} is (Eq. 51):

$$M_{LP}(r) = \frac{-b + \sqrt{b^2 - 4aC(r)}}{2a}$$

Eq. 51

with $C(r)$ from Eq. 50, substituting S_{VT} by S_{LP} calculated from the data and previously corrected for both instrumental response and attenuation (Eq. 28).

7.4.1 The error estimation

A value of the error is obviously correlated to the magnitude estimation. To evaluate this, we proceeded using a Monte-Carlo approach, considering that this error reflects essentially the uncertainty on the estimation of $C(r)$ parameter (that depends on the uncertainty of the spectral estimate and hence on the SNR of the signals) and of the hypocentral distance r .

First, we estimated the dependence of the spectral estimate on the SNR. To do this, we took a square wave 2 s long in the time domain. Gaussian noise with a Root-Mean-Square of up to 70% of the signal amplitude was added to this synthetic signal, to obtain sets of synthetic signals with increasing SNRs. For each value of SNR, we generated 1000 signals. For any value of the SNR, we thus calculated the squared spectra integral between the same frequency limits used in the present study (Section 7.3) to calculate the integrals of Eq. 32 for all the signals belonging to the same set, and eventually its average and standard deviation, which represent the error on the squared spectra of the signal. This error is never >2% for a SNR of 70%, which is an overestimation of the true SNR even for bad quality data. Changing the duration of the square wave does not affect significantly the error estimate, and thus we were confident that an overestimation of the error on the squared spectra integral is less than 2% of the value. We finally applied a Monte-Carlo procedure to estimate the errors on M_{LP} . Taking into account an error of 2% in the integral of the squared velocity spectrum, and an uncertainty in the determination of the hypocentral distance of the order of 30%, for each value of the integral we generated a random set of 10 000 values with an average equal to $C(r)$ and a standard deviation of 2% of this value, and a random set of distances with an average equal to the measured distance and a standard deviation of 30% of this value. Finally, we calculated the magnitude for any pair of squared velocity integrals and distances sampled in these two sets. The standard deviation of the magnitudes thus obtained from Eq. 51 represents a Monte-Carlo estimate of the error associated with the LP magnitude so far. All the errors obtained from some examples of the application are between 0.15 and 0.2, so to be sure to not underestimate the error, we considered an error value of 0.2.

8. Data analysis - application of the method

The obtained method for the magnitude calculation was applied to LP seismic events belonging to different volcanoes.

First of all we applied the method to the Campi Flegrei LP seismicity recorded on October 2006 and deeply studied in this doctoral thesis.

As second step we decided to apply the method to a data-set relative to LP events recorded on Colima volcano (Mexico) in 2005 and then we used the algorithm also to obtain the magnitude value of an event recorded on Etna volcano (Sicily, South Italy).

8.1 Campi Flegrei

8.1.1 The dominant frequency

Basing on the Fourier Transform (calculated considering the '2 τ ' time window of each waveform (see Section 7.2)) and using the Eq. 25, we calculated the spectrum of each event at each seismic station, averaging the three spectra X_i and correcting it with the C_{corr} coefficient in Eq. 26, obtaining:

$$\overline{X}_k = \frac{1}{3} C_{corr} (|X_{kN}| + |X_{kE}| + |X_{kZ}|)$$

Eq. 52

To compute the correction coefficient in the Eq. 26 we used $G= 800$ Vs/m, $v_s= 2700$ m/s, $Q_0=21$ and $g= 0.6\pm 0.9$ (Petrosino S., *et al.*, 2008).

Evaluating the maximum of this spectra we could obtain the dominant frequency of every event at each seismic station.

The dominant frequency, used in the energy calculation, it is useful to understand what is the main contribution in frequencies associated with the analyzed data set. In addition, observing all the spectra, smaller contributions at different frequency from those of LP could be further detected and maybe attributable to other reasons (i.e. noise, see Section 6.4.3).

In the following figures (Figure 60, Figure 61, Figure 62 and Figure 63) some spectra are showed in order to illustrate the main features discovered through this analysis.

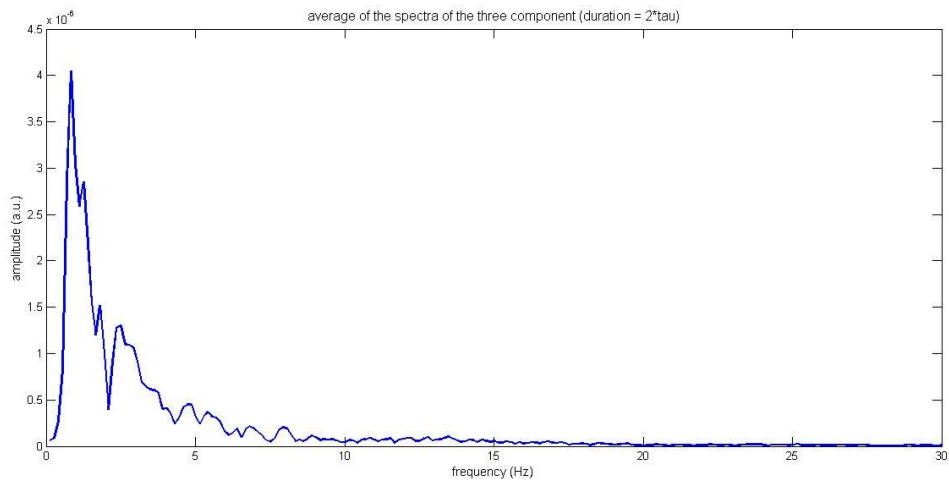


Figure 60 Spectrum of the sample event, on 26th October 2006 at 00:05 recorded at the seismic station ASB2. Typical spectrum with the main peak at 0.83 Hz, and other minor peaks.

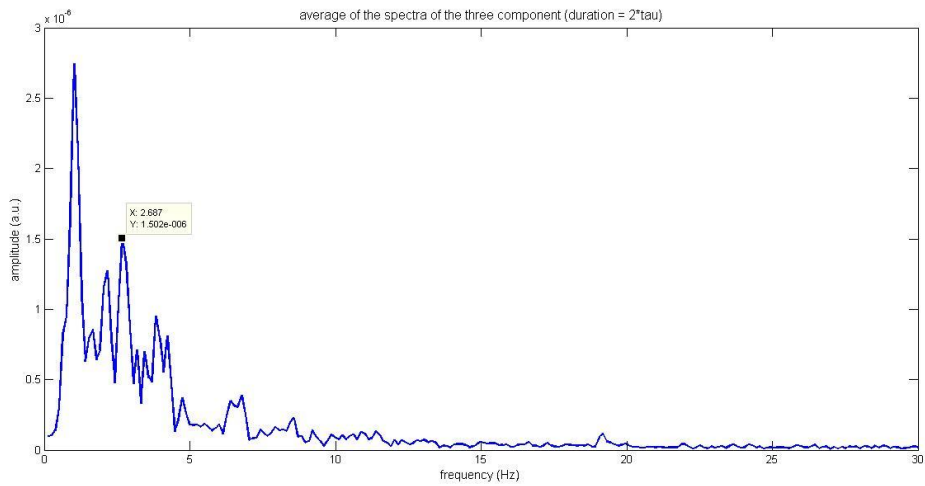


Figure 61 Spectrum of the event on 27th October 2006 at 09:04 recorded at the seismic station ASB2. Typical spectrum with a minor peak at 2.68 Hz.

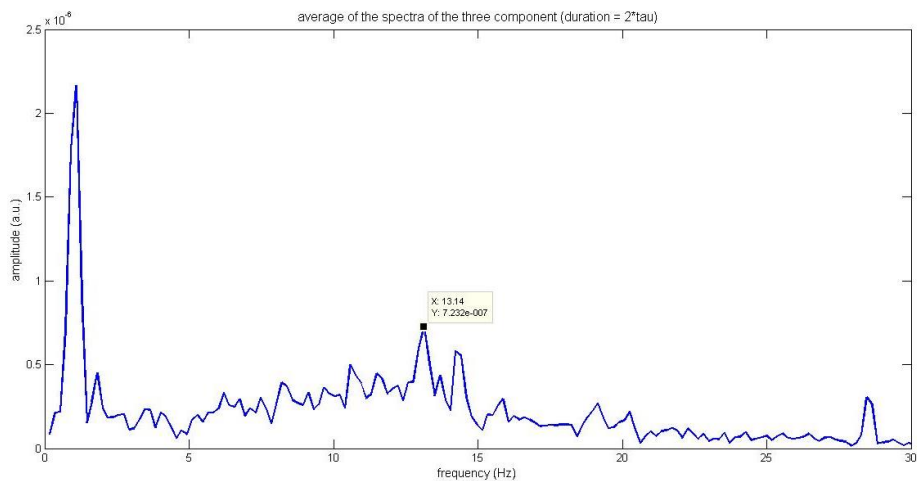


Figure 62 Spectrum of the event on 27th October 2006 at 10:52 recorded at the seismic station AMS2. Typical spectrum with a minor peak at 13.14 Hz.

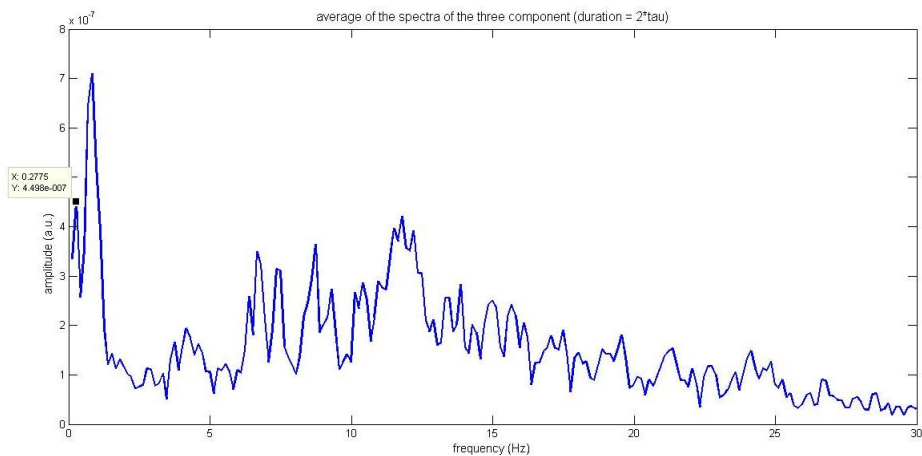


Figure 63 Spectrum of the event on 27th October 2006 at 22:08 recorded at the seismic station AMS2. Typical spectrum with a minor peak at 0.27 Hz and some other peaks at major frequencies than the LP characteristics.

The main peak is showed for all the spectra (Figure 60, Figure 61, Figure 62, Figure 63) but some other peaks are evident. In all the spectra, a peak at a frequency between 2 Hz and 3 Hz is clearly visible. This is a feature of almost the entire data set so it may be imputable to some noise contribute. Considering the main contributors to the background seismic noise (Section 6.4.3) we could deduce that the reason why there is a contribute at about 2 Hz – 3 Hz may be ascribed to the anthropic noise. Since the Solfatara surrounding area is densely populated (like the rest of the Campi Flegrei as well), to attribute the 2-3 Hz frequency contribution to the anthropic noise is reasonable.

A further peak at higher frequencies (between 10 Hz and 15 Hz) could be seen in Figure 62 and Figure 63, that we noticed also in some spectrograms

(Section 6.4.1). In Figure 64 the spectrum of the event recorded on 2006 October 26th at 9:14 at the station ASB2 is showed. In this figure the peak of the 10.6 Hz frequency is visible and this peak is also visible in the spectrogram for the same signal reported in Figure 49.

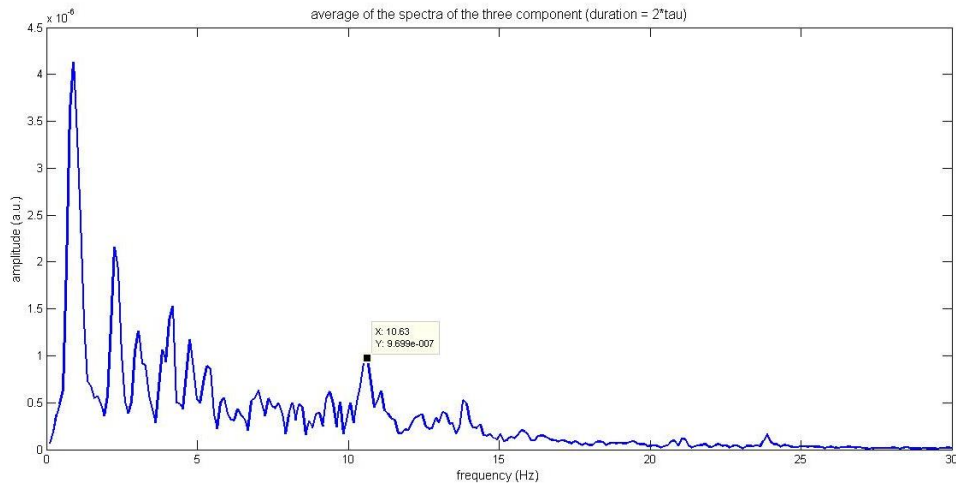


Figure 64 Spectrum of the event on 26th October 2006 at 9:14 recorded at the seismic station ASB2. A peak at 10.6 Hz is also in spectrogram for the same signal reported in Figure 49.

The method described in the Section 7 is then applied to the LP seismicity recorded at Campi Flegrei caldera in 2006 at ASB2, AMS2, TAGG and BGNB seismic stations.

Before the magnitude estimation, we selected the signals that could be analysed. The previous study in the time and frequency domain (Section 6.1 and Section 6.4) allowed us to select, and then reject, the waveforms with the lower SNR and the ones with high peaks of the noise spectrum.

At this point we obtained the data set that has to be analysed.

First of all we verified the low content in frequency of the seismic events analysed. In order to do this, the dominant frequency, obtained from the spectral analysis, have been evaluated, searching for the frequency corresponding to the maximum of the spectrum of each event saving it as the dominant frequency.

For each event, the dominant frequencies are plotted in Figure 65. In this figure the results obtained for the different seismic stations are differently coloured, the blue dots are for the ASB2 events, the red dots for TAGG events, the green dots for AMS2 and the black dots for the BGNB one.

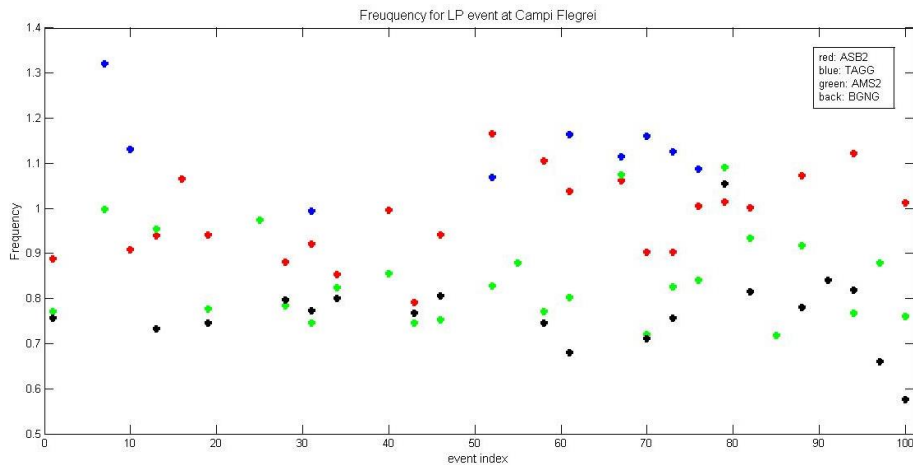


Figure 65 Dominant frequency for the entire set of LP seismic data analysed in this work. Each integer number in the x axes (event index) represents a different event. The different colours indicate the LP events belonging to the different seismic stations: red for ASB2, blue for TAGG, green for AMS2 and black for BGNB.

The dominant frequency values range from 0.5 Hz to 1.4 Hz, so they exhibit the typical frequency for the LP seismicity (Figure 25).

The dominant frequencies are greater for the signals recorded at in ASB2 and TAGG seismic stations and lower for AMS2 and BGNB (Figure 25). This feature could be attributed to a noise contribution or to the distance of the seismic station to the source of the LP events. Since we discarded the events with a high noise contribute we are confident that, even if a noise perturbation could still be present, the reason of the observed trend for the frequencies values due to the different distances of the seismic stations. The higher frequencies values are for TAGG station and then, in decreasing order, for ASB2, AMS2 and BGNB (see Figure 65), in fact the greatest hypocentral distance is for TAGG station, and then, in decreasing order, for ASB2, AMS2 and BGNB (the distances of the four seismic stations from the hypocenters are showed in Table 3).

Seismic station	Distance
TAGG	2561 Km
ASB2	1851 Km
AMS2	1625 Km
BGNB	1265 Km

Table 3 Hypocentral distances of the studied LP events at Campi Flegrei to the four seismic stations.

8.1.2 The magnitude estimation

As second step we calculated the magnitude through Eq. 51.

The error associated to the magnitude values is estimated to be 0.2 (as discussed in Section 7.4.1). The obtained results are represented in Figure 66, where the magnitude values for each event recorded at the four seismic stations are shown: the blue symbols are for the magnitude values of the events recorded at the ASB2 station, the red symbols for TAGG station, the green symbols for the magnitude of AMS2 station and the black ones for BGNB seismic station.

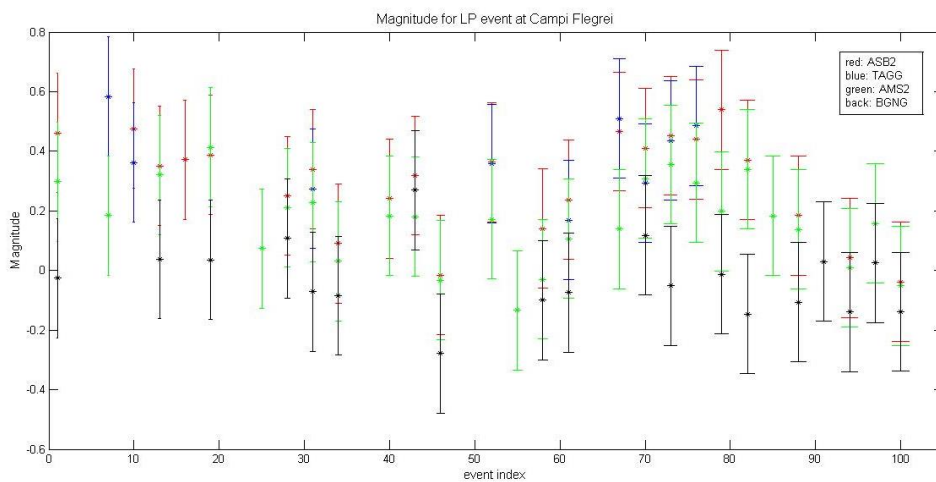


Figure 66 Magnitude values for the entire set of LP seismic data of Campi Flegrei LP, with error representation. Each integer number in the x axes (event index) represents a different event. The different colours indicate the LP events belonging to the different seismic stations: red for ASB2, blue for TAGG, green for AMS2 and black for BGNB.

To better visualize the obtained results we also represented them without the errorbar in Figure 67.

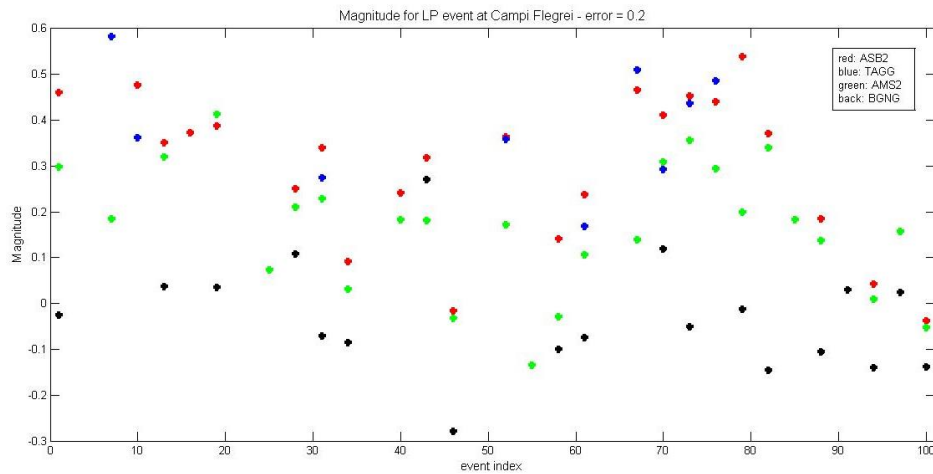


Figure 67 Magnitude values obtained for the entire set of LP seismic data of Campi Flegrei. Each integer number in the x axes (event index) represents a different event. The different colours indicate the LP events belonging to the different seismic stations: red for ASB2, blue for TAGG, green for AMS2 and black for BGNB. The error on the magnitude is 0.2.

The magnitude values span in a range between -0.3 ± 0.2 and 0.6 ± 0.2 . It is evident that the swarm of low-frequency events is characterized by a low energy content. The events recorded at BGNB station show the lower magnitude values, possibly due to the source-receiver distance (see Table 3). We also separated the results obtained for the magnitude at the four seismic stations and plotted in the following figures (Figure 68, Figure 69, Figure 70 and Figure 71).

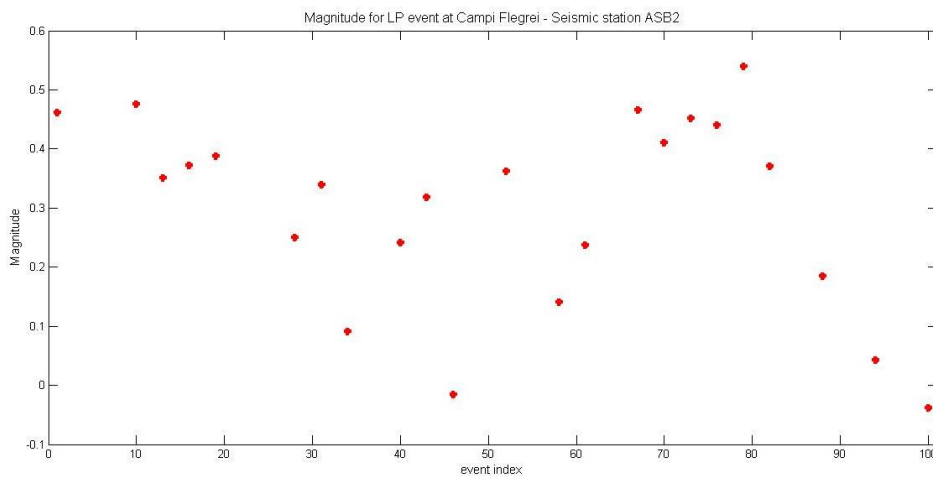


Figure 68 Magnitude values obtained for the LP data-set recorded at Campi Flegrei at ASB2 seismic station. Each integer number in the x axes (event index) represents a different event.

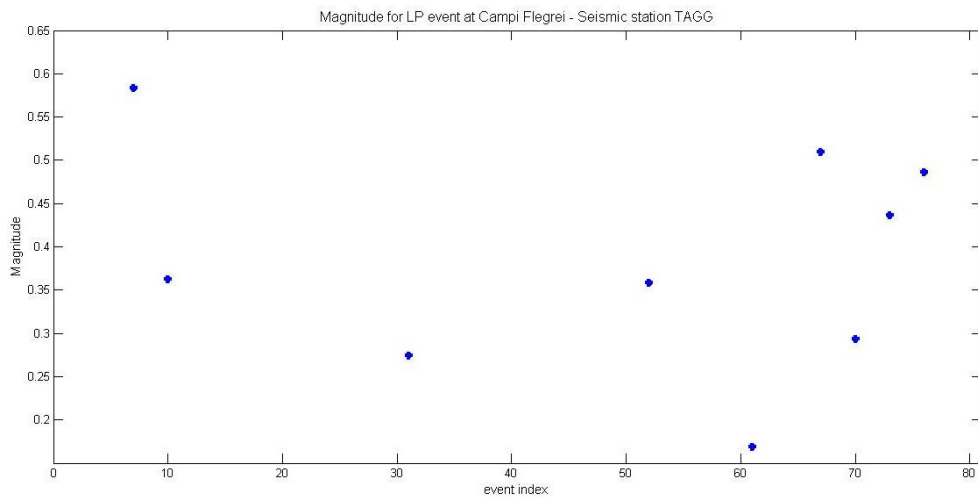


Figure 69 Magnitude values obtained for the LP data-set recorded at Campi Flegrei at TAGG seismic station. Each integer number in the x axes (event index) represents a different event.

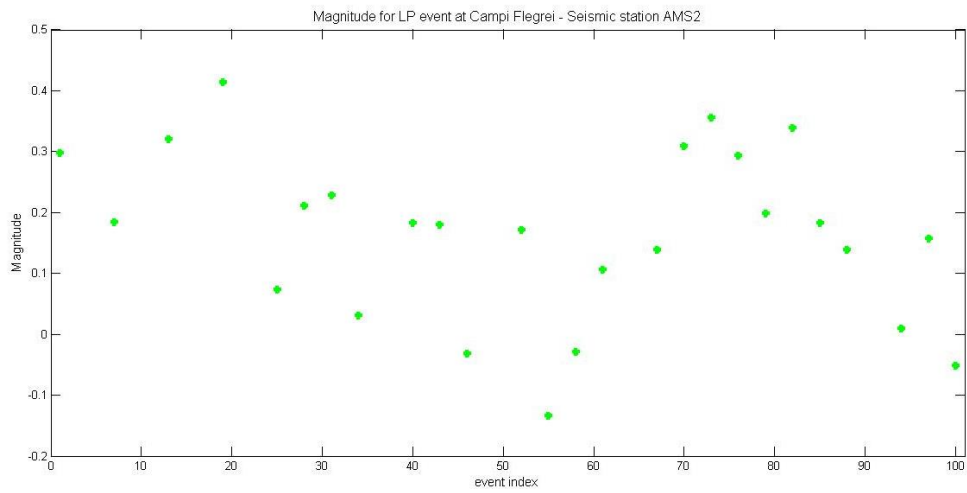


Figure 70 Magnitude values obtained for the LP data-set recorded at Campi Flegrei at AMS2 seismic station. Each integer number in the x axes (event index) represents a different event.

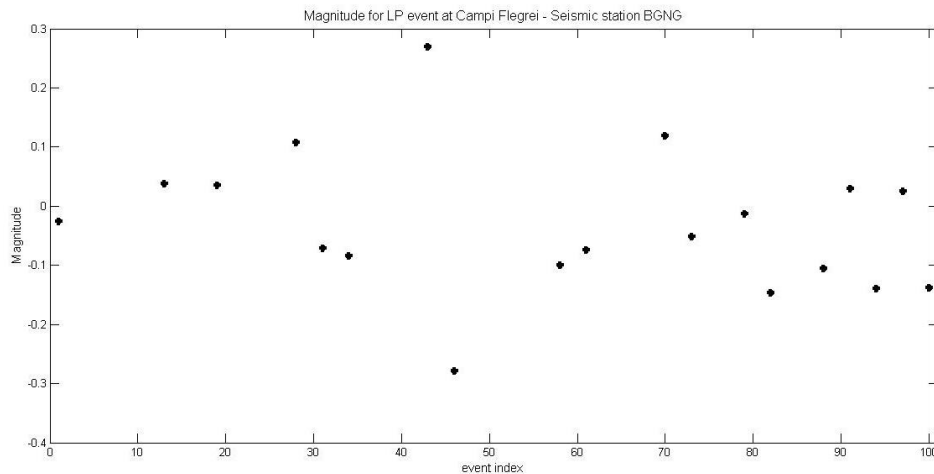


Figure 71 Magnitude values obtained for the LP data-set recorded at Campi Flegrei at BGNB seismic station. Each integer number in the x axes (event index) represents a different event.

For the events recorded at ASB2 seismic station the magnitude values are in the range -0.1 Hz – 0.6 Hz, the event recorded at TAGG seismic station show magnitude values in the range 0.1 Hz – 0.6 Hz, the event recorded at AMS2 seismic station show magnitude values in the range -0.2 Hz – 0.5 Hz and finally the event recorded at BGNB seismic station show magnitude values in the range -0.4 Hz – 0.3 Hz. These results point out that the stations with the greater hypocentral distances show larger magnitude values.

In order to investigate the results we also selected an event (whose waveforms was possible to analyze at all the seismic stations) observing the magnitude values obtained at the different seismic stations. We selected the event recorded on 2006 October 26th at 18:23 and the results are showed in the following table (Table 4).

	TAGG	ASB2	AMS2	BGNB
M	0.3±0.2	0.3±0.2	0.2±0.2	-0.1±0.2
Distance (Km)	2561	1851	1625	1265

Table 4 Magnitude values and hypocentral distances for the event recorded on 2006 October 26th at 18:23 at the four different seismic stations.

The magnitude values obtained for the waveforms recorded at TAGG and ASB2 are the greater ones and this is in agreement with the hypocentral distances of the stations. Moreover, even if the hypocentral distance of the ASB2 station is much less than that of TAGG, the magnitude values obtained for ASB2 and TAGG are the same (within the error value).

8.1.3 Searching for a scaling law

An important task that could be very interesting in a volcano seismology context, is to investigate on a possible scaling law for the magnitude values of LP events, to eventually improve the knowledge about the LP source.

Once established that the duration is not correlated to the energy contribute of the events (Section 6.3), we decided to use the dominant frequency as the parameter to study for the scaling law.

As a first attempt to investigate on a possible scaling law, we represented the magnitude values versus the dominant frequencies for the entire data set at the four seismic station using blue dots for the events recorded at ASB2 station, red dots for the events at TAGG station, green dots for those recorded at AMS2 station and black ones for the events recorded at BGNB (Figure 72). To better visualize the results we also separated them for the four seismic stations and represented the magnitude versus the dominant frequencies as well (Figure 73, Figure 74, Figure 75, Figure 76).

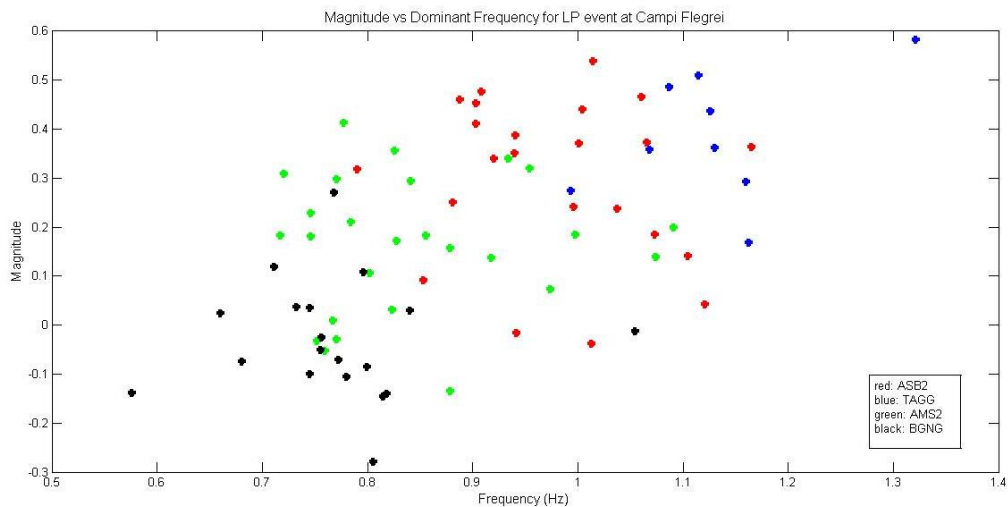


Figure 72 Magnitude versus dominant frequency for the LP seismic events at Campi Flegrei recorded at October 2006. Red dots are for the events recorded at ASB2 seismic station, blue dots for TAGG station, green symbols for AMS2 and black ones for BGNB seismic station. The error on the magnitude values is 0.2.

In Figure 73, Figure 74, Figure 75 and Figure 76, we showed the results obtained for the events recorded at each station.

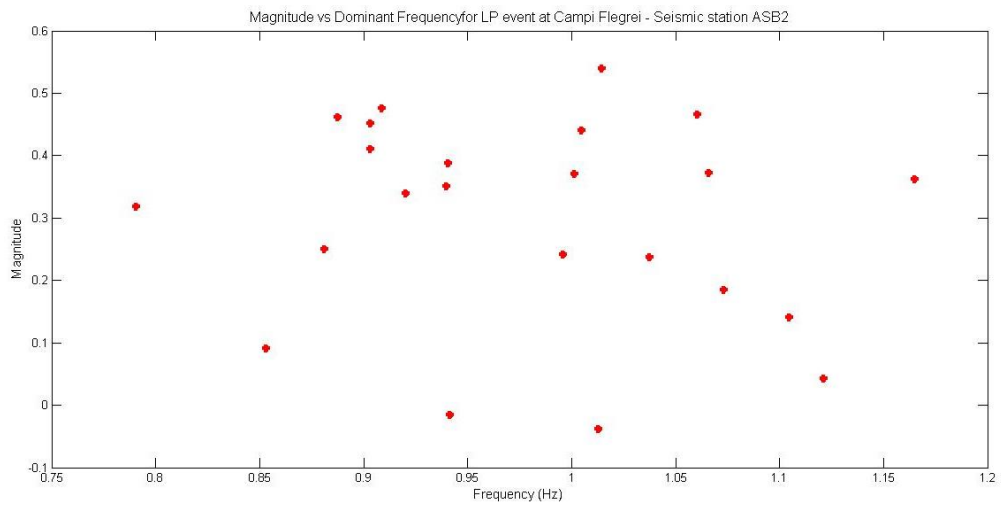


Figure 73 Magnitude versus dominant frequencies for the event recorded at the ASB2 seismic station. The error on the magnitude values is 0.2.

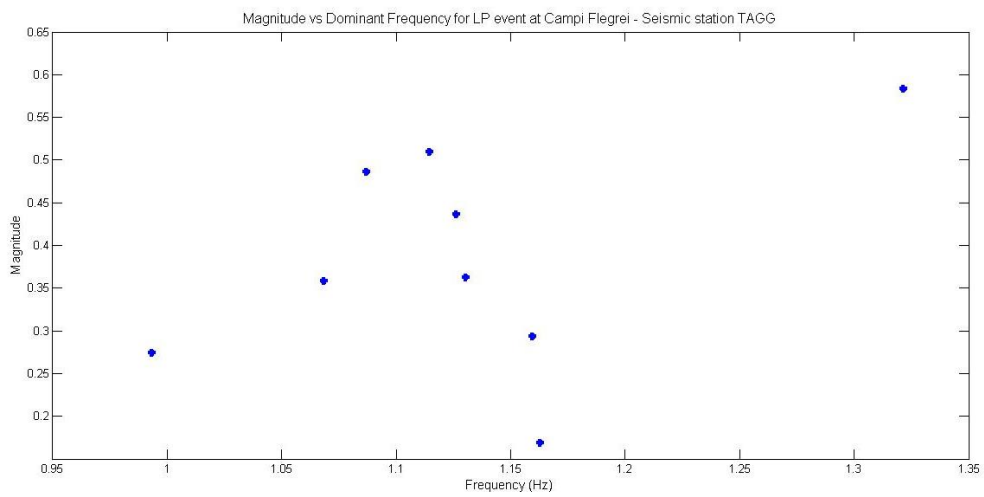


Figure 74 Magnitude versus dominant frequencies for the event recorded at the TAGG seismic station. The error on the magnitude values is 0.2.

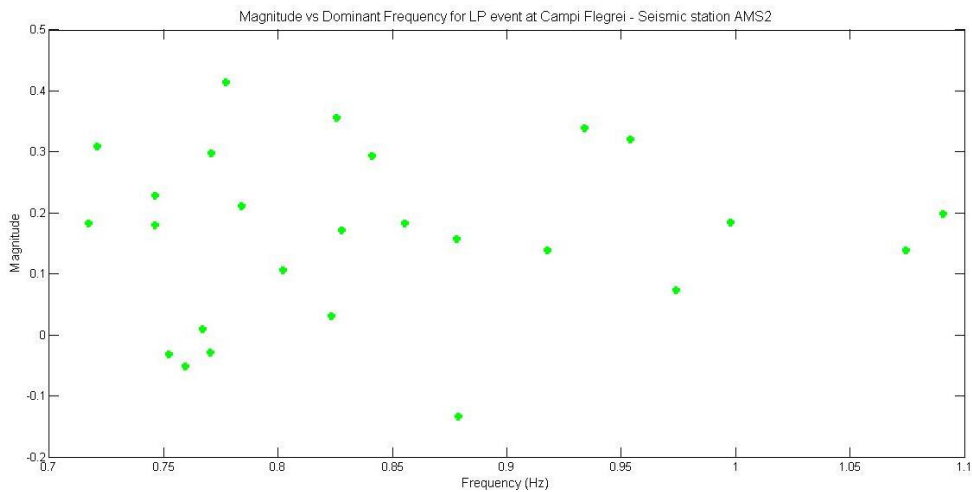


Figure 75 Magnitude versus dominant frequencies for the event recorded at the AMS2 seismic station. The error on the magnitude values is 0.2.

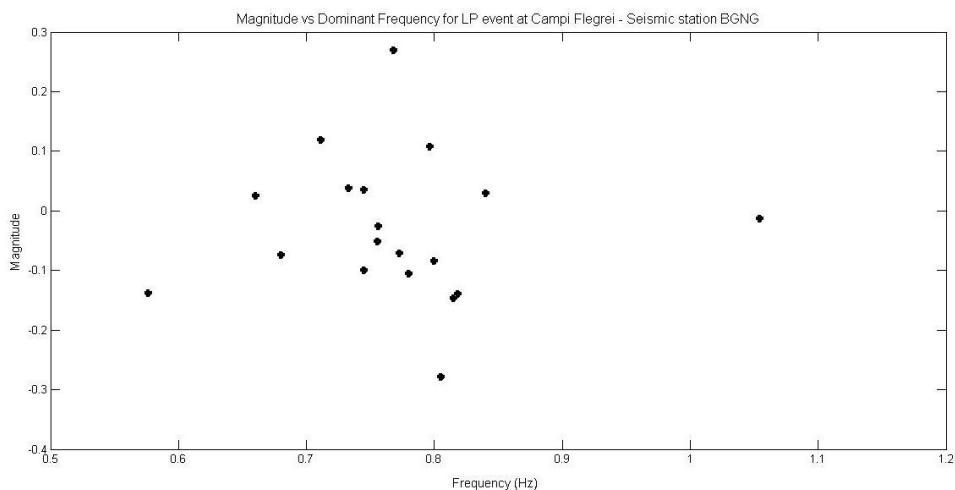


Figure 76 Magnitude versus dominant frequencies for the event recorded at the BGNB seismic station. The error on the magnitude values is 0.2.

Observing Figure 72, a regularity on the behaviour of the magnitude and dominant frequency values is evident. In fact, the results with lower magnitude and also dominant frequency values is BGNB (the one with the smallest hypocentral distance value), and then gradually increasing the values obtained for the event recorded at AMS2 seismic station, ASB2 and finally TAGG seismic station.

Observing also the results separated for each seismic station (Figure 73, Figure 74, Figure 75, Figure 76) no scaling law between the dominant frequency and magnitude appears to be evident.

8.2 Mount Colima

We searched for the magnitude estimation of an LP data set recorded at another volcano: Volcàn de Colima, that is characterized by a very different dynamic respect to the Campi Flegrei area.

Colima is a 3860 m high andesitic strato-volcano and it is considered the most active volcano in Mexico. It shows a wide range of eruptive styles that often occur in cycles. An important eruptive cycle ended in June 2005, but the eruptive activity continued to January 2007 with ash and steam emission (Petrosino, et al., 2011). This eruptive activity was accompanied by different kind of seismicity. In particular the explosions and steam emission were accompanied by Long Period seismic events.

In this work we studied the LP seismicity that occurred during December 2005 at a depth of 1070 m, that was recorded by 3C broad-band seismic stations.

Since no earth quality factor Q is available for this volcano, we performed the path attenuation correction assuming the same quality factor of Etna volcano (Del Pezzo, et al., 1996).

We analyzed the waveforms recorded at two seismic stations: COCA and COBA (see Figure 77).

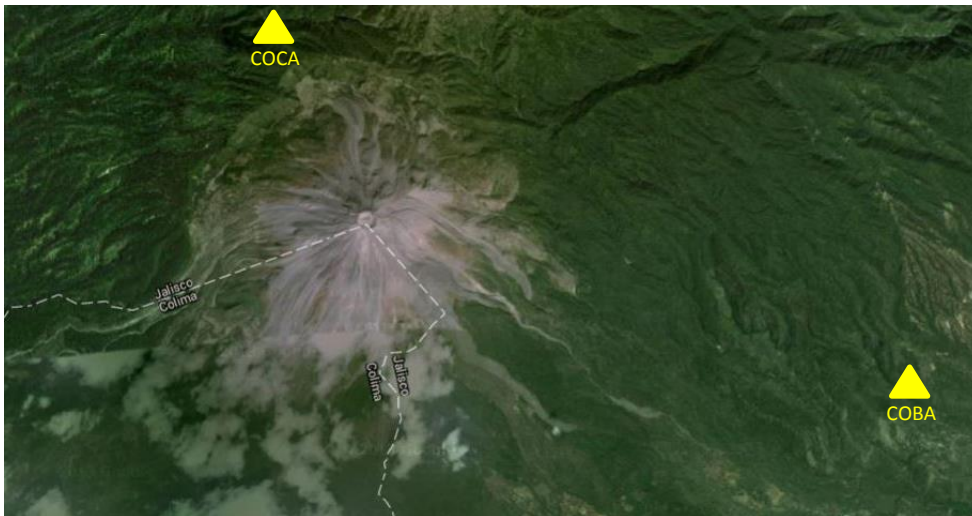


Figure 77 Map of Colima Volcano. Triangles represent the seismic stations (Map from Google.it).

In the following figures (Figure 78 and Figure 79) an example of an LP waveform recorded on 2005 December 3rd at both the seismic stations is plotted.

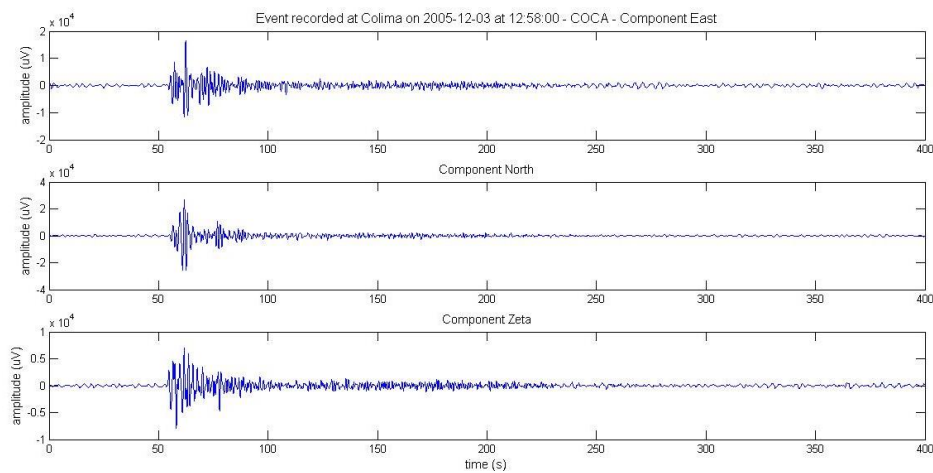


Figure 78 3C waveforms of Colima LP recorded on 2005 December 3rd at COCA seismic station.

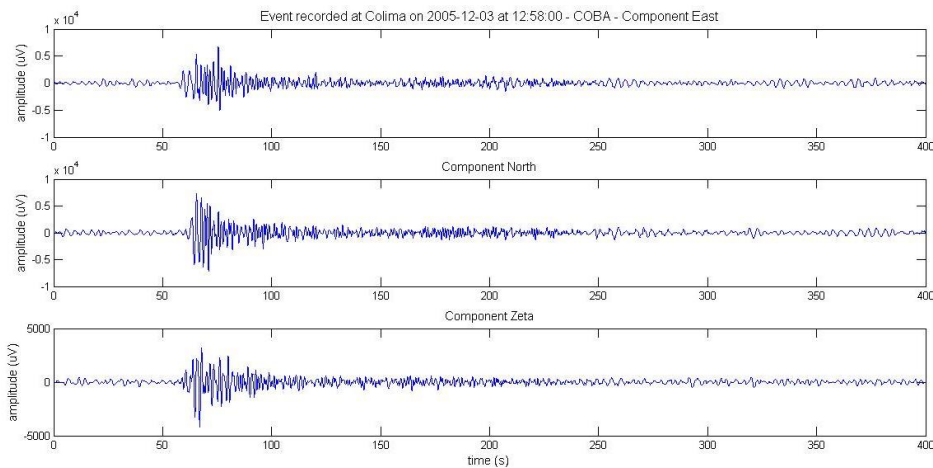


Figure 79 3C waveforms of Colima LO recorded on 2005 December 3rd at COBA seismic station

The waveforms of Colima volcano have a higher SNR respect to those of Campi Flegrei caldera and this make the data analysis easier.

Once selected the data-set that has to be analysed (considering the ones with a higher SNR in which the identification of the onset of the seismic impulse was easier) we performed the ‘ 2τ ’ method (see Section 7.2) to determine the time duration of each waveform and then we could compute the velocity-density spectra for the entire data set, using the Eq. 52.

Studying the spectra of the recorded events we could obtain the dominant frequency of each event at each seismic station.

In Figure 80 and Figure 81, respectively, the dominant frequencies for the events recorded at COCA seismic station and COBA seismic station are plotted.

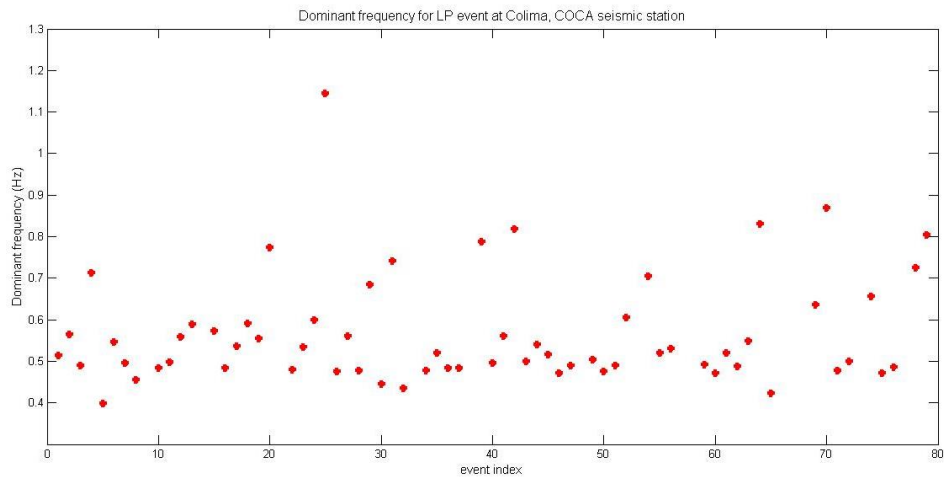


Figure 80 Dominant frequencies of the Colima LP events recorded at COCA seismic station. Each integer number in the x axes (event index) represents a different event.

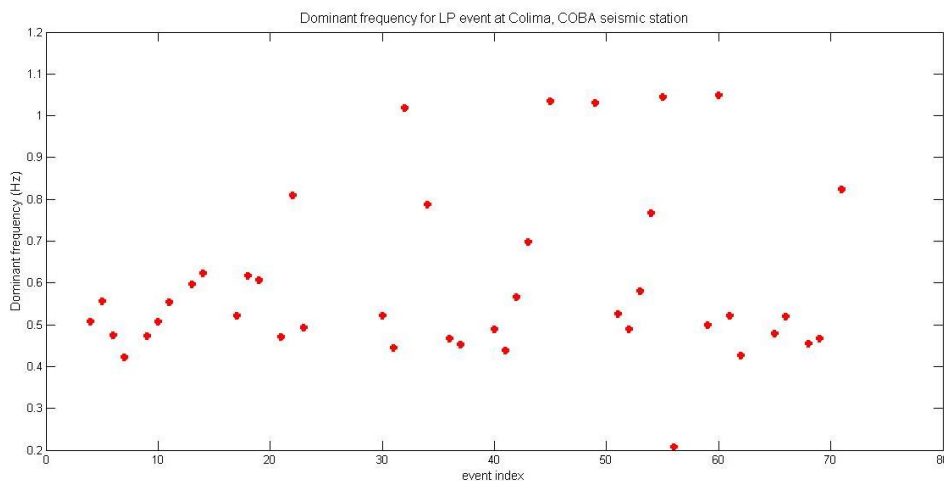


Figure 81 Dominant frequencies of the Colima LP events recorded at COBA seismic station. Each integer number in the x axes (event index) represents a different event.

The dominant frequency values are in the range 0.2 Hz – 1.2 Hz, that is typical for the LP seismicity (see Section 3.1).

As final step, we could estimate the magnitude using Eq. 51. Also in this case the error on the magnitude values is 0.2, but, to better represent the results, we didn't use the error-bars in the following plot. In Figure 82 the magnitude obtained for the events recorded at COCA seismic station are plotted, in Figure 83 the magnitude of the events recorded at COBA seismic station are plotted.

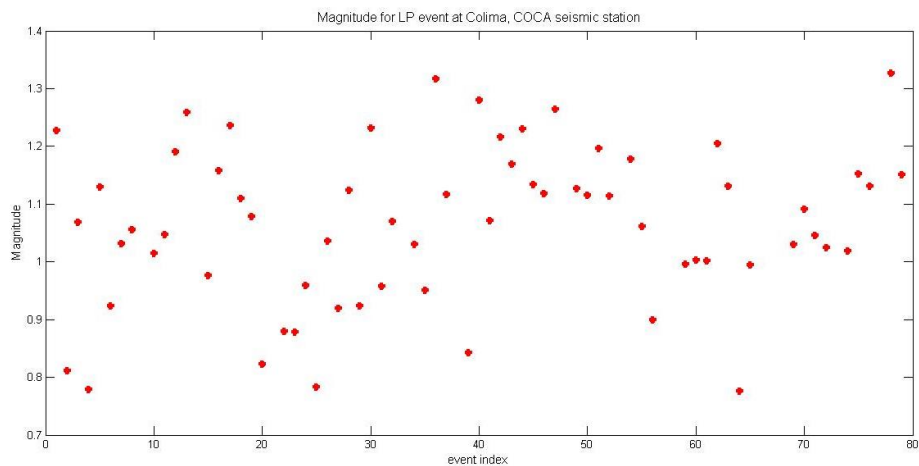


Figure 82 Magnitude values obtained for the LP events recorded at Colima volcano by COCA seismic station. Each integer number in the x axes (event index) represents a different event.

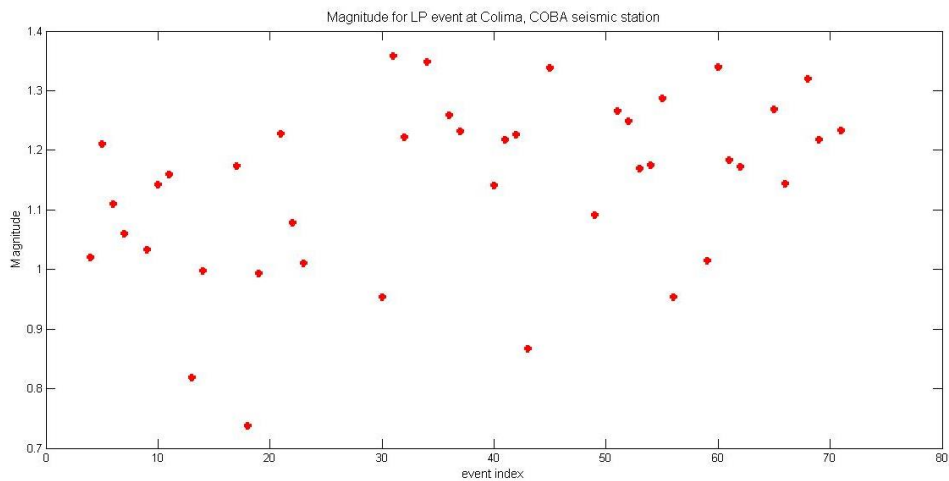


Figure 83 Magnitude values obtained for the LP events recorded at Colima volcano by COBA seismic station. Each integer number in the x axes (event index) represents a different event.

The obtained magnitude values are in the range between 0.7 ± 0.2 and 1.4 ± 0.2 . The analysed swarm of low-frequency events is characterized by a low energy content, but clearly higher than that of Campi Flegrei.

The magnitude values obtained for the two different seismic station are in the same range.

Finally, we plotted the magnitude values versus the dominant frequencies to possibly point out a scaling law also for the case of Colima volcano. In Figure 84 and Figure 85, the magnitude versus dominant frequency for COCA and COBA seismic stations, respectively, are plotted.

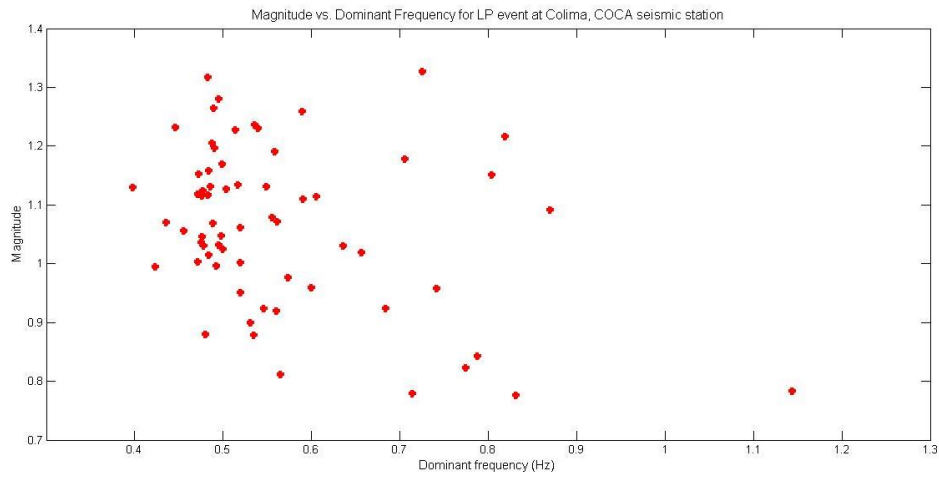


Figure 84 Magnitude versus dominant frequency for the events LP recorded at Colima by COCA seismic station.

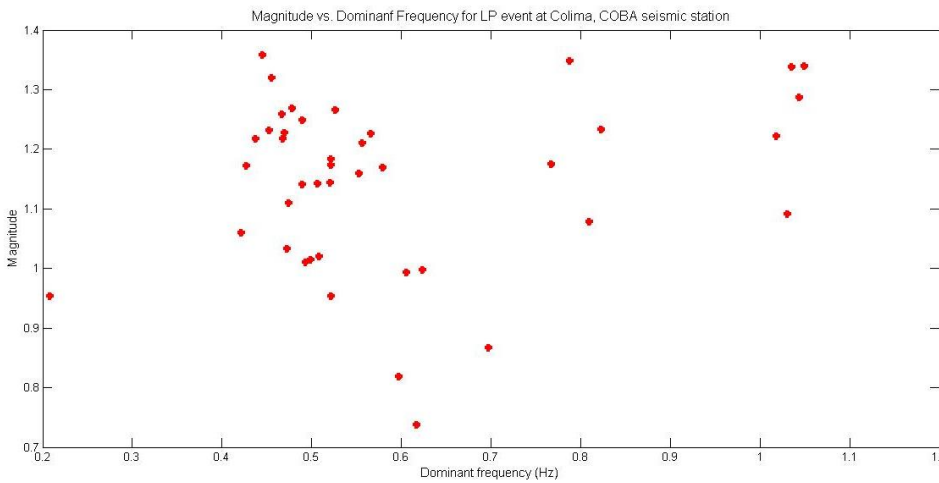


Figure 85 Magnitude versus dominant frequency for the events LP recorded at Colima by COBA seismic station.

The results didn't point out any scaling law also in this case.

Estimating the magnitude also for the Colima LPs we could demonstrate the simply applicability of the proposed algorithm also for LP seismicity with different features, confirming also the absence of a scaling law between magnitude and dominant frequency.

8.3 Mount Etna

We estimated the magnitude value also for an LP event recorded at Etna volcano.

Etna volcano is a strato-volcano 3330 m high, located in Sicily (South Italy). It covers an area of about 1,250 km² with a basal circumference of 140 km. It shows almost continuous eruptive cycles and also LP events are repetitive (Patanè, *et al.*, 2011).

An effusive eruption started on 2004 September with thousands of LP events. We analyzed a low frequency event recorded on 2005 August at ET00 seismic station. It was located in the summit crater at 2700 m a.s.l. (Lockmer, *et al.*, 2007), and recorded by 3C digital seismic stations (Figure 86).

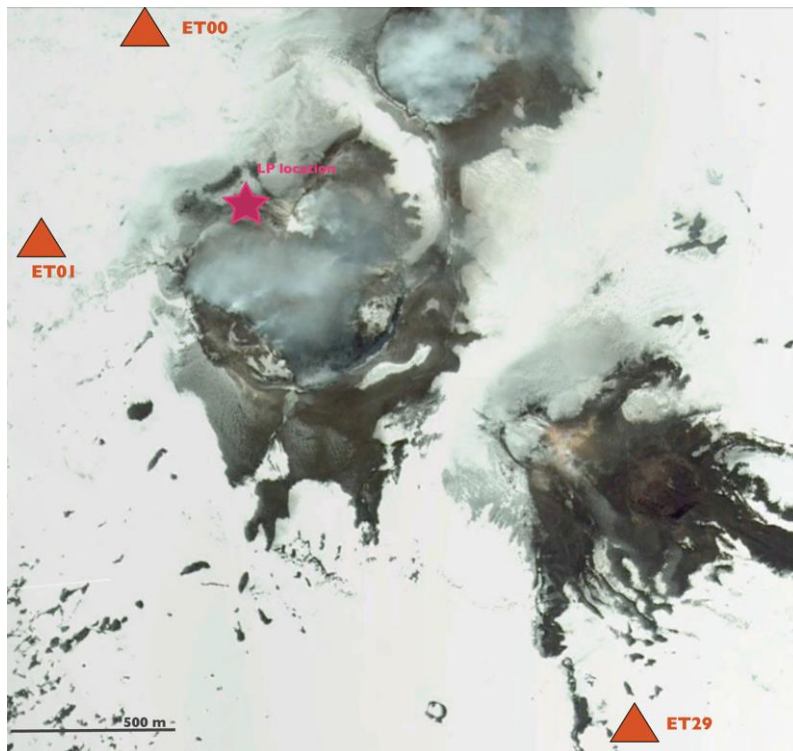


Figure 86 Map of Mt Etna superimposed by the localizations of the seismic stations (triangles) and the LP event (star). The depth of this selected event is 2700 m a.s.l. (Del Pezzo, *et al.*, 2013).

As first step we evaluated the ' 2τ ' time duration (see Section 7.2).

In the following figure (Figure 87) we plotted the 3C waveforms superimposed with the duration selection (red lines).

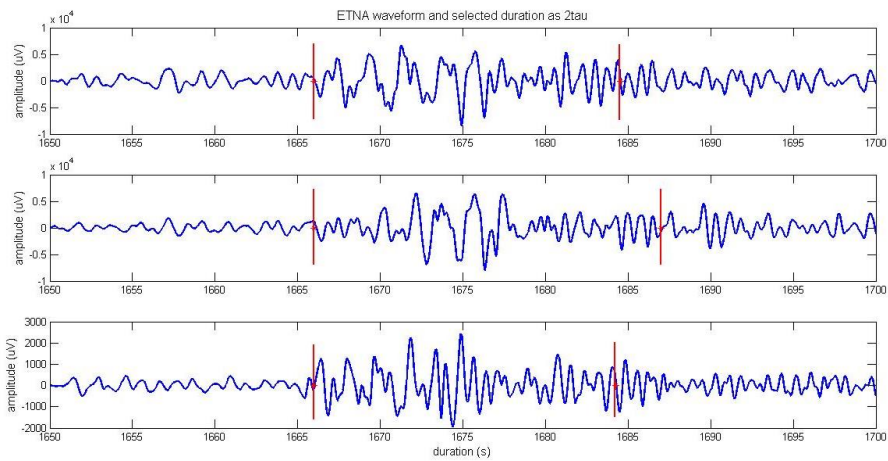


Figure 87 3C waveforms of the LP recorded at Etna volcano on 2005 August superimposed with the duration selection (red lines).

Then we performed the velocity-density spectrum (see Section 7.3) corrected by the attenuation using the attenuation parameter obtained by (Del Pezzo, *et al.*, 1996) and we represented it in the following figure (Figure 88). The dominant frequency obtained is 2.5 Hz.

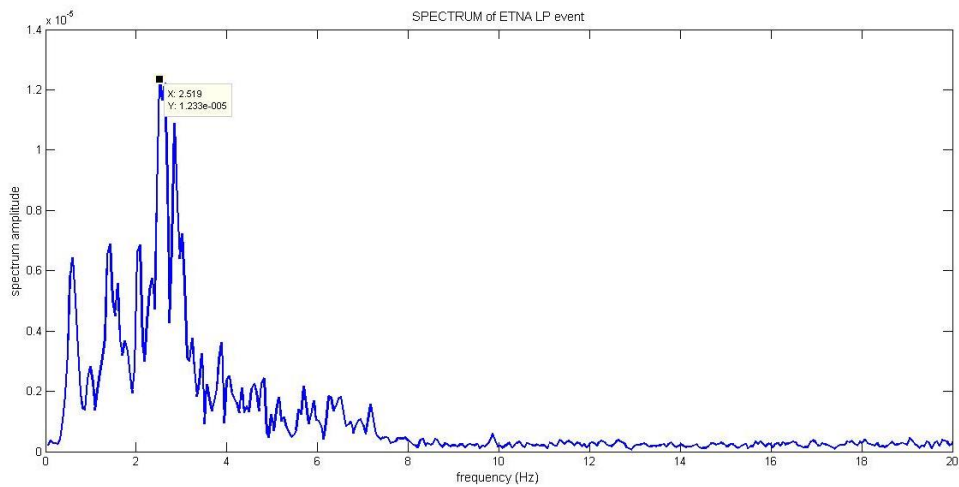


Figure 88 Spectrum of the LP recorded at Etna volcano on 2005 August and its dominant frequency.

We could finally evaluate the magnitude using Eq. 50 and we obtained the value: 1.4 ± 0.2 .

9. Conclusions and future developments

In the present doctoral thesis we approached a method for the determination of the magnitude of Long Period events. No previous studies on this topic exist, possibly due to the intrinsic difficulties in representing the corrected source for the low frequency seismicity.

After a first step of study of the features of the LP seismicity recorded on October 2006 at Campi Flegrei caldera. In November 2004 a new phase of uplift started and culminated in October 2006 leading to 4 cm of positive ground deformation. The deformation has been accompanied by swarms of VT and LP earthquakes all localized around the Solfatara crater (see Figure 24) (Saccorotti, *et al.*, 2007). This crisis didn't end with an eruption.

We firstly proposed several methods for the duration evaluation and for the energy determination. We calculated the duration through a visual inspection of the waveform or of the envelope of each waveform and we also developed two algorithms to routinely obtain this duration (Section 6.2). The routines led to unstable results, small variation of the parameters involved, resulted in great variations in the duration results, so we did not use those routines and visually selected the events-duration also using sometimes a supporting function based on the envelope of the waveforms (see Section 6.2.1).

We developed different methods for the energy evaluation based on a theoretical approaches or on the area of the envelope of the waveforms calculated in different ways (Section 6.3).

Using the different method we obtained, an uncorrelation between the energy and the duration of the LP events (Section 6.3.3). These results proved that the duration for the LP events have a different meaning respect to the duration of a VT event.

The time sustained source of an LP event leads to different waveforms respect to the VT ones and possibly it is responsible for the behaviour of the signal duration versus the energy. In fact an LP event with short (source) duration and high maximum amplitude may have the same energy of an LP with greater duration and lower maximum amplitude.

As final step we moved in the frequency domain and evaluated the energy as the integral of the squared velocity density spectrum.

Evaluating the spectrum of each LP event, considering the path attenuation correction and the transduction constant of the instrument, we could obtain the dominant frequency value. We evaluated the dominant frequency for the Campi Flegrei LP data-set (Section 8.1.1), for the Colima LP data-set (events

recorded on December 2005) (Section 8.2) and for an LP event recorded at Etna volcano on August 2005 (Section 8.3).

The obtained dominant frequencies values were in the typical range of LP event (see Section 3.1).

Our scope was to define a simple method for the magnitude evaluation possibly useful for a routinely and in quasi-real time practice of a volcanological observatory.

In order to obtain this goal, we evaluated the integral of the squared velocity density spectrum for each LP event and then we consider as magnitude M_{LP} the moment-magnitude of a VT with the same integral value of the LP one.

The magnitude values obtained for Campi Flegrei data-set span in the range -0.3 ± 0.2 and 0.6 ± 0.2 , so they confirm the low energy content of this seismicity. The lower magnitudes have been obtained for the BGNB waveforms and the greater for ASB2 events and this could be due to the different source-receiver distance (see 8.1.2).

The attenuation parameters (Section 7.3) are calibrated on VT events, so, to minimize this dependence on the distance, a better evaluation of the attenuation parameters specific for LP seismicity could be necessary.

The last step was to make a first attempt in searching for a scaling law for the magnitude. For this scope we deeply analysed the behaviour of the magnitude as a function of the dominant frequency. In both data-set (Campi Flegrei (Section 8.1.2) and Colima (Section 8.2), differently from the case of VT events (Bak, *et al.*, 2002, Beresnev, 2009), we didn't find a scaling law between the magnitude and the dominant frequency.

We are also confident that this method could be helpful in the determination of the magnitude of LP events recorded in non-volcanic areas (e.g. Piccinini & Saccorotti, 2008) or in other sectors broader to volcano seismicity (for instance, the size of slow-slip events, landslides, large glacial earthquakes, low-frequency tectonic earthquakes).

10. List of figures

FIGURE 1 VT EVENT RECORDED AT MT. MERAPI (INDONESIA). ARRIVALS OF P AND S WAVES CLEARLY DISTINGUISHABLE. THE COLOUR CODING REPRESENTS NORMALIZED AMPLITUDE SPECTRAL (WASSERMANN, 2011).	10
FIGURE 2 LP EVENT RECORDED AT MT. MERAPI. THE DOMINANT FREQUENCY IS ABOUT 1 HZ (WASSERMANN, 2011).	11
FIGURE 3 EXAMPLE OF LP EVENT RECORDED AT TWO DIFFERENT STATIONS AT REDOUBT VOLCANO (ALASKA) (WASSERMANN, 2011). THE SPINDLE SHAPE WAVEFORM IS ALSO KNOWN AS ‘TORNILLO’	11
FIGURE 4 TREMOR SIGNAL RECORDED AT MT. SEMERU (INDONESIA) (WASSERMANN, 2011).	12
FIGURE 5 HYBRID EVENT REDOUBT VOLCANO (ALASKA) (WASSERMANN, 2011).....	13
FIGURE 6 WAVEFORMS OF LP EVENTS RECORDED AT DIFFERENT VOLCANOES: KUSATSU-SHIRANE, GALERAS, KILAWEA AND REDOUBT. THE SIGNATURES ARE CHARACTERIZED BY DIFFERENT Q VALUES: THE Q VALUES OF KILAWEA AND REDOUBT EVENTS ARE BETWEEN 20 AND 50, THE Q VALUES OF KUSATSU-SHIRANE AND GALERAS ARE HIGHER THAN 100 (CHOUET, 2003).....	14
FIGURE 7 GEOMETRY OF THE CRACK MODEL (CHOUET, 2003).....	15
FIGURE 8 CAMPI FLEGREI AREA, WITH THE MAIN VOLCANO STRUCTURES (VULCANI D'ITALIA - UNIROMA3).	17
FIGURE 9 CRATER OF <i>MONTE NUOVO</i> , (A) FROM (VULCANI D'ITALIA - UNIROMA3), (B) (OV-INGV)	20
FIGURE 10 DISPOSITION OF VOLCANIC SYSTEMS IN THE PHLEGREAN CALDERA. THE DASHED LINES APPROXIMATE THE AREAS OF LOWERING, AS A RESULT OF THE <i>IGNIMBRITE CAMPANA</i> ERUPTION (THE EXTERNAL ONE) AND THE <i>TUFO GIALLO NAPOLETANO</i> ERUPTION (THE INTERNAL). (VULCANI D'ITALIA - UNIROMA3)	20
FIGURE 11 TEMPLE OF SERAPIS IN POZZUOLI (VULCANI D'ITALIA - UNIROMA3).	22
FIGURE 12 SUBMERGED ROMAN PORT IN THE GULF BETWEEN BAIA AND BACOLI (VULCANI D'ITALIA - UNIROMA3)	22
FIGURE 13 LOCALIZATIONS OF VT EVENTS, RECORDED BETWEEN 19 TH AND 28 TH OCTOBER 2006, IN THE CAMPI FLEGREI CALDERA. (OV-INGV)	23
FIGURE 14 VARIATIONS OF <i>CAPOSALDO</i> N.25, IN THE CORSO UMBERTO IN POZZUOLI CITY, MEASURED BY GEOMETRIC LEVELING (OV-INGV)	24
FIGURE 15 TIME SERIES FROM 2006 OF THE VERTICAL DEFORMATION IN POZZUOLI, MEASURED BY THE GPS PERMANENT STATION (OV-INGV)	25
FIGURE 16 PLANIMETRIC DISPLACEMENTS IN THE PHLEGREAN AREA IN 2008-2011 PERIOD (OV-INGV). 25	
FIGURE 17 MAGNITUDE OF SEISMIC EVENTS FROM 2006 TO 2011 (OV-INGV).....	26
FIGURE 18 VERTICAL GROUND DEFORMATION AT THE STATION RITE (POZZUOLI) SINCE 2000 TO 31 ST JANUARY 2013 (OV-INGV, BOLLETTINO MENSILE VULCANI CAMPANI, 2012).	27
FIGURE 19 TEMPORAL SERIES OF VERTICAL GROUND DEFORMATION AT RITE STATION (POZZUOLI), SINCE 1 ST JANUARY 2012 TO 4 TH FEBRUARY 2013 (OV-INGV, BOLLETTINO MENSILE VULCANI CAMPANI, 2012).	27
FIGURE 20 SEISMIC NETWORK OF OSSERVATORIO-VESUVIANO, (OV-INGV).....	28
FIGURE 21 MAP OF OSSERVATORIO VESUVIANO SEISMIC NETWORK OPERATING AT CAMPI FLEGREI AREA (OV-INGV). BLUE SYMBOLS REFERS TO THE PERMANENT NETWORK AND YELLOW SYMBOLS TO THE TEMPORARY ONE. STATIONS EQUIPPED WITH SHORT PERIOD SENSOR ARE MARKED WITH CIRCLES AND THE TRIANGLE ARE USED FOR THE BROADBAND SENSOR STATIONS. THE CIRCLE WITH THE BLACK POINT INSIDE REFERS TO THE ARRAY (SACCOROTTI, <i>ET AL.</i> , 2007).	29

FIGURE 22 (A) NUMBER OF VT EARTHQUAKES, ENERGY RELEASE AND GROUND VERTICAL DEFORMATION IN POZZUOLI, FROM GPS MEASUREMENTS. (B) NUMBER OF VT AND LP EARTHQUAKES DURING 6 HOURS IN THE 20 TH -30 TH OCTOBER 2006 CRISIS (SACCOROTTI, <i>ET AL.</i> , 2007).....	30
FIGURE 23 STACKED VELOCITY SEISMOGRAMS FOR THE THREE CLUSTERS, FROM THE NS COMPONENT OF STATION ASB2, INDIVIDUALLY NORMALISED TO THEIR MAXIMUM AMPLITUDE (PEAK-TO-PEAK) (SACCOROTTI, <i>ET AL.</i> , 2007).....	31
FIGURE 24 LOCATIONS OF THE THREE CLUSTERS OF LP EVENTS, SUPERIMPOSED TO A MAP OF THE SOLFATARA VOLCANO (SACCOROTTI, <i>ET AL.</i> , 2007). THE THREE COLORS ARE RELATIVE TO THE THREE CLUSTERS OF EVENTS (SACCOROTTI, <i>ET AL.</i> , 2007).	32
FIGURE 25 DOMINANT FREQUENCY (A) AND QUALITY FACTOR (B) FOR THE RADIAL COMPONENT OF THE LP EVENTS AT STATION ASB2. DIFFERENT TONES CORRESPOND TO EVENT OF DIFFERENT CLUSTER (SACCOROTTI, <i>ET AL.</i> , 2007).....	33
FIGURE 26 (A) DAILY AVERAGE TEMPERATURE (INFRARED MEASURES) AT BOCCA GRANDE FUMAROLE OF SOLFATARA (SOLID LINE) COMPARED WITH THE STEAM VELOCITY AT THE SAME PLACE (GREY DOTS). THE VALUES ARE NORMALIZED. (B) DAILY NUMBERS OF VT (BLACK LINE) AND LP (GREY LINE) ACTIVITY (CUSANO, <i>ET AL.</i> , 2008).....	34
FIGURE 27 POSSIBLE SCENARIO FOR THE 2006 CRISIS AT CAMPI FLEGREI (SACCOROTTI, <i>ET AL.</i> , 2007).....	35
FIGURE 28 SEISMIC NETWORK IN THE CAMPI FLEGREI AREA. HIGHLIGHTED IN RED ARE THE STATIONS WHOSE WAVEFORMS ARE USED IN THIS WORK (OV-INGV).....	36
FIGURE 29 THREE COMPONENTS OF THE EVENT RECORDED ON OCTOBER 26 TH 2006 AT 00:05 AT THE ASB2 SEISMIC STATION.....	37
FIGURE 30 THREE COMPONENTS OF THE EVENT RECORDED ON OCTOBER 26 TH 2006 AT 00:05 AT THE TAGG SEISMIC STATION.....	37
FIGURE 31 THREE COMPONENTS OF THE EVENT RECORDED ON OCTOBER 26 TH 2006 AT 00:05 AT THE AMS2 SEISMIC STATION.	38
FIGURE 32 THREE COMPONENTS OF THE EVENT RECORDED ON OCTOBER 26 TH 2006 AT 00:05 AT THE BGNB SEISMIC STATION.....	38
FIGURE 33 THE FUNCTION RMST (DOTTED LINE) CALCULATED FOR THE VT WAVEFORM IN THE LOWER PANEL (PETROSINO, <i>ET AL.</i> , 2007).	40
FIGURE 34 SUPERPOSITION OF A SIGNAL (BLACK LINE) AND ITS HILBERT TRANSFORM (BLUE LINE).	41
FIGURE 35 (A) WAVEFORM (FILTERED BETWEEN 0.2 Hz AND 1.2 Hz) OF AN EVENT OF 26 TH OCTOBER 2006 AT THE ASB2 SEISMIC STATION; (B) ITS FUNCTION RMST. THE RED ARROWS CORRESPOND TO THE ARRIVAL TIME AND THE END OF THE SEISMIC IMPULSE.....	42
FIGURE 36 (A) WAVEFORM (FILTERED BETWEEN 0.2 Hz AND 1.2 Hz) OF AN EVENT OF 26 TH OCTOBER 2006 AT THE ASB2 SEISMIC STATION, (B) ITS ENVELOPE, (C) THE ENVELOPE DENOISED. THE RED ARROWS CORRESPOND TO THE ARRIVAL TIME AND THE END OF THE SEISMIC IMPULSE.....	43
FIGURE 37 COMPARISON BETWEEN THE DURATION OBTAINED THROUGH THE TWO DIFFERENT DURATION-ROUTINES (USING THE AMPLITUDE-ENVELOPE (RED DOTS) AND THE RMS (BLUE DOTS) OF THE WAVEFORM) APPLIED TO THE ASB2 WAVEFORMS. EACH INTEGER NUMBER (EVENT INDEX) ON THE X-AXES REFERS TO A DIFFERENT EVENT.....	45
FIGURE 38 SEISMIC WAVE ARRIVAL AT THE SURFACE (KASAHARA, 1981).....	47
FIGURE 39 ENERGY VS DURATION FOR EACH COMPONENT OF EVERY SEISMIC EVENT (SEMI-LOGARITHMIC SCALE) OF THE ASB2 SEISMIC STATION, OBTAINED USING THEORETICAL FORMULA.	48
FIGURE 40 WAVEFORM OF AN EVENT FILTERED BETWEEN 0.2 Hz AND 1.2 Hz (A), ENVELOPE (B) AND ENVELOPE CORRECTED FOR THE BACKGROUND NOISE CONTRIBUTION (C).....	50
FIGURE 41 'ENERGY' FOR EACH WAVEFORM VERSUS DURATION OF THE EVENT VISUALLY SELECTED FROM THE RELATIVE WAVEFORM. THE BLUE SYMBOLS ARE RELATIVES TO THE MAIN IMPULSE IN THE WAVEFORM, THE RED ONE TO THE FIRST SUB-IMPULSE AND THE GREEN TO THE SECOND ONE.	51

FIGURE 42 'ENERGY' FOR EACH WAVEFORM VERSUS DURATION OF THE EVENT SELECTED FROM THE ENVELOPE. THE BLUE SYMBOLS ARE RELATIVES TO THE FIRST IMPULSE IN THE WAVEFORM, THE RED ONE TO THE SECOND AND THE GREEN TO THE THIRD ONE.....	51
FIGURE 43 'ENERGY' OF THE AVERAGE OF THE HORIZONTAL COMPONENTS VERSUS TIME DURATION SELECTED FROM THE WAVEFORMS FOR THE ASB2 SEISMIC STATION. THE BLUE ONES ARE RELATIVES TO THE FIRST IMPULSE IN THE WAVEFORM, THE RED ONE TO THE SECOND AND THE GREEN TO THE THIRD ONE.	52
FIGURE 44 'ENERGY' VERSUS DURATION OF THE AVERAGE OF THE HORIZONTAL COMPONENTS ENVELOPES (CALCULATED VISUALLY SELECTING THE DURATION FROM ENVELOPES) VERSUS TIME DURATION SELECTED FROM THE ENVELOPES FOR THE ASB2 SEISMIC STATION. THE BLUE ONES ARE RELATIVES TO THE FIRST IMPULSE IN THE WAVEFORM, THE RED ONE TO THE SECOND AND THE GREEN TO THE THIRD ONE.....	53
FIGURE 45 WAVEFORM AND RELATIVE SPECTROGRAM FOR THE EVENT OF 26 TH OF OCTOBER 2006, AT 00:05, RECORDED AT THE STATION ASB2 (SAMPLE EVENT). THE FIRST WAVEFORM IS THE E-W COMPONENT, THE SECOND THE N-S COMPONENT AND THE THIRD THE Z ONE.	55
FIGURE 46 WAVEFORM AND RELATIVE SPECTROGRAM FOR THE EVENT OF 26 TH OF OCTOBER 2006, AT 00:05, RECORDED AT THE STATION TAGG. THE FIRST WAVEFORM IS THE E-W COMPONENT, THE SECOND THE N-S COMPONENT AND THE THIRD THE Z ONE.	56
FIGURE 47 WAVEFORM AND RELATIVE SPECTROGRAM FOR THE EVENT OF 26 TH OF OCTOBER 2006, AT 00:05, RECORDED AT THE STATION AMS2. THE FIRST WAVEFORM IS THE E-W COMPONENT, THE SECOND THE N-S COMPONENT AND THE THIRD THE Z ONE.	56
FIGURE 48 WAVEFORM AND RELATIVE SPECTROGRAM FOR THE EVENT OF 26 TH OF OCTOBER 2006, AT 00:05, RECORDED AT THE STATION BGNB. THE FIRST WAVEFORM IS THE E-W COMPONENT, THE SECOND THE N-S COMPONENT AND THE THIRD THE Z ONE.	57
FIGURE 49 WAVEFORM AND RELATIVE SPECTROGRAM FOR THE EVENT OF 26 OF OCTOBER AT 9:12 AT ASB2. THE FIRST WAVEFORM IS THE E-W COMPONENT, THE SECOND THE N-S COMPONENT AND THE THIRD THE Z ONE.	58
FIGURE 50 WAVEFORM AND RELATIVE SPECTROGRAM FOR THE EVENT OF 26 OF OCTOBER AT 9:12 AT TAGG. THE FIRST WAVEFORM IS THE E-W COMPONENT, THE SECOND THE N-S COMPONENT AND THE THIRD THE Z ONE.....	58
FIGURE 51 THREE COMPONENTS WAVEFORM OF THE SAMPLE EVENT. THE 'SUB-IMPULSE' (RED CIRCLE) AFTER THE MAIN EVENT (GREEN CIRCLE) ARE VISIBLE IN THE N-S AND E-W WAVEFORMS.....	60
FIGURE 52 WAVEFORM OF THE SAMPLE FUNCTION AND THE CROSS-CORRELATION CURVE BETWEEN THE 'MAIN-IMPULSE' AND THE 'SECOND-IMPULSE' WITH A TIME WINDOW OF 0.3 S (IN RED RECTANGLES THE PORTION OF WAVEFORMS CROSS-CORRELATED).	61
FIGURE 53 WAVEFORM OF THE SAMPLE FUNCTION AND THE CROSS-CORRELATION CURVE BETWEEN THE 'MAIN-IMPULSE' AND THE 'SECOND-IMPULSE' WITH A TIME WINDOW OF 1 S (IN RED RECTANGLES THE PORTION OF WAVEFORMS CROSS-CORRELATED).	62
FIGURE 54 WAVEFORM OF THE EVENT OF OCTOBER 26 TH 2006 AT 00:05 RECORDED AT ASB2 SEISMIC STATION.	63
FIGURE 55 AVERAGE OF 10 S OF SEISMIC NOISE (ABSOLUTE VALUE) FOR THE THREE COMPONENTS BEFORE EVERY EVENTS RECORDED AT THE ASB2 SEISMIC STATION. EACH INTEGER NUMBER (EVENT INDEX) IN THE X-AXES REPRESENTS AN EVENT. IN BLUE IS THE COMPONENT E-W, IN PINK THE N-S AND IN YELLOW THE Z COMPONENT.	64
FIGURE 56 SAMPLE EVENT OF THE OCTOBER 26 TH 2006 ATE ASB2 SEISMIC STATION. THE RED LINES SHOW THE ONSET OF THE SEISMIC IMPULSE AND THE END OF THE THREE DIFFERENT COMPONENTS USING THE '2T' METHOD. THE FINAL TIME DURATION IS THE SMALLEST OF THE THREE.....	69

FIGURE 57 SQUARED VELOCITY DENSITY SPECTRUM INTEGRATED BETWEEN 0 AND $F_{SUP} = 50$ HZ VERSUS MAGNITUDE FOR DIFFERENT DISTANCES: 1000 M (BLUE), 4000 M (RED), 5000 M (BROWN), 7500 M (GREEN), 10000 M (BLUE) (DEL PEZZO <i>ET AL.</i> , 2013).	75
FIGURE 58 PLOT OF THE PARAMETER C_i VERSUS DISTANCES IN METERS (RED DOTS). THE BLUE LINE REPRESENT THE INTERPOLATION WITH THE 4 TH ORDER POLYNOMIAL.	76
FIGURE 59 VALUES OF $LOG_{10}(S_{VT})$ VERSUS MAGNITUDE THEORETICALLY CALCULATED (LINES) AND INTERPOLATED USING EQ. 47 (DOTS FOR A DISTANCE OF 20 000 M, RHOMBS FOR 4000 M AND STARS FOR 1000 M).	77
FIGURE 60 SPECTRUM OF THE SAMPLE EVENT, ON 26 TH OCTOBER 2006 AT 00:05 RECORDED AT THE SEISMIC STATION ASB2. TYPICAL SPECTRUM WITH THE MAIN PEAK AT 0.83 HZ, AND OTHER MINOR PEAKS.	80
FIGURE 61 SPECTRUM OF THE EVENT ON 27 TH OCTOBER 2006 AT 09:04 RECORDED AT THE SEISMIC STATION ASB2. TYPICAL SPECTRUM WITH A MINOR PEAK AT 2.68 HZ.	80
FIGURE 62 SPECTRUM OF THE EVENT ON 27 TH OCTOBER 2006 AT 10:52 RECORDED AT THE SEISMIC STATION AMS2. TYPICAL SPECTRUM WITH A MINOR PEAK AT 13.14 HZ.	81
FIGURE 63 SPECTRUM OF THE EVENT ON 27 TH OCTOBER 2006 AT 22:08 RECORDED AT THE SEISMIC STATION AMS2. TYPICAL SPECTRUM WITH A MINOR PEAK AT 0.27 HZ AND SOME OTHER PEAKS AT MAJOR FREQUENCIES THAN THE LP CHARACTERISTICS.	81
FIGURE 64 SPECTRUM OF THE EVENT ON 26 TH OCTOBER 2006 AT 9:14 RECORDED AT THE SEISMIC STATION ASB2. A PEAK AT 10.6 HZ IS ALSO IN SPECTROGRAM FOR THE SAME SIGNAL REPORTED IN FIGURE 49.	82
FIGURE 65 DOMINANT FREQUENCY FOR THE ENTIRE SET OF LP SEISMIC DATA ANALYSED IN THIS WORK. EACH INTEGER NUMBER IN THE X AXES (EVENT INDEX) REPRESENTS A DIFFERENT EVENT. THE DIFFERENT COLOURS INDICATE THE LP EVENTS BELONGING TO THE DIFFERENT SEISMIC STATIONS: RED FOR ASB2, BLUE FOR TAGG, GREEN FOR AMS2 AND BLACK FOR BGNB.	83
FIGURE 66 MAGNITUDE VALUES FOR THE ENTIRE SET OF LP SEISMIC DATA OF CAMPI FLEGREI LP, WITH ERROR REPRESENTATION. EACH INTEGER NUMBER IN THE X AXES (EVENT INDEX) REPRESENTS A DIFFERENT EVENT. THE DIFFERENT COLOURS INDICATE THE LP EVENTS BELONGING TO THE DIFFERENT SEISMIC STATIONS: RED FOR ASB2, BLUE FOR TAGG, GREEN FOR AMS2 AND BLACK FOR BGNB.	84
FIGURE 67 MAGNITUDE VALUES OBTAINED FOR THE ENTIRE SET OF LP SEISMIC DATA OF CAMPI FLEGREI. EACH INTEGER NUMBER IN THE X AXES (EVENT INDEX) REPRESENTS A DIFFERENT EVENT. THE DIFFERENT COLOURS INDICATE THE LP EVENTS BELONGING TO THE DIFFERENT SEISMIC STATIONS: RED FOR ASB2, BLUE FOR TAGG, GREEN FOR AMS2 AND BLACK FOR BGNB. THE ERROR ON THE MAGNITUDE IS 0.2.	85
FIGURE 68 MAGNITUDE VALUES OBTAINED FOR THE LP DATA-SET RECORDED AT CAMPI FLEGREI AT ASB2 SEISMIC STATION. EACH INTEGER NUMBER IN THE X AXES (EVENT INDEX) REPRESENTS A DIFFERENT EVENT.	85
FIGURE 69 MAGNITUDE VALUES OBTAINED FOR THE LP DATA-SET RECORDED AT CAMPI FLEGREI AT TAGG SEISMIC STATION. EACH INTEGER NUMBER IN THE X AXES (EVENT INDEX) REPRESENTS A DIFFERENT EVENT.	86
FIGURE 70 MAGNITUDE VALUES OBTAINED FOR THE LP DATA-SET RECORDED AT CAMPI FLEGREI AT AMS2 SEISMIC STATION. EACH INTEGER NUMBER IN THE X AXES (EVENT INDEX) REPRESENTS A DIFFERENT EVENT.	86
FIGURE 71 MAGNITUDE VALUES OBTAINED FOR THE LP DATA-SET RECORDED AT CAMPI FLEGREI AT BGNB SEISMIC STATION. EACH INTEGER NUMBER IN THE X AXES (EVENT INDEX) REPRESENTS A DIFFERENT EVENT.	87
FIGURE 72 MAGNITUDE VERSUS DOMINANT FREQUENCY FOR THE LP SEISMIC EVENTS AT CAMPI FLEGREI RECORDED AT OCTOBER 2006. RED DOTS ARE FOR THE EVENTS RECORDED AT ASB2 SEISMIC	

STATION, BLUE DOTS FOR TAGG STATION, GREEN SYMBOLS FOR AMS2 AND BLACK ONES FOR BGNB SEISMIC STATION. THE ERROR ON THE MAGNITUDE VALUES IS 0.2.....	88
FIGURE 73 MAGNITUDE VERSUS DOMINANT FREQUENCIES FOR THE EVENT RECORDED AT THE ASB2 SEISMIC STATION. THE ERROR ON THE MAGNITUDE VALUES IS 0.2.....	89
FIGURE 74 MAGNITUDE VERSUS DOMINANT FREQUENCIES FOR THE EVENT RECORDED AT THE TAGG SEISMIC STATION. THE ERROR ON THE MAGNITUDE VALUES IS 0.2.....	89
FIGURE 75 MAGNITUDE VERSUS DOMINANT FREQUENCIES FOR THE EVENT RECORDED AT THE AMS2 SEISMIC STATION. THE ERROR ON THE MAGNITUDE VALUES IS 0.2.....	90
FIGURE 76 MAGNITUDE VERSUS DOMINANT FREQUENCIES FOR THE EVENT RECORDED AT THE BGNB SEISMIC STATION. THE ERROR ON THE MAGNITUDE VALUES IS 0.2.....	90
FIGURE 77 MAP OF COLIMA VOLCANO. TRIANGLES REPRESENT THE SEISMIC STATIONS (MAP FROM GOOGLE.IT).	91
FIGURE 78 3C WAVEFORMS OF COLIMA LP RECORDED ON 2005 DECEMBER 3 RD AT COCA SEISMIC STATION.....	92
FIGURE 79 3C WAVEFORMS OF COLIMA LO RECORDED ON 2005 DECEMBER 3 RD AT COBA SEISMIC STATION.....	92
FIGURE 80 DOMINANT FREQUENCIES OF THE COLIMA LP EVENTS RECORDED AT COCA SEISMIC STATION. EACH INTEGER NUMBER IN THE X AXES (EVENT INDEX) REPRESENTS A DIFFERENT EVENT.	93
FIGURE 81 DOMINANT FREQUENCIES OF THE COLIMA LP EVENTS RECORDED AT COBA SEISMIC STATION. EACH INTEGER NUMBER IN THE X AXES (EVENT INDEX) REPRESENTS A DIFFERENT EVENT.	93
FIGURE 82 MAGNITUDE VALUES OBTAINED FOR THE LP EVENTS RECORDED AT COLIMA VOLCANO BY COCA SEISMIC STATION. EACH INTEGER NUMBER IN THE X AXES (EVENT INDEX) REPRESENTS A DIFFERENT EVENT.....	94
FIGURE 83 MAGNITUDE VALUES OBTAINED FOR THE LP EVENTS RECORDED AT COLIMA VOLCANO BY COBA SEISMIC STATION. EACH INTEGER NUMBER IN THE X AXES (EVENT INDEX) REPRESENTS A DIFFERENT EVENT.....	94
FIGURE 84 MAGNITUDE VERSUS DOMINANT FREQUENCY FOR THE EVENTS LP RECORDED AT COLIMA BY COCA SEISMIC STATION.	95
FIGURE 85 MAGNITUDE VERSUS DOMINANT FREQUENCY FOR THE EVENTS LP RECORDED AT COLIMA BY COBA SEISMIC STATION.	95
FIGURE 86 MAP OF MT ETNA SUPERIMPOSED BY THE LOCALIZATIONS OF THE SEISMIC STATIONS (TRIANGLES) AND THE LP EVENT (STAR). THE DEPTH OF THIS SELECTED EVENT IS 2700 M A.S.L. (DEL PEZZO, <i>ET AL.</i> , 2013).	96
FIGURE 87 3C WAVEFORMS OF THE LP RECORDED AT ETNA VOLCANO ON 2005 AUGUST SUPERIMPOSED WITH THE DURATION SELECTION (RED LINES).	97
FIGURE 88 SPECTRUM OF THE LP RECORDED AT ETNA VOLCANO ON 2005 AUGUST AND ITS DOMINANT FREQUENCY.	97

11. List of tables

TABLE 1 PERCENTAGE (ALWAYS CALCULATED OVER THE ENTIRE NUMBER OF 'SUB-IMPULSE' FOR EACH SEISMIC STATION) OF THE MAXIMUM OF THE CROSS-CORRELATION FUNCTIONS THAT PASSED THE THRESHOLD OF 0.8. (THE CROSS-CORRELATION FUNCTION IS NORMALIZED)	62
TABLE 2 VALUES OF THE P PARAMETERS OF THE INTERPOLATION OF THE COEFFICIENT $C(R)$ WITH A 4 TH DEGREE POLYNOMIAL.....	76
TABLE 3 HYPOCENTRAL DISTANCES OF THE STUDIED LP EVENTS AT CAMPI FLEGREI TO THE FOUR SEISMIC STATIONS.	83
TABLE 4 MAGNITUDE VALUES AND HYPOCENTRAL DISTANCES FOR THE EVENT RECORDED ON 2006 OCTOBER 26 TH AT 18:23 AT THE FOUR DIFFERENT SEISMIC STATIONS.....	87

12. Bibliography

- Aki, K., Fehler, M., & Das, S. (1977). Source Mechanism of Volcanic Tremor: Fluid-driven Crack Models and their Application to the 1963 Kilauea Eruption. *Journal of Volcanology and Geothermal Research*, 259 - 287.
- Aster, R., Zandomenichi, D., Mah, S., McNamara, S., Henderson, D., Knox, H., et al. (2008). Moment tensor inversion of very long period seismic signals from Strombolian eruption of Erebus volcano. *Journal of Volcanological and Geothermal Research*.
- Auger, E., D'Auria, L., Martini, M., Chouet, B., & Dawson, P. (2006). Realtime monitoring and massive inversion of source parameters of very long period seismic signals: an application to Stromboli volcano, Italy. *Geophysical Research Letters*.
- Bak, P., Christensen, K., Danon, L., & Scalon, T. (2002). Unified Scaling Law for Earthquakes. *Physical Review Letters*.
- Barberi, F., Bertagnini, A., & Landi, P. (1992). A review on phreatic eruption and their precursors. *Journal of Volcanology and Geothermal Research*, 231 - 246.
- Battaglia, M., Troise, C., Obrizzo, F., Pingue, F., & De Natale, G. (2006). Evidence for fluid migration as the source of deformation at Campi Flegrei caldera (Italy). *Geophysical Research Letters*.
- Battaglia, M., Troise, C., Obrizzo, F., Pingue, F., & De Natale, G. (2006). Evidence of fluid migration as the source of deformation at Campi Flegrei caldera (Italy). *Geophysical Research Letters*.
- Beresnev, I. (2009). The reality of the scaling law of earthquake-source spectra? *Journal of Seismology*.
- Beroza, G., Ide, S., Shelly, D., & Ukide, T. (2007). A scaling law for slow earthquakes. *Nature*.
- Bianchi, R., Coradini, A., Federico, C., Giberti, G., Lanciano, P., Pozzi, J., et al. (1987). Modeling of Surface Deformation in Volcanic Areas: The 1970-1972 and 1982-1984 Crises of Campi Flegrei, Italy. *Journal of Geophysical research*.
- Bianco, F., Castellano, M., Cogliano, R., Cusano, P., Del Pezzo, E., Di Vito, M. A., et al. (2010). *Caratterizzazione del noise sismico nell'area vulcanica dei Campi Flegrei (Napoli): l'esperimento "UNREST"*. Quaderni di geofisica - n° 86.
- Bianco, F., Del Pezzo, E., & Ventura, G. (2004). The role of hydrothermal fluids in triggering the July–August 2000 seismic swarm at Campi Flegrei, Italy: evidence from seismological and mesostructural data. *Journal of Volcanology and Geothermal Research*.

- Boatwright, J. (1980). A spectral theory of circular seismic sources: simple estimates of source dimension, dynamic stress drop and radiated energy. *Bulletin of the Seismological Society of America* .
- Brune, J. (1970). Tectonic stress and spectra of seismic shear waves from earthquakes. *Journal of Geophysical Research*.
- Chouet , B. (1996). Long-period volcano seismicity: its source and use in eruption forecasting. *Nature*, 309-316.
- Chouet, B. (2003). Volcano seismology. *Pure and Applied Geophysics*, 739 - 788.
- Cusano, P., Petrosino, S., & Saccorotti, G. (2008). Hydrothermal origin for sustained Long-Period (LP) activity at Campi Flegrei Volcanic Complex, Italy . *Journal of Volcanology and Geothermal Research*.
- Davis, J. (2002). *Statistics and data analysis in Geology*. Wiley.
- Del Pezzo, E., Bianco, F., & Borgna, I. (2013). Magnitude scale for LP events: a quantification scheme for volcanic quakes. *Geophysical Journal International*.
- Del Pezzo, E., Bianco, F., Castellano, M., Cusano, P., Galluzzo, D., La Rocca, M., et al. (2013). Detection of Seismic Signals from Background Noise in the Area of Campi Flegrei: Limits of the Present Seismic Monitoring. *Seismological Research Letters*.
- Del Pezzo, E., De Natale, G., Martini, M., & Zollo, A. (1987). Source parameters of microearthquakes at Phlegraean Fields (southern Italy) volcanic area. *Physics of the Earth and Planetary Interiors*.
- Del Pezzo, E., Simini, M., & Ibañez, J. (1996). Separation of intrinsic and scattering Q for volcanic areas: a comparison between Etna and Campi Flegrei. *Journal of Volcanology and Geothermal Research*.
- Di Vito, M., Isaia, R., Orsi, G., Southon, J., De Vita, S., D'Antonio, M., et al. (1999). Volcanism and deformation since 12,000 years at the Campi Flegrei caldera (Italy). *Journal of Volcanology and Geothermal Research*.
- Elmore, W., & Heald, M. (1969). *Physics of waves*. Dover Publications.
- Ferrazzini, V., & Aki, K. (1992). Preliminary Results from a Field Experiment on Volcanic Events at Kilauea Using an Array of Digital Seismographs. *Eds Gasparini, P., Scarpa, R. & Aki, K., IAVCEI Proc. in Volcanology, 3, Springer-Verlag*.
- Frasca, S. (2011). Analisi dei segnali. Dipartimento di Fisica - Univeristà di Roma "La Sapienza".
- Gasparini, P., Scarpa, R., & Aki, K. (1992). Preliminary Results from a Field Experiment on Volcanic Events at Kilauea Using an Array of Digital Seismographs. *Volcanic Seismology*, 168-189.
- Hanks, T., & Kanamori, H. (1979). A Moment Magnitude Scale. *Journal of Geophysical Research*.

- INGV. (n.d.). Retrieved from www.ingv.it.
- Johnson, J., & Aster, R. (2005). Relative partitioning of acoustic and seismic energy during Strombolian eruption. *Journal of Volcanology and Geothermal Research*.
- Kanamori, H. (1977). The energy release in great earthquakes. *Journal of Geophysical Research*.
- Kasahara. (1981). *Earthquake mechanics*. Cambridge University Press.
- Kostrov, V. (1974). Seismic moment and energy of earthquakes, and seismic flow of rock. *USSR Academy of Sciences, Physics Solid Earth*.
- Kumagai, H., & Chouet, B. (1999). The complex frequencies of the long-period seismic events as probes of fluid composition beneath volcanoes. *Geophysical Journal International*.
- Kumagai, H., Chouet, B., & Nakano, M. (2002). Waveform inversion of oscillatory signatures in long-period events beneath volcanoes. *Journal Of Geophysical Research*.
- Kumazawa, M., Imanishi, Y., Fukao, Y., & Furumoto, M. (1990). A theory of spectral analysis based on the characteristic property of a linear dynamic system. *Geophysical Journal International*.
- Lay, T., & Wallace, T. (1995). *Modern global seismology*. Academic Press.
- Liberali, V. (2010, Novembre 08). Teoria dei segnali - Densità spettrale di energia e di potenza - campionamento e teorema di Shannon. Milano: Dipartimento di Fisica - Università degli studi di Milano.
- Lirer, L., Luongo, G., & Scandone, R. (1987). On the volcanological evolution of Campi Flegrei.
- Lockmer, I., Bean, C., Saccorotti, G., & Patané, D. (2007). Moment-tensor inversion of lp events recorded on Etna on 2004 using constraints obtained from wave simulation tests. *Geophysical Research Letters*.
- Lucas, G., McKeighan, P., & Ransom, J. (2001). *Nontraditional methods of Sensing Stress, Strain and Damage in Materials and Structures*. ASTM.
- Marzorati, S. (2004). PHD Thesis - dottorato di ricerca in scienze geologiche e geotecnologie per l'ambiente e il territorio - xix ciclo. *Fenomenologia del noise sismico ambientale: dalla conoscenza del segnale alle applicazioni empiriche*.
- Matoza, R., & Chouet, B. (2010). Subevents of long-period seismicity: Implications for hydrothermal dynamics during the 2004–2008 eruption of Mount St. Helens. *Journal of Geophysical Research*, B12206.
- McNutt, S. (2005). Volcanic Seismology. *Annu. Rev. Earth Planet. Sci.*
- Miller, A., Stewart, R., White, R., Lockett, R., Baptie, B., Aspinall, W., et al. (1998). Seismicity associated with dome growth and collapse at the Soufriere Hills Volcano, Montserrat. *Geophysical Research Letters*, 3401 - 3404.

- Morhange, C., Marriner, N., Laborel, J., Todesco, M., & Oberlin, C. (2006). Rapid sea-level movements and noneruptive crustal deformations in the Phlegrean Fields caldera, Italy. *Geological Society of America*.
- Morse, P., & Bolt, R. (1944). Sound waves in room. *Modern Physics*.
- Nakano, M., & Kumagai, H. (2005). Response of a hydrothermal system to magmatic heat inferred from temporal variations in the complex frequencies of long-period events at Kusatsu-Shirane Volcano, Japan. *Journal of Volcanology and Geothermal Research*.
- Nakano, M., Kumagai, H., Chouet, B., & Dawson, P. (2007). Waveform inversion of volcano-seismic signals for an extended source. *Journal of Geophysical Research*.
- OV-INGV. (n.d.). Retrieved from www.ov.ingv.it.
- OV-INGV. (2012). *Bollettino mensile vulcani campani*.
- OV-INGV. (2013). *Bollettino mensile vulcani campani*.
- Patanè, D., Aliotta, M., Cannat, A., Cassisi, C., Coltelli, M., Di Grazia, G., et al. (2011). Interplay between Tectonics and Mount Etna's Volcanism: Insights into the Geometry of the Plumbing System. *New Frontiers in Tectonic Research - At the Midst of Plate Convergence, Dr. Uri Schattner (Ed.)*.
- Petrazzuoli, S., Troise, C., Pingue, F., & De Natale, G. (1999). The mechanics of Campi Flegrei unrest as related to plastic behaviour of the caldera borders. *Annali di Geofisica*.
- Petrosino, S., Cusano, P., La Rocca, M., Galluzzo, D., Orozco-Rojas, J., Bretón, M., et al. (2011). Source location of long period seismicity at Volcàn de Colima, Mexico. *Bulletin of Volcanology*.
- Petrosino, S., De Siena, L., & Del Pezzo, E. (2008). Recalibration of the Magnitude Scales at Campi Flegrei, Italy, on the Basis of Measured Path and Site and Transfer Functions. *Bulletin of Seismological Society of America, 1964–1974*.
- Piccinini, D., & Saccorotti, G. (2008). First revelation of non-volcanic, long period seismicity in the central Appenines, Italy. *Geophysical Research Letters*.
- Rosi, M., Sbrana, A., & Principe, C. (1983). The Phlegrean Fields; Structural evolution, Volcanic history and eruptive mechanisms. *Journal of Volcanology and Geothermal Research*.
- Rosi, M., & Sbrana, A. (1987). Phlegrean Fields. *CNR Quaderni della ricerca scientifica*.
- Saccorotti, G., Bianco, F., & Castellano, M. (2001). The July-August 2000 seismic swarms at Campi Flegrei volcanic complex, Italy. *Geophysical research letters, 2525-2528*.

- Saccorotti, G., Petrosino, S., Bianco, F., Castellano, M., Galluzzo, D., La Rocca, M., et al. (2007). Seismicity associated with the 2004–2006 renewed. *Physics of the Earth and Planetary Interiors*, 14-24.
- Scandone R., B. F. (1991). The structure of the Campanian Plain and the activity of Neapolitan volcanoes. *Journal of Volcanology and Geothermal Research*.
- Scandone, R., & Giacomelli, L. (1998). *Vulcanologia - principi fisici e metodi d'indagine*. Liguori.
- Shearer, P. (1999). *Introduction to Seismology*. Cambridge.
- Troise, C., De Natale, G., Pingue, F., Obrizzo, F., De Martino, P., Tammaro, U., et al. (2007). Renewed ground uplift at Campi Flegrei caldera (Italy): New insight on magmatic processes and forecast. *Geophysical Research Letters*.
- Varley, N., Arámbula-Mendoza, R., Reyes-Dávila, G., Stevenson, J., & Harwoo, R. (2010). *Long-period seismicity during magma movement at Volcán de Colima*. Bulletin of Volcanology.
- Vulcani d'Italia - Uniroma3*. (n.d.). Retrieved from <http://vulcan.fis.uniroma3.it/italia/campania/campi/right-left.html>.
- Wassermann, J. (2011). *Volcano seismology*.
- Zobin, V. (2003). *Introduction to volcanic seismology*. ELSEVIER.
- Zollo, A., Herreo, A., & Emolo, A. (2003). *Terremoti ed onde: introduzione alla sismologia sperimentale*.

ACKNOWLEDGMENTS

I would like to express my special appreciation and thanks to my tutor Dr.ssa Francesca Bianco, for encouraging my study and my research and for the great support, guidance, patience and advice during the entire research project.

I also thank Prof. Edoardo Del Pezzo for his great support and help during this work, and all the others INGV-OV researchers for their help.

I would like to thank Prof. Roberto Scandone for his helpful advice.

I would especially like to thank all the colleagues of the Geophysics Laboratory of the Physics Department at RomaTre University, thanks to all of you!

Finally I would like to express my gratitude to my family for supporting me and a special thanks to Federico for believing in me more than I do.

Eva thank you for all!!!